

AD A090343

LEVEL

12/8/80
C

DTIC
ELECTE
OCT 9 1980
S D C

TIME DEPENDENT NAVIER-STOKES SOLUTION OF A
TURBULENT GAS JET EJECTED FROM A RECTANGULAR
ORIFICE INTO A HIGH-SUBSONIC CROSSFLOW

DISSERTATION

AFIT/DS/AA/80-1 William C. Golbitz
Major USAF

Approved for public release; distribution unlimited

80 9 30 018

(6) TIME DEPENDENT NAVIER-STOKES SOLUTION
OF A TURBULENT GAS JET EJECTED FROM A RECTANGULAR
ORIFICE INTO A HIGH-SUBSONIC CROSSFLOW

DISSERTATION

Presented to the Faculty of the School of Engineering
of the Air Force Institute of Technology

Air University

in Partial Fulfillment of the
Requirements for the Degree of
Doctor of Philosophy

(1) [REDACTED]

by

(10) William C. Golbitz, E.S., M.S.

Major

USAF

(11) June 1980

(12) [REDACTED]

Approved for public release; distribution unlimited

512-15

TIME DEPENDENT NAVIER-STOKES SOLUTION OF A
TURBULENT GAS JET EJECTED FROM A RECTANGULAR
ORIFICE INTO A HIGH SUBSONIC CROSSFLOW

by

William C. Golbitz, B.S., M.S.

Major

USAF

Accession For	
NTIS GRA&I	<input checked="" type="checkbox"/>
DTIC TAB	<input type="checkbox"/>
Unannounced	<input type="checkbox"/>
Justification	
By	
Distribution/	
Availability Codes	
Dist	Avail. and/or Special
A	

Approved:

Harold E. Wright
Chairman

2 July 1980

John Jones Jr.

2 July 1980

Prof. J. Shing

10 July 1980

Will Hakey

10 July 1980

James E. Hitchcock

11 July 1980

Stephen J. Kool

11 July 1980

Accepted:

J. S. Przemieniecki
Dean, School of Engineering

15 July 1980

Acknowledgements

I am deeply indebted to Dr. Harold Wright for his enthusiastic support, encouragement, and guidance throughout the research phase when progress in increments of "two steps forward and one step backward" seemed to typify the research process. I am also grateful to Dr. James VanKuren who together with Dr. Wright provided the necessary contacts to obtain a research topic which would be of wide utility while at the same time would be solvable within finite time constraints.

I am especially thankful to Dr. Joseph Shang for unselfishly sharing his considerable expertise in computational fluid dynamics and for providing an "arena" in which concepts and ideas were freely tested and exchanged leading to understanding of the complex physical nature of the flow interaction. I also thank Major Stephen Koob for his thought provoking questions which invariably led to further understanding.

I thank Dr. James Hitchcock for providing me with the "tools of the trade" without which much of the insight and knowledge required would have been lacking. I also thank Dr. John Jones for providing his strong mathematical background and for making some disastrous days more bearable.

I thank all the members of the Computational Aerodynamics Group at the Flight Dynamics Laboratory of the Air Force Wright Aeronautical Laboratories, Wright-Patterson AFB, Ohio, and especially Dr. Wilbur Hankey for providing the stimulating environment in which to conduct the requisite research. I further thank the Advanced Radiation Technology Office at the Air Force Weapons Laboratory, Kirtland AFB, New Mexico, for providing the computational support on their CDC 7600.

Finally, I thank my best friend, my wife Marcy, for enduring the last three years and providing constant support and understanding even though just being wife, mother, and surrogate father would surely have been far more than I could have wished, and, at times, far more than I deserved.

William Golbitz

Contents

Acknowledgements	iii
List of Figures	vii
List of Tables	x
Notation	xi
Abstract	xv
I. Introduction	1
I.1 Jets in Crossflows - Background	4
Experiment and Empirical Methods	4
Potential Flow Methods	12
Integral Methods	15
Numerical Methods	15
I.2 Summary	17
II. Mathematical Model of the Physical Problem.	19
II.1 Model Governing Equations	20
II.2 Thermodynamic Properties	22
II.3 Turbulence Model	24
II.4 Boundary Conditions	25
II.4.1 Upper Face	26
II.4.2 Windward Face	27
II.4.3 Remaining Faces	28
II.5 Summary	28
III. Numerical Solution Algorithm	30
III.1 Computational Grid	30
III.2 Spatial Derivatives: Non-uniform Mesh	31
III.3 Optimum Cross-Derivative Approximations	34
III.4 Finite Difference Equations	37
III.4.1 Conservation of Mass	38
III.4.2 Conservation of Momentum	40
III.4.3 Conservation of Energy	45
III.4.4 Conservation of Species	48
III.4.5 Boundary Conditions	49
III.5 Stability Requirements	52
III.6 Convergence Criteria	55
III.7 Summary	57
IV. Results of the Numerical Simulation	59
IV.1 Verification of the Numerical Algorithm	59
IV.1.1 Numerical Solution: Convergence	60
IV.1.2 Numerical Solution: Results	62

IV.2	Airborne Chemical Laser Exhaust	68
IV.2.1	Numerical Solution: Convergence	69
IV.2.2	Numerical Solution: Results	71
	Trajectory Analysis	71
	Flowfield Analysis	75
IV.3	Simplified Analyses	78
IV.3.1	Helium Jet	78
IV.3.2	Hot Air Jet	80
IV.4	Molecular Weight Correction	81
IV.5	Turbulence Diffusivity: Heat Transfer Effects	83
IV.6	Summary	86
V.	Conclusions and Recommendations	89
	Bibliography	94
	Appendix A: 1962 United States Standard Atmosphere	147
	Appendix B: Gaussian Jet Velocity Profile	154
	Appendix C: Gas Transport Properties	156
	Appendix D: Thermodynamic Properties	167
	Vita	170

List of Figures

<u>Figure</u>	<u>Page</u>
1 Jet Flowfield Schematic	101
2 Jet Element Model: Abromovich Model	102
3 Computational Domain Aircraft Jet Injection Model	103
4 Finite Subdivision of Computational Domain	104
5 Staggered Mesh: Cell Variable Location	105
6 Computational Domain Weston and Thames Experimental Model	106
7 Convergence Criterion Weston Simulation: $K=1.1$, Coarse Mesh	107
8 Convergence Criterion Weston Simulation: $K=1.05$, Coarse Mesh	108
9 Convergence Criterion Weston Simulation: $K=1.05$, Refined Mesh	109
10a Y-Plane Flowfield: Symmetry Plane -2	110
10b Y-Plane Flowfield: Symmetry Plane -1	111
10c Y-Plane Flowfield: Symmetry Plane	112
10d Y-plane Flowfield: Symmetry Plane +1	113
10e Y-Plane Flowfield: Symmetry Plane +2	114
11 Experimental and Analytical Results Symmetry Plane	115
12 Symmetry Plane Flowfield: Coarse Mesh	116
13a Pressure Coefficient Contour Map Right Half-Plane	117
13b Weston-Thames Pressure Coefficient Contour Map: Right Half-Plane, $R=4.01$	118
13c Pressure Coefficient Correlation $R=4.0$, $X/D_e=0.0$	119

<u>Figure</u>		<u>Page</u>
14a	Peake Experiment Pressure Coefficient Contour Map, $R=4.0$	120
14b	Peake Experiment Pressure Coefficient Contour Map, $R=4.1$	121
15	Surface Pressure Distribution	122
16	Convergence Criterion AFWL Gas, $K=1.2$, Coarse Mesh	123
17	Convergence Criterion AFWL Gas, $K=1.09$, Fine Mesh	124
18	Trajectory Analysis: Density Contour Map, AFWL Gas	125
19	Trajectory Analysis: Temperature Contour Map, AFWL Gas	126
20	Trajectory Analysis: Mass Fraction Contour Map, AFWL Gas	127
21	Trajectory Analysis: Molecular Weight Contour Map, AFWL Gas	128
22	Jet Trajectory Comparisons	129
23	Flowfield Analysis: Mach Number Contour Map, AFWL Gas	130
24a	Flowfield Analysis: Symmetry Plane, AFWL Gas	131
24b	Flowfield Analysis: Symmetry Plane -1, AFWL Gas	132
24c	Flowfield Analysis: Symmetry Plane -2, AFWL Gas	133
25	Symmetry Plane Surface Properties	134
26	Flowfield Analysis: Symmetry Plane Pressure Coefficient Map	135
27	Convergence Criterion: Helium, $K=1.20$, Coarse Mesh	136
28	Flowfield Analysis: Helium, $K=1.20$, Coarse Mesh	137

<u>Figure</u>		<u>Page</u>
29	Trajectory Analysis: Helium, $K=1.20$, Coarse Mesh	138
30	Convergence Criterion: Hot Air, $K=1.20$, Coarse Mesh	139
31	Flowfield Analysis: Hot Air, $K=1.20$, Coarse Mesh	140
32	Trajectory Analysis: Hot Air, $K=1.20$, Coarse Mesh	141
33	Adiabatic Wall Temperature: Hot Air, $K=1.20$, Coarse Mesh, Molecular	142
34	Adiabatic Wall Temperature: Hot Air, $K=1.20$, Coarse Mesh, Turbulent	143
35	Adiabatic Wall Temperature: Helium, $K=1.20$, Coarse Mesh, Molecular	144
36	Adiabatic Wall Temperature: Helium, $K=1.20$, Coarse Mesh, Turbulent	145

List of Tables

<u>Table</u>		<u>Page</u>
I	AFWL Gas Mixture (Case 2C)	146
C.1	Lennard-Jones (12-6) Force Constants	166
D.1	Thermochemical Data, c_p	168
D.2	Thermochemical Data, $h-h_{298.15}$	169

Notation

<u>Symbol</u>	<u>Meaning</u>
a	Local speed of sound, Eq (32); Semi-major axis of jet orifice, Appendix B.
b	Semi-minor axis of jet orifice, Appendix B.
c_p, c_v	Specific heats at constant pressure and volume.
D	Binary diffusion coefficient of gas mixture; Effective binary diffusion coefficient.
D	Dimension of jet orifice aligned with the freestream.
D_e	Equivalent diameter of rectangular orifice, (diameter of circle with same area)
D_h	Hydraulic diameter, Eq (10).
d	Circular jet diameter.
E	Specific energy of the gas mixture, Eq (19).
f_i	Body forces in each spatial coordinate direction.
G	Molecular weight correction factor, Eq (100).
$G_{\text{diff-k}}$	Diffusive flux of species-k due to concentration gradients, Eq (21).
h, h_k	Specific enthalpy of gas mixture and species-k.
i, j, k	Indices corresponding to spatial coordinate directions.
I	Specific internal energy of the gas mixture, Eq (19).
k	Turbulent kinetic energy; Boltzmann constant, Appendix C; Thermal conductivity of gas mixture, Eq (20).
K	Geometric stretch factor for vertical mesh, Eq (41); Correction factor of truncated bivariate Gaussian distribution, Appendix B.
L	Length of computational domain, Eq (99).
m_k	Mass fraction of species-k, $m_k = \rho_k / \rho$.
M, M_k	Molecular weight of gas mixture and species-k; Mach number, $M = U/a$.

<u>Symbol</u>	<u>Meaning</u>
P	Pressure of gas mixture.
p	Property of the gas mixture.
Pr_t	Turbulent Prandtl Number, $Pr_t=0.9$
Q	Jet to freestream dynamic pressure ratio.
R_{gas}	Universal gas constant.
R	Gas constant of gas mixture, $R=R_{gas}/\text{Molecular weight}$; Jet to freestream velocity ratio.
s	Exponent in molecular weight correction, Eq (100).
3_k	Source (chemical) for species-k, Eq (84).
Sc_t	Turbulent Schmidt Number, $Sc_t=0.9$
T	Temperature of gas mixture.
t	Temporal variable.
U	Magnitude of velocity.
U_i	Mean velocity component in each spatial coordinate direction.
u,v,w	Velocity components of each cell in x, y, and z directions.
V_e	Equivalent velocity ratio, Eq (9).
V_j	Jet exit velocity.
x,y,z	Spatial coordinates associated with Cartesian mesh.

<u>Greek</u>	<u>Meaning</u>
α	Donor cell parameter, $0 < \alpha < 1$.
γ	Ratio of specific heats, Eq (29).
δ	Jet injection angle, Eq (9); Boundary layer thickness, Eq (37); Non-dimensional pressure, Appendix A.
Δ	Incremental temporal or spatial variable.
δ_{ij}	Kronecker delta tensor, $\delta_{ij}=1$ iff $i=j$, else $\delta_{ij}=0$.
ϵ	Eddy viscosity, Eq (33); Turbulent energy dissipation; Convergence criterion, Eq (98); Well depth of Lennard-Jones (12-6) Potential.
Θ	Non-dimensional temperature, Appendix A.
λ	Second coefficient of molecular viscosity, Eq (15); Thermal conductivity, Appendix C.
μ	First coefficient of molecular viscosity, Eq (15); Viscosity, Appendix C; Mean value, Appendix B.
ξ	Grid increment for non-uniform mesh Taylor series expansions, Eqs (43)-(48).
ρ, ρ_k	Density of gas mixture and species-k.
σ	Lennard-Jones (12-6) collision diameter, Appendix C; Non-dimensional density, Appendix A.
σ_x, σ_y	Standard deviation in the x and y values respectively, Appendix B.
τ_{ij}	Shear stress tensor, Eq (15).
ϕ	Parameter in non-uniform mesh Taylor series expansions, Eqs (43)-(48).
ω	Over-relaxation factor.
Ω	Collision integrals required in transport properties, Appendix C.

<u>Subscripts</u>	<u>Meaning</u>
char	characteristic
eff	effective
j	jet
max	maximum value
min	minimum value
mix	mixture
t	turbulent
∞	freestream
$(),_t$	$\partial() / \partial t$, derivative with respect to time
$(),_j$	$\partial() / \partial x_j$, derivative with respect to j-coordinate variable

<u>Superscripts</u>	<u>Meaning</u>
.	per unit time
$\bar{}$	average
+	non-uniform mesh expansion, to right of central value
-	non-uniform mesh expansion, to left of central value
*	property at the tropopause, Appendix A.

<u>Miscellaneous</u>	<u>Meaning</u>
$ \cdot $	Absolute value
	Evaluated at

Abstract

↘
The high temperature ($1500 \text{ n}^{\text{deg}}\text{K}$) exhaust gases from an airborne chemical laser being forcibly ejected downwards at a jet to freestream dynamic pressure ratio (Q) of 0.15 from an aspect ratio 1.75 rectangular diffuser orifice aligned with the major axis parallel to the Mach 0.7 ambient crossflow at the tropopause was successfully simulated using a modified donor-cell ICE (Implicit Continuous fluid Eulerian) algorithm formulated in primitive variables. The complete set of time dependent, three-dimensional Navier-Stokes equations and a species conservation equation were numerically solved for every cell in the computational domain. The diffusive flux effects caused by concentration gradients (Fick's Law) as well as variable transport and thermodynamic properties of the gas mixture were incorporated into the numerical model. Turbulence closure was achieved by employing a locally varying velocity defect eddy viscosity model. Chemical reactions between the exhaust gases and the ambient crossflow were proscribed. ↙

↘
Data acquired from the numerical simulations were used to define the trajectory of the jet plume, the extent of the recirculation zone in the wake, and the regions with possibly large heat transfer rates. ↘
Simplified analyses were also conducted to determine whether essential flow phenomena were captured mathematically using simple binary gas interactions. Convective processes were observed to dominate the low Q jet-crossflow interaction for gas mixture, helium, and air injectants; each of the simulations contained essentially the same flow features and characteristics. Thermal diffusion was also seen to have a significantly greater effect than molecular diffusion for the jet-

crossflow gases simulated. For the low molecular weight injectants, a secondary wall vortex (recirculation zone) was created approximately 3.2 jet streamwise dimensions (D) aft of the jet center apparently caused by diffusive transport due to concentration gradients in the presence of a constraining "no-slip" wall. The lateral span of the wall vortex did not exceed 0.3 D.

Jet penetration of the ambient flowfield was observed to be dependent upon the molecular weight of the injectant for the constant Q constraint. A molecular weight correction factor used in typical heat-mass transfer boundary layer problems was utilized to synthesize the trajectory curve of one gas from that of another gas at the same conditions and to correct empirically derived trajectory formulae for variances in molecular weight. The latter technique resulted in less than 5 percent variation from the corresponding trajectory derived from the numerical simulation. Sensitivity analyses relating the heat transfer to the injection surface from the jet plume with the magnitude of the turbulent diffusivities were also conducted.

TIME DEPENDENT NAVIER-STOKES SOLUTION
OF A TURBULENT GAS JET EJECTED FROM A RECTANGULAR
ORIFICE INTO A HIGH-SUBSONIC CROSS FLOW

I. Introduction

The development of the Airborne Laser Laboratory II (ALL II) involves the emplacement of a large chemical laser on board a wide body jet aircraft. This study in support of the ALL II program is concerned with the three-dimensional flowfield produced by the interaction of the high temperature, low molecular weight waste gas (generated by the chemical laser system and forcibly exhausted normally downward from a rectangular diffuser embedded in the aft fuselage) with the surrounding high-subsonic ambient freestream. Because of both the high temperature and the corrosive nature of the chemical laser exhaust, it is imperative to determine the extent of the heating on the aircraft fuselage and the plume of the laser effluent. Consequently, the primary goals of this research effort are (1) to demonstrate the feasibility of the numerical methodology to accurately predict the viscous jet-crossflow interaction, (2) to solve the three-dimensional jet trajectory problem for the real gas exhaust mixture, and, (3) to determine the location and extent of regions with possibly large rates of heat transfer to the injection surface. Ancillary goals of determining the location and extent of any recirculation zone, the structure and characteristics of the jet-crossflow interaction, and the effects of the diffusivity induced by the turbulence on the heat transfer from the hot gas mixture to the aircraft surface are also of prime importance.

It is widely recognized that there exist at least three principal

regions of interest for problems in which a turbulent jet is injected into a crossflow independent of the respective gases as indicated in Figure 1. The first of these is designated as the "near field" or "potential core" region and is characterized by the irrotationality and dominance of the jet flow. As the crossflow impacts the issuing jet, a compression zone is formed ahead of the jet while a pressure defect zone is formed behind the jet. It is this induced pressure difference which initiates the deformation of the jet (Ref 1) and which consequently provides the basis for the interactive mixing of the two flows. The second, or intermediate, region has been termed "curvilinear" by Chan and Kennedy (Ref 2) and "zone of maximum deflection" by Pratte and Baines (Ref 3). It is characterized by the rapid change in direction of the jet from its initial injection to that of the governing crossflow. Within this zone, a pair of counterrotating vortices are formed which enhance the entrainment of fluid from the crossflow into the jet plume and which directly affect the jet-crossflow interaction. The final region is designated as "far field" in which the jet flow is essentially aligned with the crossflow and in which it is assumed that profiles of velocity and fluid properties exhibit Gaussian similitude; additionally, the flow is further assumed to be isotropic.

Real gases at elevated temperatures being forcibly ejected into a cross flowing stream of another gas complicate any mathematical modeling of the flow interaction. Adequate description of the gas dynamics is proscribed by approximate integral, potential, or boundary layer methodologies; consequently, only the full set of time dependent Navier-Stokes equations utilizing both variable gas transport and thermodynamic

properties become requisite. Prior to this study and the advancement in technology it represents, no documented numerical method existed which could provide time dependent solutions to problems of this type in three-dimensions. The development and validation of this numerical scheme as a useful engineering predictive tool within each of the regions associated with the jet-crossflow interaction comprise the bulk of the research effort.

Historically, the early studies of jets injected into crossflows were concerned with obtaining empirical formulae to define the jet trajectory. There exist many means of mathematically defining the trajectory curve, including those of the following list:

- (1) Locus of maximum velocity,
- (2) Locus of maximum total pressure,
- (3) Locus of maximum total temperature,
- (4) Locus of maximum species concentration,
- (5) Locus of maximum / minimum density,
- (6) Locus of maximum pressure coefficient.

Most researchers have normally chosen to define the mean flow trajectory by curve fitting the loci of maximum velocity or momentum flux. Additionally, the empirical methodology is further split into two groups: (1) analytical, and (2) experimental.

The major impetus affecting jet-crossflow research was the advent of modern V/STOL aircraft and the attendant need to define the aerodynamic impact of the interaction of the jet-crossflow upon the air vehicle performance, stability and control. Not only were trajectory data of prime importance, but also data describing the pressure and

velocity fields near the jet orifice and their associated effects on the vehicle surface became equally vital. Paralleling the advance in aircraft technology, large commercial power stations came into vogue and the need to define the impact of exhaust particulate dispersion on the local environment also became a matter of research interest as well as civic concern. These two driving forces helped focus research effort on approximate integral and potential flow methodologies. Finally, the Navier-Stokes solutions of the jet-crossflow problem became more tractable with the development of modern computational machinery. Each of the aforementioned methodologies will be briefly examined in the next section.

I.1 Jets in Crossflows - Background

Experiment and Empirical Methods. The early analytical studies detailing the behavior of jet injection into a crossflow were accomplished for round jets because of the reduction in complexity afforded by the geometry. The simplest analyses were concerned with deriving mathematical expressions for the jet trajectory. Abromovich used the method developed by M. S. Volinskii (Ref 1) in which each infinitesimal segment of the jet is treated as an airfoil at some given sweep angle with respect to the crossflow (see Figure 2.). Enforcing the condition of radial equilibrium, the normal component of the sectional aerodynamic drag was equated to the centrifugal force from which the local radius of curvature of the jet trajectory was computed. Abromovich's following expression (12.162) for the trajectory of a jet normally injected from a flat plate into a crossflow results:

$$\frac{y}{d} = 14.4 \sqrt{a} \log_{10} \left[1 + 0.1 \frac{x}{d} \left(1 + \sqrt{1 + 20 \frac{d}{x}} \right) \right] \quad (1)$$

$$\text{where } a = \frac{\rho_j v_j^2}{\hat{C}_d \rho_\infty U_\infty^2} ;$$

d is the initial diameter of the jet at injection;

x, y are the streamwise and normal coordinate directions, respectively;

and \hat{C}_d is the jet element drag coefficient.

Vizel and Mostinskii (Ref 2) improved the agreement of this semi-empirical method by determining the trajectory of the jet utilizing the drag coefficient of the entire jet, C_d . If experimental results were available, the following expression

$$\log_{10} \left| 1 + 0.049 \frac{x}{d} \right| = 0.0153 C_d \left(\frac{\rho_j v_j^2}{\rho_\infty U_\infty^2} \right) \left(\frac{y}{d} \right)^2 \quad (2)$$

could be used to determine C_d ; if on the other hand, C_d were either known or arbitrarily assigned,

$$\frac{y}{d} = 16.2 \left[\log_{10} \left(1 + 0.049 \frac{x}{d} \right) \left(\frac{\rho_j v_j^2}{\rho_\infty U_\infty^2 C_d} \right) \right]^{0.5} \quad (3)$$

could be used to determine the trajectory of the jet. Further refinements to this methodology were added by Epshtein (Ref 5) and Vakhlamov (Ref 6). Epshtein removed the restriction of the normal component of the jet momentum being constant and permitted it to vary with the gravitational force. Vakhlamov developed prescribed control

surfaces over which a momentum balance was conducted. His resulting expression for the trajectory of a round jet injected normally into a crossflow is given by

$$\bar{x} = \bar{y} + (2.530 \bar{y} + 1.590 \bar{y}^2 + 0.143 \bar{y}^3) \frac{\rho_{\infty} U_{\infty}^2}{\rho_j V_j^2} \quad (4)$$

where $\bar{x} = x/d$ and $\bar{y} = y/d$.

Shandarov (Ref 7) following the basic methodology used by Abromovich, obtained a similar expression for circular jets ejected normally into a uniform unbounded subsonic gas flow,

$$\frac{y}{d} = \frac{1}{C_d} \frac{q_2}{q_1} \ln \left[\left\{ \left(1 + C_d \frac{q_1}{q_2} \frac{x}{d} \right)^2 - 1 \right\}^{0.5} + \left(1 + C_d \frac{q_1}{q_2} \frac{x}{d} \right) \right] \quad (5)$$

where $q_1 = \rho U_{\infty}^2$ and $q_2 = \rho_j V_j^2$ at injection.

Despite the degree of analysis each of the derivations for the preceding expressions entailed, the range of jet-crossflow parameters is rather limited to be of practical engineering value. Consequently, empirical power law expressions for the trajectory have been developed for a wider range of temperature, density, and velocity ratios. Abromovich presented two empirical expressions developed by Shandarov

and Ivanov ostensibly for air jets. They are given by the following expressions for normal jet-crossflow injection:

$$\text{Shandarov : } \frac{x}{d} = \frac{\rho_{\infty} U_{\infty}^2}{\rho_j v_j^2} \left(\frac{y}{d} \right)^{2.55} \quad (6)$$

$$\text{for } 2 \leq \frac{\rho_j v_j^2}{\rho_{\infty} U^2} \leq 22$$

$$\text{and } 1 \leq \frac{T_{\infty}}{T_j} \leq 3$$

$$\text{Ivanov : } \frac{x}{d} = \left(\frac{\rho_{\infty} U^2}{\rho_j v_j^2} \right)^{1.3} \left(\frac{y}{d} \right)^3 \quad (7)$$

$$\text{for } 12 \leq \frac{\rho_j v_j^2}{\rho_{\infty} U^2} \leq 1000$$

Callaghan and Ruggeri (Ref 8) experimentally determined an empirical expression valid for heated (860 °R) circular air jets with jet Reynolds numbers based upon the diameter between 60,000 and 500,000. Their expression rewritten in terms of the same notation as the above equations is given by

$$\frac{x}{d} = 0.118 \left(\frac{\rho_{\infty} U_{\infty}^2}{\rho_j v_j^2} \right)^2 \left(\frac{y}{d} \right)^{3.3} \quad (8)$$

Their use of the jet to freestream mass flux ratio as opposed to the

dynamic pressure (or equivalently, the momentum flux) ratio provides better agreement than many other formulae. Margason (Ref 9) experimentally determined another relationship describing the trajectory of the circular air jet in terms of the jet injection angle and effective velocity ratio. His comparisons with both experimental data and empirical trajectory equations of other investigators provide invaluable insight into the jet plume deflection phenomenon. Written in terms of the same variables as the preceding equations, Margason's relationship is expressed by,

$$\frac{x}{d} = \frac{V_e^2}{4 \sin^2 \delta_j} \left(\frac{y}{d} \right)^3 + \left(\frac{y}{d} \right) \cot \delta_j \quad (9)$$

where V_e is the effective velocity ratio,

$$V_e = \sqrt{\frac{\rho_\infty U_\infty^2}{\rho_j V_j^2}} ;$$

and δ_j is the jet injection angle.

Not only were his comparisons of existing formulae to experiment of prime importance, but also his determination through experiment that the trajectory equations could be applied to jets injected either normally upwards or downwards (for the range of V_e considered) increased the utility of the existing empirical data base. Nowhere else are data recorded for downwardly injected jets; additionally, his research is unique in that data were presented for injection angles of 30 through 180 degrees (opposing flow) and for numerous values of effective velocity ratio.

Although the preceding trajectory equations were initially developed for round jets injected into crossflows, the same expressions are valid as first approximations for orifice shapes other than circular if the diameter of the jet, d , is replaced by the hydraulic diameter which is defined as follows:

$$D_h = 4 \left(\frac{\text{cross sectional area}}{\text{wetted perimeter}} \right) \quad (10)$$

Ivanov, as referenced in the text by Abromovich, confirmed this fact for rectangular jets with an aspect ratio (length/width) of 5.0 both in the streamwise and blunt orientations; however, no reference was made to the flow conditions upon which this conclusion was based. It should be noted that a similar substitution occurs in convective heat transfer problems involving tubes of non-circular cross section (Ref 10).

The effects of orifice shape on jet flow coefficients for normally discharging jets into a cross flowing air stream were investigated by Callaghan and Bowden (Ref 11). This work was expanded by Ruggeri, Callaghan, and Bowden (Ref 12) to determine the penetration of air jets directed perpendicularly to the free stream air from non-circular jets and to correlate the results with those for circular jets through the use of the jet flow coefficient. Ruggeri (Ref 13) later furthered the efforts of his co-workers by similarly correlating temperature profiles of heated air jets downstream of the injection point.

As discussed to this point, each of the investigative efforts has provided the means to describe the trajectory of the jet-crossflow interaction, but, none have provided any information regarding the

observed gas dynamic phenomena to include the creation and transport of the counterrotating vortex pair and the entrainment of both crossflow mass and momentum. Jordinson (Ref 14) was among the first researchers to provide detailed data about the structure of both the flowfield and the jet plume. He provided total pressure coefficient contours and jet centerline trajectories for jet to crossflow velocity ratios of 4, 6, and 8. Additionally, he presented a flowfield vector plot for a jet-crossflow velocity ratio of 6. In his data, the characteristic kidney shape cross sections in planes normal to the trajectory were clearly observed. The results also show the entrainment of low velocity air from the vicinity of the injection plane into the jet. Gelb and Martin (Ref 15) recorded pressure distributions and conducted a detailed photographic study of high speed jets (125 to 1000 feet per second) being injected into low speed (15 to 60 feet per second) crossflows.

Keffer and Baines (Ref 16) formulated an entrainment coefficient which was proportional to the difference between the jet and crossflow velocities and which considered only the effect of the entrained momentum upon the trajectory of an initially round turbulent non-buoyant jet. Slawson and Csanady (Ref 17) observed power station chimney stacks and the effluent discharged from them. From careful observations and known values of exhaust temperature, velocity, and mass flow in addition to known ambient parameters, they formulated a modified turbulent entrainment hypothesis which enabled them to predict the mean path of the turbulent, buoyant exhaust plumes. Pratte and Baines (Ref 18) used a methodology similar to Margason including the use of photographs of a round turbulent jet injected with an aerosol (oil as opposed to water)

to obtain not only trajectory data, but also data relating to the jet spread and eddy structure of the plume. Chan and Kennedy compared numerous empirical expressions (Ref 2, Table 2-1) to compute the mean trajectory of the jet-crossflow interaction for both entrainment and drag formulations, some of which have been discussed within this section. They observed, as did Margason, that nearly all the empirical equations defining the jet trajectory can be written in the following general form,

$$\frac{x}{d} = K \left(\frac{y}{d} \right)^m \left(\frac{\rho_{\infty} U_{\infty}^2}{\rho_j U_j^2} \right)^n \quad (11)$$

where K is some prescribed constant, and,

$$m \sim 3 \text{ and } 1 \leq n \leq 1.5 .$$

For completeness, Lee (Ref 19) and Garner (Ref 20) authored survey reports detailing the state-of-the-art of jet-crossflow interaction studies.

Experimentalists of the next decade carried on from where those of the 1960's stopped. Kamotani and Greber (Ref 21) not only extended the pioneering work of Keffer and Baines for unheated circular air jets, but they also extended the available data base for circular heated air jets. The dependency of the trajectory on the jet to crossflow momentum flux (or, dynamic pressure) ratio, Q, was confirmed. Additionally, they also confirmed that entrainment of the crossflow was independently controlled by the normal and parallel components of the velocity impacting the plume, an assumption used by Chan and Kennedy as well as other investigators.

Experimental and analytical "far field" studies of viscous three-dimensional turbulent air jets exhausting from rectangular and other shaped orifices into quiescent environments were conducted by Sforza, Steiger, and Trentacoste (Ref 22), Trentacoste and Sforza (Ref 23), and Sforza Ref (24). Detailed "near field" velocity and shear stress measurements were made for turbulent, incompressible air jets ejected from square orifices into quiescent environments by duPlessis, Wang, and Kahawita (Ref 25). Their results showed square jet characteristics which differed only slightly from those of corresponding circular jets. Only recently, have the properties of non-circular jets being ejected normally into subsonic crossflows been of interest. Weston and Thames (Ref 26) conducted experimental investigations of rectangular, isothermal air jets normally injected into subsonic cross flowing air from an orifice with an aspect ratio of 4. Both the streamwise and blunt orientations of the jet were examined for both planar and streamlined body (nacelle) injection surfaces. Empirical trajectory power law expressions somewhat similar to those obtained for round jets were obtained after extensive numerical analyses to ensure the best fit for the range of jet to crossflow velocity ratios tested (4, 8, and 10). Additionally, empirical power law expressions similar to those for the trajectory were presented to define the vortex locus curve, i.e., the trajectory the induced vortices follow.

Potential Flow Methods. Many potential flow methods have been devised to ascertain the aerodynamic effects of normal circular jet injection upon V/STOL aircraft. The earliest potential method was developed by Chang Hsin-Chen (Ref 27) to mathematically describe the

vortex "roll-up" effect observed when a cylinder is placed in a uniform crossflow. Since jet injection from V/STOL aircraft occurs at relatively high ratios of jet to crossflow velocities, the jet appears as a quasi-solid body and consequently, the methodology which Chang derived has been used as the basis for more complex potential flow algorithms. Bradbury and Wood (Ref 28) not only experimentally measured the pressure field on the injection surface from which a circular jet issued for jet to crossflow velocity ratios of 2, 4, 8, and 11.3, but, they also noted that the jet could be qualitatively simulated by a blockage and distributed line sink representation. Gelb and Martin (Ref 15), attempted to describe the jet flow interaction for both low and high jet to crossflow velocity ratios by the superposition of a uniform stream and a line sink distribution on the jet axis with only limited success. In the same vein, albeit a more successful one, Wooler (Ref 29) developed his own expression for the jet plume centerline based upon the experimental results of Jordinson from which the local radius of curvature along the jet axis could be determined. After balancing the centrifugal force exerted on the jet by the crossflow, the jet plume was subdivided into a large but finite number of elements. A distribution of trailing vortices was then developed from which the induced flow field and pressure distribution on the injection surface could be computed. Williams and Wood (Ref 30) developed a more refined "vortex sheet" method based upon the earlier work of Wooler. It also required an empirical expression for the jet trajectory, but, it provided better agreement with experimental data. Wooler, Burghart, and Gallagher (Ref 31) developed a theoretical model which did not require the use of an

empirical expression for the jet center line, but which required the jet to be represented by a distribution of both sinks and doublets to account for the entrainment and blockage of the jet. Again, the objective of the investigators was to determine the induced aerodynamic effects upon the surface from which the jet was issuing and not to determine quantitative data concerning the physics of the flowfield interaction. Wu, Mosher, and Wright (Ref 32) conducted both analytical and experimental investigations for circular and elliptical normally injected jets in streamwise and blunt configurations. Their potential method utilized doublets, vortices, and sinks to model the effects of entrainment and blockage; additionally, the wake region of the jet was excluded. However, this model, as well as other potential flow models, required the use of an empirical formula for the jet trajectory to describe the three-dimensionality of the flow interaction which simply is not available in potential representations. The empirical model utilized in their method was that of Wooler which is presented here for completeness,

$$\frac{x}{d} = B \left(\cosh \frac{y}{Bd} - 1 \right) \quad (12)$$

$$\text{where } B = 0.19 \left(\frac{V_j}{U_\infty} \right)^2 .$$

Additional investigations have followed similar approaches. Among them are the works of Braun and McAllister (Ref 33) and Rubbert (Ref 34). Endo and Nakamura (Ref 35) developed a mathematical model of the round

jet-crossflow interaction by consolidating the efforts of previous investigators, including the vortex model of Wooler, and then correlated predictions from it with experimental data.

Integral Methods. The work of Chan and Kennedy included approximate integral analyses of the turbulent round jet for all three zones of the jet-crossflow interaction as well as experimentally derived data. Comparisons of their analytical predictions with experimental data, both their own as well as others, consistently show reasonable agreement. Their bibliography of jet-crossflow research efforts is by far one of the most complete and current. Schatzmann (Ref 36) extended the efforts of Chan and Kennedy for turbulent round jets in both the "curvilinear" and the "far field" regions and corrected the mathematical errors entailed in the analyses from which Chan and Kennedy derived their methodology. Additionally, Schatzmann recast the governing equations in terms of the natural coordinates of the jet in vector form.

Numerical Methods. Numerical computation of the three-dimensional behavior of jets has become possible with the current generation of high speed computers. Computations of co-flowing turbulent supersonic circular, elliptic, and interacting square jets were accomplished by Oh and Harris (Ref 37) utilizing an ADI (Alternating Direction Implicit) scheme to solve the steady flow parabolic-elliptic Navier-Stokes equations in three dimensions. The parabolized equations were formed from the Navier-Stokes equations utilizing the assumption of a preferred main flow direction which dominates the convective processes. Consequently, derivatives with respect to this direction are assumed negligible in the shear stress terms. However, as noted by Oh and

Harris, "...the system is formally correct for supersonic flows; for subsonic flows, the static pressure distribution or its gradient in the marching direction must be specified if the problem is to be well posed mathematically". Little additional complexity was added to their methodology by the incorporation of a simple algebraically prescribed mixing length eddy viscosity model through which turbulence closure was achieved. McGuirk and Rodi (Ref 38) computed the steady, three-dimensional behavior of turbulent, rectangular, incompressible, free jets with aspect ratios of 1, 5, 10, and 20 issuing into a quiescent atmosphere. They utilized the finite difference scheme of Pantankar and Spalding for three-dimensional parabolic flows and achieved closure through use of a two-equation turbulent kinetic energy-dissipation ($k-\epsilon$) model. Chien and Schetz (Ref 39) computed the normally injected turbulent round jet-crossflow interaction for an incompressible fluid using the vorticity-velocity formulation of the steady Navier-Stokes equations. Closure was obtained through use of a Prandtl constant eddy viscosity model. Pantankar, Basu, and Alpay (Ref 40) applied a finite difference code to solve the turbulent round jet injection-crossflow problem for an incompressible fluid. Closure was achieved through essentially the same two-equation turbulent kinetic energy-dissipation model McGuirk and Rodi used. The steady, incompressible formulations of the last two groups of investigators numerically predicted the flowfield caused by the interaction of the jet and crossflow for relatively slow crossflows and high jet to crossflow velocity ratios with reasonable accuracy.

I.2 Summary

Numerous empirical formulae have been developed to describe the trajectory of a jet injected at some arbitrary angle into a crossflow comprised of the same or a different fluid. Most of these expressions are generalizable to a power law form as expressed by Eq (11); however, these expressions were developed for flows characterized by neither low ratios of jet to freestream momentum flux, nor, for low ratios of jet to freestream mean molecular weights. Potential flow approximations to the jet-crossflow interaction problem have marginal utility for flowfield analysis although they may be used to adequately describe the aerodynamic effects of the jet upon V/STOL aircraft performance, stability, and control. Numerical methods currently being used to solve the three-dimensional jet injection problem are restricted to jets injected into relatively slow crossflows or quiescent atmospheres. Furthermore, the Navier-Stokes equations were simplified by assuming no time dependence and constant fluid density. In some cases, the set of equations was parabolized to enable existing solution algorithms to be used. To date, no other computational methodology has been documented which will permit computation of the the complex flow structure caused by the interaction of real, viscous fluids being injected into crossflows characterized by either low or high jet to crossflow velocity ratios. Furthermore, no known method developed to date has been used to even attempt the same feat with real, low molecular weight gas mixtures at elevated temperatures injected into a high-subsonic ambient crossflow with atmospheric properties corresponding to the altitude at which the injection occurs. The balance of this document details the development

and validation of the methodology as a useful predictive engineering tool to advance both the state-of-the-art and the general knowledge of jet-crossflow interactions. Section II describes the governing equations, boundary conditions, and ancillary relations required to mathematically model the physical problem. Section III details both the finite difference formulations of the model and the methodology to implement them as well as the factors inherent in both the model and physical problem which directly affect the stability and convergence of the numerical solutions. Finally, the results of the research and the associated conclusions drawn from them are presented in Sections IV and V respectively.

II. Mathematical Model of the Physical Problem

The complex flow interaction problem created by the exhaust of an airborne chemical laser aboard a wide-bodied aircraft which is discharging into a high-subsonic ambient crossflow presents formidable difficulties in the modeling of the mixing processes. The simplifications made by previous investigators to permit integral analyses to be conducted are not valid for the existing problem and, consequently, the complete set of non-linear, coupled equations (Navier-Stokes) must be utilized to describe the behavior of the viscous-inviscid fluid interaction; the equations are further encumbered by the requirement to compute the fluid properties of the mixture which are constantly changing with the temperature and species concentration. These equations are formulated in Cartesian tensor notation for compactness and clarity within this section.

Additionally, the wide variation in molecular weights further exacerbates the task of approximating properties of the fluid mixture. Using the assumption that the exhausting multi-component gas is homogeneous in composition while neglecting the possibility of chemical reactions with ambient air occurring within the flowfield permits not only the binary mixture diffusion coefficient (Appendix C) to be computed, but, also introduces many simplifications in both the species conservation and global energy conservation equations.

Because the matrix of problem dependent parameters is overwhelming in nature, representative values for the aircraft Mach number (0.7) and pressure altitude (36089.239 feet, or, 11 kilometers) were chosen. Additionally, only one representative jet mixture (Table I) was

utilized. For all real gas test cases, the jet temperature was defined to be 1500 °K and the jet Mach number was defined to be 0.24; the ratio of jet to freestream dynamic pressures was constrained to the value 0.15. The orifice aspect ratio of 1.75 used for the injection studies was based on preliminary design data of the laser exhaust diffuser as implemented on the bottom of the fuselage of a wide-bodied air vehicle.

II.1 Model Governing Equations

The full set of time dependent Navier-Stokes equations describing the mean flow quantities in three dimensions in addition to a species conservation equation were required to solve the jet injection and associated flowfield interaction problem. These equations for the gas mixture, in conservation form, are expressed in Cartesian tensor notation (utilizing the Einstein summation convention) as follows:

Conservation of Mass

$$\rho_{,t} + (\rho U_j)_{,j} = 0 \quad (13)$$

Conservation of Momentum

$$(\rho U_i)_{,t} + (\rho U_i U_j)_{,j} + P_{,i} - \tau_{ij,j} = \rho f_i \quad (14)$$

$$\text{where } \tau_{ij} = \lambda \delta_{ij} U_{j,j} + \mu_{\text{eff}} (U_{i,j} + U_{j,i}) \quad (15)$$

$$\text{and where } \lambda = -\frac{2}{3} \mu_{\text{eff}} \quad (16)$$

$$\text{and } \mu_{\text{eff}} = (\mu + \mu_t) \quad (17)$$

Conservation of Energy

$$(\rho E)_{,t} + (\rho E U_j + P U_j - \tau_{kj} U_k + \dot{q}_j)_{,j} = \rho f_1 U_1 \quad (18)$$

$$\text{where } E = I + (U_1 U_1)/2 \quad (19)$$

$$\text{and where } \dot{q}_j = -k_{\text{eff}} T_{,j} + \sum_k^N G_{\text{diff } k} h_k \quad (20)$$

$$\text{where } G_{\text{diff } k} = -\rho D_{\text{eff}} (\rho_k / \rho)_{,j} \quad (21-a)$$

$$k_{\text{eff}} = k + \mu_t c_p / Pr_t \quad (21-b)$$

$$D_{\text{eff}} = D + (\mu_t / \rho) / Sc_t \quad (21-c)$$

Conservation of Species

$$(\rho_k)_{,t} + (\rho_k U_j + G_{\text{diff } k})_{,j} = 0 \quad (22)$$

Despite the favorable properties and utility of the conservation form of the governing equations, sometimes it is even more desirable, depending upon the solution algorithm, to reformulate them in non-conservative, primitive variable form. This was accomplished on the momentum equations by expanding Eq (14) and then removing the continuity equation (Eq (13)). The resultant expression for the momentum equations is given by,

$$\rho (U_{1,t} + U_j U_{1,j}) + P_{,1} - \tau_{1j,j} = \rho f_1 \quad (23)$$

Similarly, the continuity equation was removed from the energy equation. Specifically, when Eq (23) is dotted with the velocity, U_i , the following expression results:

$$\rho i \left(U_i U_i / 2 \right)_{,t} + U_j \left(U_i U_i / 2 \right)_{,j} + U_i P_{,i} - U_i \tau_{i,j-j} - \rho \dot{U}_i f_i = 0 \quad (24)$$

This expression was then subtracted out of the energy equation to provide the following ancillary version of the energy equation which was actually solved,

$$\rho (I_{,t} + U_j l_{,j}) + P U_{j,j} - \tau_{k,j} U_{k,j} + \dot{q}_{j,j} = 0 \quad (25)$$

Thus, the Navier-Stokes equations, viz. Eqs (13), (23) and (25), and the species conservation equation, Eq (22), comprise the set of governing equations of the model.

11.2 Thermodynamic Properties

The thermodynamic properties of the gas mixture are calculated as functions of temperature from tabular data of each constituent gas (Appendix B). Both the specific heat at constant pressure, c_p , and the enthalpy of the gas mixture, h , are calculated from the following equations:

$$c_p = \sum_j^N (\rho_j / \rho) c_{p,j} = \sum_j^N m_j c_{p,j} \quad (26)$$

$$h = \sum_j^N m_j h_j \quad (27)$$

where the expression (ρ_j/ρ) is the mass fraction of the j^{th} -species, m_j , and where c_{p_j} and h_j are the j^{th} -species specific heat at constant pressure and enthalpy, respectively.

The average molecular weight of the gas mixture, \bar{M} , is defined (Ref 10) by the following expression,

$$\bar{M} = \left\{ \sum_j^N \frac{m_j}{M_j} \right\}^{-1} \quad (28)$$

where M_j is the j^{th} -species molecular weight. The ratio of specific heats at constant pressure to that at constant volume, γ , is then expressible in terms of the gas mixture variables which were presented above, that is,

$$\gamma = c_p / c_v = \left\{ 1 - R_{\text{gas}} / \bar{M} c_p \right\}^{-1} \quad (29)$$

The equation of state for an ideal gas was written in terms of the specific internal energy, I , and the ratio of specific heats (Eq (29)); it is given by the following expression:

$$P = (\gamma - 1) \rho I \quad (30)$$

The temperature of the gas mixture was then calculated locally by the following expression,

$$T = I / c_v = I\gamma / c_p \quad (31)$$

Finally, the local speed of sound of the gas mixture was calculated from the following equation:

$$a_{mix} = \sqrt{\gamma(\gamma - 1) I} \quad (32)$$

II.3 Turbulence Model

To incorporate the effects of turbulence, a simple algebraically prescribed eddy viscosity model was used instead of any higher order model which did not necessarily improve the accuracy of the solution while it most assuredly would increase the computational complexity. Harsha (Ref 41) reviewed numerous locally and history dependent jet turbulence models for widely varying gas combinations in co-flowing jets; however, none were evaluated explicitly for jets discharging normally into crossflows. Chien and Schetz (Ref 39) used a simple constant Prandtl velocity defect eddy viscosity formulation, the value of which was predetermined by the initial jet and crossflow velocities. They further determined that for an incompressible fluid, variations in the proportionality constant in this model affected the jet trajectories minimally and therefore retained the constant associated with coflowing round jets such that the eddy viscosity was expressed by (Ref 39, Eq 16)

$$\epsilon = 0.0256 (U_{jet} - U_{\infty}) (D/2) \quad (33)$$

where D is the injection diameter of the jet. Morkovin (Ref 42) has shown that the turbulence structure of gasdynamic flows is essentially unaffected by compressibility for Mach numbers less than 5. Because of the complexity of the flowfield and the inherent difficulty in modeling

it, the simplest model to reasonably approximate the turbulent transport phenomena should be used. Consequently, Eq (33) was modified to account for variations of jet and freestream velocities as well as mixture density. The resultant expression for the turbulence model used in the flowfield simulation is given by,

$$\mu_t = 0.0256 \rho_1 |\bar{U} - U_\infty| (D/2) \quad (34)$$

$$\text{where } \bar{U} = \sqrt{U_i U_i}, \quad i = 1, 2, 3$$

and ρ_1 is the local mixture density.

Additionally, Eq (34) has the required property of applying the turbulence corrections where the jet is actually mixing with the crossflow. As the flow becomes more uniform, the augmented mixing due to turbulence becomes negligible and the mean flow (laminar) equations correctly define the fluid dynamics.

II.4 Boundary Conditions

The approximation of the physical problem was accomplished by creating a rectangular computational domain (Figure 3). The faces of this domain are defined as follows:

- (1). Upper face
 - a. Injection surface, "no-slip" boundary
 - b. Jet orifice, prescribed inflow boundary
- (2). Windward face, prescribed inflow boundary
- (3). Leeward face, continuative outflow boundary
- (4). Front lateral face, continuative outflow boundary
- (5). Back lateral face, continuative outflow boundary

(6). Lower face, continuative outflow boundary

The rectangular jet was forced to discharge into a uniform crossflow with ambient properties corresponding to the aircraft pressure altitude; the local boundary layer build-up corresponded to that of a wide bodied aircraft at the proposed location for the chemical laser diffuser exit. The capability to prescribe either "top-hat" or Gaussian (Appendix B) profiles of the jet injection velocity was accommodated in the model. The boundary conditions employed in the mathematical model are presented as follows for each face of the computational domain.

II.4.1 Upper Face (6)

The injection surface of the upper face (simulating the lower surface of the aircraft fuselage) was defined to be "no-slip" such that both the normal and tangential components of the velocity were zero, that is,

$$U_i = 0 \quad , \quad i = 1, 2, 3 \quad . \quad (35)$$

It was further assumed that the injection surface behaved as an adiabatic wall. This condition results in derivatives of the fluid specific internal energy, I , at the surface in the normal direction exhibiting no variation assuming that c_v is locally constant for every affected cell. When the boundary layer approximation of the pressure variation in the normal direction is also incorporated within the model, the following general fluid property boundary condition results at the injection surface, namely,

$$\frac{\partial P}{\partial n} = 0 \quad (36)$$

where P is any thermodynamic variable of the fluid,
such as pressure, temperature, internal energy, etc.

The prescribed inflow conditions of the jet orifice were defined by the properties of the exhaust gas mixture (Table I) at an arbitrarily prescribed temperature (1500 °K) and Mach number (0.24). The jet to crossflow dynamic pressure ratio was constrained to be 0.15 which in turn specified the exhaust jet pressure and density since both the freestream and jet Mach numbers were held fixed.

II.4.2 Windward Face (1)

This face of the computational domain was a completely prescribed inflow boundary whose fluid properties and velocities were defined by the aircraft flight parameters of Mach number and altitude. The normal (streamwise) component of velocity was prescribed by,

$$U = \begin{cases} U_{\infty} (y / \delta)^{1/4}, & \text{within the turbulent boundary layer, where the boundary layer thickness is given by,} \\ \delta = 0.376 \times Re_x^{-0.2} & \\ U_{\infty} & , \text{outside the turbulent boundary layer,} \end{cases} \quad (37)$$

whereas the tangential velocity components were both assumed to be negligible, that is,

$$v = w = 0 \quad (38)$$

Again, the normal derivative of the fluid thermodynamic variables was assumed to be zero, and specified mathematically by Eq (36).

II.4.3 Remaining Faces (2,3,4,5)

The remaining faces of the computational domain were all defined as continuative outflow boundaries. Initially, the normal derivatives of both the velocity and the gas mixture properties were enforced to be identically zero, i.e.,

$$\frac{(\partial U_i)}{\partial n} = 0 \quad (39)$$

and

$$\frac{(\partial P)}{\partial n} = 0, \quad (36)$$

where P again is any fluid thermodynamic variable. However, as the solution of the equations progressed, the velocities and properties were allowed to adjust to ensure compliance with both the boundary conditions and the governing equations.

II.5 Summary

The physical problem of an airborne chemical laser venting waste exhaust gases overboard into a high-subsonic (0.7 Mach) ambient crossflow at some prescribed aircraft pressure altitude (11 km) was modeled by creating a rectangular computational domain over which certain necessary boundary conditions were enforced. The upper surface of this domain was considered to represent the "no-slip" aircraft fuselage bottom through which the rectangular exhaust jet was forcibly

ejected downwards at a given temperature (1500 °K), Mach number (0.24), and jet to crossflow dynamic pressure ratio (0.15). The remaining faces were established as continuative outflow boundaries. Only the leeward face, normal to the incoming crossflow, was prescribed by the aircraft Mach number and pressure altitude; the others were permitted to relax from the initial prescription of the "no-change", or "first derivative", boundary condition and to acquire values which ensured that the governing Navier-Stokes equations were satisfied. The next section details the finite difference algorithm and the requisite subdivision of the computational domain employed to solve the mathematical description of the model presented in this section.

III. Numerical Solution Algorithm

The computational domain defined in Section II was divided into a large, but finite, number of three-dimensional rectangular cells as shown in Figure 4. The governing non-linear differential equations were approximated by finite difference algebraic equations which were then solved for every cell within the computational domain. A simple algorithm was developed by Hirt, Nichols, and Romero (Ref 43) for time-dependent, two-dimensional, incompressible flows and was later modified by Cloutman, Nichols, and Romero (Ref 44) to incorporate the effects of compressibility with the assumption of constant fluid transport properties. The latter version also incorporated the Implicit Continuous fluid Eulerian (ICE) method as an option (Ref 45) by which the best estimate of the time advanced pressure was utilized in the momentum equations. The algorithm used a primitive variable, donor-cell formulation which, in fact, formed the basis of the methodology used for the numerical simulation of the jet injection problem. However, the algorithm was further modified in this study to solve fully three-dimensional, mixed species, real gas flows with both variable transport and thermodynamic properties.

III.1 Computational Grid

The spatial increments in the x and y directions respectively, Δx and Δy , were uniform, that is,

$$\begin{cases} \Delta x = \text{constant}, \\ \Delta y = \text{constant}, \end{cases} \quad (40)$$

but, they were not necessarily equal. Because of the violent nature of the jet injection problem and the associated near field mixing, the corresponding spatial increments in the z-direction were varied geometrically from the injection surface in an effort to capture the physics of the problem by locally refining the mesh in the region of maximum fluid interaction. The mathematical description of the geometrically varying cell lengths in the z-direction is given by,

$$\Delta z_k = \Delta z_0 K^{k-1} \quad (41)$$

where the Δz_0 and Δz_k are the initially prescribed and subsequent k-th values respectively of the cell vertical dimensions as measured from the wall, and K is the constant multiplicative factor of the geometric expansion between any two consecutive members.

Together with the spatial incrementation given in Eqs (40) and (41), the solution algorithm used a staggered mesh as indicated in Figure 5. The properties of the gas mixture for every (i,j,k)-cell, for example, $P(i,j,k)$, were defined at the cell center; the velocities, on the other hand, were defined at the centers of the (i,j,k)-cell faces. The velocities on the six faces ($u(i,j,k)$, $u(i-1,j,k)$, $v(i,j,k)$, $v(i,j-1,k)$, $w(i,j,k)$, $w(i,j,k-1)$) are indicated in the figure noting that the velocity components are situated in planes normal to their respective directions.

III.2 Spatial Derivatives : Non-uniform Mesh

Because of the prescribed variation of Δz_k , the normal expressions for the three-point, second order, spatially centered approximations to

the first and second derivatives associated with a constant mesh could not be used. However, Taylor series expansions were utilized to derive the required derivative expressions for non-uniform meshes, the discussion of which follows directly.

If the set of values of a given parameter $\{\phi_k\}$ are distributed on a non-uniform mesh in an arbitrary spatial direction at the nodes $\{\phi_1, \phi_2, \dots, \phi_n, \dots, \phi_k\}$, then the Taylor series expansions for both ϕ_{n+1} and ϕ_{n-1} may be generated in terms of $\Delta\xi^+$ and $\Delta\xi^-$, where

$$\begin{cases} \Delta\xi^+ = \phi_{n+1} - \phi_n, \text{ and} \\ \Delta\xi^- = \phi_n - \phi_{n-1}. \end{cases} \quad (42)$$

The expansions for ϕ_{n+1} and ϕ_{n-1} are then given by,

$$\begin{aligned} \phi_{n+1} = & \phi_n + \phi_n' (\Delta\xi^+) + \frac{\phi_n''}{2!} (\Delta\xi^+)^2 \\ & + \frac{\phi_n'''}{3!} (\Delta\xi^+)^3 + \frac{\phi_n^{iv}}{4!} (\Delta\xi^+)^4 + \dots \end{aligned} \quad (43)$$

and,

$$\begin{aligned} \phi_{n-1} = & \phi_n - \phi_n' (\Delta\xi^-) + \frac{\phi_n''}{2!} (\Delta\xi^-)^2 \\ & - \frac{\phi_n'''}{3!} (\Delta\xi^-)^3 + \frac{\phi_n^{iv}}{4!} (\Delta\xi^-)^4 - \dots \end{aligned} \quad (44)$$

When Eq (43) is multiplied by $(\Delta\xi^-)^2$ and Eq (44) is multiplied by

$(\Delta\xi^+)^2$, and when the resulting expressions are subtracted from one another, the required expression for the first derivative of ϕ is easily obtained and it is given by,

$$\begin{aligned}\phi'_n = & \frac{(\Delta\xi^-)}{(\Delta\xi^+)(\Delta\xi^+ + \Delta\xi^-)} \phi_{n+1} + \frac{(\Delta\xi^+ - \Delta\xi^-)}{(\Delta\xi^+)(\Delta\xi^-)} \phi_n \\ & - \frac{(\Delta\xi^+)}{(\Delta\xi^-)(\Delta\xi^+ + \Delta\xi^-)} \phi_{n-1} + O(\Delta\xi^+, \Delta\xi^-)\end{aligned}\quad (45)$$

Verification of this spatially "centered" expression for a uniform mesh is easily obtained by requiring that $\Delta\xi^+ = \Delta\xi^- = \Delta$. The resulting expression,

$$\phi'_n = \frac{\phi_{n+1} - \phi_{n-1}}{2\Delta} + O(\Delta^2)\quad (46)$$

is immediately discerned as the second order accurate, spatially centered finite difference approximation to the first derivative of ϕ for a uniformly varying computational mesh.

Similarly, the equivalent spatially centered expression for the finite difference approximation for the second derivative of ϕ is obtained. When Eq (43) is multiplied by $(\Delta\xi^-)$ and Eq (44) is multiplied by $(\Delta\xi^+)$, and the resulting expressions are added to one another, the required expression for the second derivative of ϕ is obtained. It is given by,

$$\phi_n'' = \frac{2}{(\Delta\xi^+) (\Delta\xi^+ + \Delta\xi^-)} \phi_{n+1} - \frac{2}{(\Delta\xi^+) (\Delta\xi^-)} \phi_n + \frac{2}{(\Delta\xi^-) (\Delta\xi^+ + \Delta\xi^-)} \phi_{n-1} + O(\Delta\xi^+, \Delta\xi^-) \quad (47)$$

Again, verification of the expression for the non-uniform mesh is obtained by letting the non-uniform increments be equal to some arbitrary constant, that is, $\Delta\xi^+ = \Delta\xi^- = \Delta$. The resulting expression,

$$\phi_n'' = \frac{\phi_{n+1} - 2\phi_n + \phi_{n-1}}{\Delta^2} + O(\Delta^2) \quad (48)$$

is readily discerned to be the spatially centered, second order accurate finite difference approximation for the second derivative of ϕ for a constant mesh increment. Both Eq (45) and Eq (47) show that typically second order accurate finite difference approximations associated with uniform grids degrade drastically to first order approximations when the mesh is appreciably non-uniform. The larger the value of the geometric expansion factor (K) in Eq (41), the more pronounced the numerical error becomes.

III.3 Optimum Cross-Derivative Approximations

In the momentum partial differential equations, Eq (14), the following velocity cross derivative terms appear in the expansion of the stress tensor:

$$\text{x-direction : } \frac{\partial^2 v}{\partial x \partial y}, \frac{\partial^2 w}{\partial x \partial z}$$

$$\text{y-direction : } \frac{\partial^2 u}{\partial y \partial x}, \frac{\partial^2 w}{\partial y \partial z} \quad (49)$$

$$\text{z-direction : } \frac{\partial^2 u}{\partial z \partial x}, \frac{\partial^2 v}{\partial z \partial y}$$

Each of these partial derivatives can be approximated by suitable finite difference expressions. However, proper use of Taylor series expansions for the velocities about the (i,j,k)-cell component velocities results in approximations with negligible truncation error.

As an example, the approximation for $\frac{\partial^2 u}{\partial z \partial x}$ in the z-direction momentum equation is fabricated from several Taylor series expansions about u(i,j,k). Since the marching direction for the expansions is identified by the particular momentum equation (z-direction), the u-component in the z-direction is allowed to vary between the "k" and "k+1" cells; because x is not the marching direction, the u-component is only permitted to vary between the "i" and "i-1" cells; the y-direction cell index, "j", remains fixed. Consequently, the u-component velocities of interest are u(i,j,k), u(i,j,k+1), u(i-1,j,k+1), and u(i-1,j,k). Expansions of these velocities about u(i,j,k) are as follows:

$$\begin{aligned} u(i,j,k+1) = & u \Big|_{i,j,k} + \Delta z \frac{\partial u}{\partial z} \Big|_{i,j,k} \\ & + \frac{\Delta z^2}{2!} \frac{\partial^2 u}{\partial z^2} \Big|_{i,j,k} + O(\Delta z^3) \end{aligned} \quad (50)$$

$$\begin{aligned}
u(i-1, j, k+1) = & u \Big|_{i, j, k} + \Delta z \frac{\partial u}{\partial z} \Big|_{i, j, k} + \frac{\Delta x \Delta z}{2} \frac{\partial^2 u}{\partial x \partial z} \Big|_{i, j, k} \\
& + \frac{1}{2} \left(\Delta x^2 \frac{\partial^2 u}{\partial x^2} \Big|_{i, j, k} - 2 \Delta x \Delta z \frac{\partial^2 u}{\partial z \partial x} \Big|_{i, j, k} + \Delta z^2 \frac{\partial^2 u}{\partial z^2} \Big|_{i, j, k} \right) + O(\Delta x^3, \Delta z^3) \quad (51)
\end{aligned}$$

$$u(i-1, j, k) = u \Big|_{i, j, k} - \Delta x \frac{\partial u}{\partial x} \Big|_{i, j, k} + \frac{\Delta x^2}{2} \frac{\partial^2 u}{\partial x^2} \Big|_{i, j, k} - O(\Delta x^3) \quad (52)$$

When Eqs (50) and (52) are added, and then Eq (51) is subtracted from the resulting expression, the "optimum" finite difference form of the partial derivative is given by

$$\frac{\partial^2 u}{\partial z \partial x} = \frac{u(i, j, k+1) - u(i-1, j, k+1) - u(i, j, k) + u(i-1, j, k)}{\Delta z \Delta x} \quad (53)$$

This form of the finite difference approximation to the example partial derivative possesses the fortuitous property of truncation error cancellation by the components thereby increasing the accuracy of the numerical solution. The remaining finite difference approximations to the partial derivatives indicated in Eq (49) were similarly determined and are summarized as follows:

x-direction :

$$\frac{\partial^2 v}{\partial x \partial y} = \frac{v(i+1, j, k) - v(i+1, j-1, k) - v(i, j, k) + v(i, j-1, k)}{\Delta x \Delta y} \quad (54)$$

$$\frac{\partial^2 w}{\partial x \partial z} = \frac{w(i+1, j, k) - w(i+1, j, k-1) - w(i, j, k) + w(i, j, k-1)}{\Delta x \Delta z} \quad (55)$$

y-direction :

$$\frac{\partial^2 u}{\partial y \partial x} = \frac{u(i,j+1,k) - u(i-1,j+1,k) - u(i,j,k) + u(i-1,j,k)}{\Delta y \Delta x} \quad (56)$$

$$\frac{\partial^2 w}{\partial y \partial z} = \frac{w(i,j+1,k) - w(i,j+1,k-1) - w(i,j,k) + w(i,j,k-1)}{\Delta y \Delta z} \quad (57)$$

z-direction :

$$\frac{\partial^2 v}{\partial z \partial y} = \frac{v(i,j,k+1) - v(i,j-1,k+1) - v(i,j,k) - v(i,j-1,k)}{\Delta z \Delta y} \quad (58)$$

III.4 Finite Difference Equations

In accordance with the SOLA-ICE algorithm (Ref 44), the governing partial differential equations were approximated by finite difference equations using a modified donor cell formulation. The advected terms were modeled by a sum of spatially centered and donor cell terms, while the remaining terms were approximated by difference expressions and techniques readily available in the literature. The algorithm utilized the concept of a staggered mesh in which the velocities are cell face centered and the properties of the fluid mixture are cell centered. This formulation permits the same computational index to be employed for both the cell properties and the cell component velocities. However, particular care must be exercised during the construction of the difference equations because the spatial locations of the computed variables within each cell are not coincident (see Figure 5). When the mesh incrementation is permitted to become infinitesimally small, the

finite difference approximations to the governing partial differential equations are consistent.

In FORTRAN IV, fractional and zero indices are prohibited. Consequently, the indices for the cell velocities were redefined. If the (i,j,k)-cell is specified, then the properties of the fluid are associated with the spatial coordinates of the cell center; the x-direction velocity is specified at the center of the right cellular face; the y-direction velocity is specified at the center of the back cellular face; the z-direction velocity is specified at the center of the upper cellular face. The velocities at the centers of the remaining cellular faces are identified by decrementing the indices associated with the respective spatial coordinate directions by 1, for example, $u(i-1,j,k)$ denotes the velocity component in the x-direction associated with the left cellular face of the (i,j,k)-cell. The remainder of this section is devoted to presenting each of the finite difference forms of the governing partial differential equations.

III.4.1 Conservation of Mass

The continuity equation, Eq (13), is the only equation to retain its conservative form. The time advanced value of the mixture density for any cell is then determined from the following difference equation:

$$\begin{aligned} \frac{\rho_{i,j,k}^{n+1} - \rho_{i,j,k}^n}{\Delta t} &+ \frac{(\rho u)_{i,j,k}^{n+1} - (\rho u)_{i-1,j,k}^{n+1}}{\Delta x} \\ &+ \frac{(\rho v)_{i,j,k}^{n+1} - (\rho v)_{i,j-1,k}^{n+1}}{\Delta y} \\ &+ \frac{(\rho w)_{i,j,k}^{n+1} - (\rho w)_{i,j,k-1}^{n+1}}{\Delta z} = 0 \end{aligned} \quad (59)$$

The mixed flux expressions (ρu) , (ρv) , and (ρw) are differenced in accordance with the SOLA-ICE algorithm. As an example, the quantity $(\rho u)_{i,j,k}^{n+1}$ is formulated as follows:

$$\begin{aligned}
 (\rho u)_{i,j,k}^{n+1} = & \frac{(1-\alpha)}{2} \left(\rho_{i+1,j,k}^n + \rho_{i,j,k}^n \right) u_{i,j,k}^{n+1} + \\
 & \frac{\alpha}{2} \left[\rho_{i+1,j,k}^n (u_{i,j,k}^{n+1} - |u_{i,j,k}^{n+1}|) + \right. \\
 & \left. \rho_{i,j,k}^n (u_{i,j,k}^{n+1} + |u_{i,j,k}^{n+1}|) \right] \quad (60)
 \end{aligned}$$

The remaining flux terms of Eq (59) are differenced similarly and index adjustments follow directly. The donor cell parameter, α , governs the amount of flux advection between adjacent cells; it is further constrained as follows:

$$\alpha = \begin{cases} 0, & \text{pure spatially centered differences} \\ 1, & \text{pure donor cell differences} \end{cases}$$

The donor cell terms are essentially upwind difference forms. The requirement to check the direction of the flow between cells is incorporated in the program without adding any conditional statements which slow the cycle computational time. The method as utilized in the SOLA-ICE algorithm and depicted in Eq (60) both adds and subtracts the absolute value of the time advanced velocity. Dependent upon the

direction of the fluid flow, the appropriate value of the density of the fluid is provided by the donor cell.

III.4.2 Conservation of Momentum

The three momentum conservation equations in non-conservative, primitive variable form, Eq (23), are approximated using a combination of donor cell and standard difference forms. Again, advection terms of the form $U_i U_{i,j}$ and $U_i U_{j,i}$ use the modified donor cell formulation, whereas the remaining terms use standard upwind or central difference forms as appropriate. The following cellular face centered flux expressions of the velocity gradients are provided to illustrate the methodology involved.

If the x-direction momentum equation is arbitrarily chosen, the following advection terms occur:

$$\left(u \frac{\partial u}{\partial x} \right)_{i,j,k}^n, \quad \left(v \frac{\partial u}{\partial y} \right)_{i,j,k}^n, \quad \left(w \frac{\partial u}{\partial z} \right)_{i,j,k}^n.$$

These terms, unlike those encountered in the continuity equation which was in conservative (divergence) form, are approximated in the following manner:

$$\begin{aligned} \left(u \frac{\partial u}{\partial x} \right)_{i,j,k}^n &= u_{i,j,k}^n \left(\frac{u_{i+1,j,k}^n - u_{i-1,j,k}^n}{2\Delta x} \right) (1 - \alpha) \\ &+ \alpha \left(\frac{u_{i+1,j,k}^n - u_{i,j,k}^n}{\Delta x} \right) \left(\frac{u_{i,j,k}^n - |u_{i,j,k}^n|}{2} \right) \\ &+ \alpha \left(\frac{u_{i,j,k}^n - u_{i-1,j,k}^n}{\Delta x} \right) \left(\frac{u_{i,j,k}^n + |u_{i,j,k}^n|}{2} \right) \quad (61) \end{aligned}$$

where $0 < \alpha < 1$.

The two remaining expressions,

$$\left(v \frac{\partial u}{\partial y} \right)_{i,j,k}^n \quad \text{and} \quad \left(w \frac{\partial u}{\partial z} \right)_{i,j,k}^n$$

are similarly approximated, however, the v and w velocity components are not defined in the spatial marching direction (in this case, the x -direction) and therefore require special attention. Only the u component velocity is defined in the x -direction and it is physically centered on both the left and right faces of any particular cell. Consequently, both v and w must be formed from the averages of the four v and w neighboring velocities in both the j -plane and k -plane respectively. These average velocities, \bar{v} and \bar{w} are defined as follows:

$$\bar{v}_{i,j,k}^n = \frac{(v_{i+1,j,k}^n + v_{i+1,j-1,k}^n + v_{i,j,k}^n + v_{i,j-1,k}^n)}{4} \quad (62)$$

$$\bar{w}_{i,j,k}^n = \frac{(w_{i+1,j,k}^n + w_{i+1,j,k-1}^n + w_{i,j,k}^n + w_{i,j,k-1}^n)}{4} \quad (63)$$

With these definitions of $\bar{v}_{i,j,k}^n$ and $\bar{w}_{i,j,k}^n$ the required difference expressions can therefore be formed analogously to Eq (61), that is,

$$\begin{aligned} v \frac{\partial u}{\partial y} \Big|_{i,j,k}^n &= \bar{v}_{i,j,k}^n \left(\frac{u_{i,j+1,k}^n - u_{i,j-1,k}^n}{2\Delta y} \right) (1 - \alpha) \\ &+ \alpha \left(\frac{u_{i,j+1,k}^n - u_{i,j,k}^n}{\Delta y} \right) \left(\frac{\bar{v}_{i,j,k}^n - |\bar{v}_{i,j,k}^n|}{2} \right) \\ &+ \alpha \left(\frac{u_{i,j,k}^n - u_{i,j-1,k}^n}{\Delta y} \right) \left(\frac{\bar{v}_{i,j,k}^n + |\bar{v}_{i,j,k}^n|}{2} \right) \end{aligned} \quad (64)$$

and,

$$\begin{aligned}
 \left(w \frac{\partial u}{\partial z} \right)_{i,j,k}^n &= \bar{w}_{i,j,k}^n \left(\frac{u_{i,j,k+1}^n - u_{i,j,k-1}^n}{2\Delta z} \right) (1 - \alpha) \\
 &+ \alpha \left(\frac{u_{i,j,k+1}^n - u_{i,j,k}^n}{\Delta z} \right) \left(\frac{\bar{w}_{i,j,k}^n - |\bar{w}_{i,j,k}^n|}{2} \right) \\
 &+ \alpha \left(\frac{u_{i,j,k}^n - u_{i,j,k-1}^n}{\Delta z} \right) \left(\frac{\bar{w}_{i,j,k}^n + |\bar{w}_{i,j,k}^n|}{2} \right) \quad (65)
 \end{aligned}$$

Eq (65) would be conceptually valid if the mesh in the z-direction was uniform, however, the mesh in this direction varied geometrically as prescribed by Eq (22). The proper form of the finite difference approximation for the advected gradient flow in the z-direction required replacement of the uniform mesh spatially centered and one-sided differences by the non-uniform mesh formulations of section III.2 .

Upon defining the quantities Δz^+ and Δz^- as follows,

$$\begin{cases} \Delta z^+ = z_c(k+1) - z_c(k) \\ \Delta z^- = z_c(k) - z_c(k-1) \end{cases} \quad (66)$$

Eq (65) was rewritten in the following form which is reducible to that for the uniform z-direction mesh when X is identically one,

$$\begin{aligned}
 \left(w \frac{\partial u}{\partial z} \right)_{i,j,k}^n &= \\
 \bar{w}_{i,j,k}^n &\left\{ \frac{u_{i,j,k+1}^n \Delta z^-}{\Delta z^+ (\Delta z^+ + \Delta z^-)} - \frac{u_{i,j,k-1}^n \Delta z^+}{\Delta z^- (\Delta z^+ + \Delta z^-)} \right\}
 \end{aligned}$$

$$\begin{aligned}
& + \frac{u_{i,j,k}^n (\Delta z^+ - \Delta z^-)}{\Delta z^+ \Delta z^-} \Bigg\} (1 - \alpha) \\
& + \alpha \left(\frac{u_{i,j,k+1}^n - u_{i,j,k}^n}{\Delta z^+} \right) \left(\frac{\bar{w}_{i,j,k}^n - |\bar{w}_{i,j,k}^n|}{2} \right) \\
& + \alpha \left(\frac{u_{i,j,k}^n - u_{i,j,k-1}^n}{\Delta z^-} \right) \left(\frac{\bar{w}_{i,j,k}^n + |\bar{w}_{i,j,k}^n|}{2} \right) \cdot (67)
\end{aligned}$$

The diffusive terms of the momentum equations were expanded according to the rules of differential calculus and subsequently differenced utilizing windward differences for the velocity derivatives and two-point, first order accurate property derivatives. For example, in the x-marching direction, the following approximations were made:

$$\left(\frac{\partial p}{\partial x} \right)_{i,j,k}^n = \frac{p_{i+1,j,k}^n - p_{i,j,k}^n}{\Delta x} \quad (68)$$

$$\left(\frac{\partial u}{\partial x} \right)_{i,j,k}^n = \frac{u_{i,j,k}^n - u_{i-1,j,k}^n}{\Delta x} \quad (69)$$

$$\left(\frac{\partial v}{\partial x} \right)_{i,j,k}^n = \frac{v_{i,j,k}^n - v_{i-1,j,k}^n}{\Delta x} \quad (70)$$

$$\left(\frac{\partial w}{\partial x} \right)_{i,j,k}^n = \frac{w_{i,j,k}^n - w_{i-1,j,k}^n}{\Delta x} \quad (71)$$

$$\left(\frac{\partial p}{\partial y} \right)_{i,j,k}^n = \frac{p_{i,j+1,k}^n - p_{i,j,k}^n}{\Delta y} \quad (72)$$

$$\left(\frac{\partial u}{\partial y} \right)_{i,j,k}^n = \frac{u_{i,j,k}^n - u_{i,j-1,k}^n}{\Delta y} \quad (73)$$

$$\left(\frac{\partial v}{\partial y}\right)_{i,j,k}^n = \frac{v_{i,j,k}^n - v_{i,j-1,k}^n}{\Delta y} \quad (74)$$

$$\left(\frac{\partial w}{\partial y}\right)_{i,j,k}^n = \frac{w_{i,j,k}^n - w_{i,j-1,k}^n}{\Delta y} \quad (75)$$

$$\left(\frac{\partial p}{\partial z}\right)_{i,j,k}^n = \frac{p_{i,j,k+1}^n - p_{i,j,k}^n}{\Delta z^+} \quad (76)$$

$$\left(\frac{\partial u}{\partial z}\right)_{i,j,k}^n = \frac{u_{i,j,k}^n - u_{i,j,k-1}^n}{\Delta z^-} \quad (77)$$

$$\left(\frac{\partial v}{\partial z}\right)_{i,j,k}^n = \frac{v_{i,j,k}^n - v_{i,j,k-1}^n}{\Delta z^-} \quad (78)$$

$$\left(\frac{\partial w}{\partial z}\right)_{i,j,k}^n = \frac{w_{i,j,k}^n - w_{i,j,k-1}^n}{\Delta z_k} \quad (79)$$

where Δz^+ and Δz^- are defined by Eq (66) and Δz_k is the vertical dimension of the (i,j,k)-cell. The variances in the formulations occur naturally from the staggered uniform-geometric mesh system which is utilized. Care must be exercised in forming the derivatives in the remaining two spatial marching directions. Some forms are identical to those listed above, whereas others are different and require additional inputs into the numerical simulation model. Incorporation of each of the above finite difference approximations and the remaining required difference forms not explicitly presented was easily accomplished for the set of momentum equations. The resultant algebraic expressions were explicitly solved for the time advanced values of the component cell velocities .

III.4.3 Conservation of Energy

The energy equation, Eq (25), was approximated by its finite difference counterpart in the same manner as were the momentum equations. In this case, however, the specific internal energy of each cell was donor-cell fluxed as were the advection terms of the momentum equations. Terms of the form,

$$\frac{\partial I}{\partial t} + u \frac{\partial I}{\partial x} + v \frac{\partial I}{\partial y} + w \frac{\partial I}{\partial z}$$

were approximated as follows for uniform meshes in each of the spatial directions utilizing the shorthand subscript notation whereby omitted indices are held constant:

$$\begin{aligned} & \frac{I_{i,j,k}^{n+1} - I_{i,j,k}^n}{\Delta t} + (1 - \alpha) \left\{ \left(\frac{u_i^{n+1} + u_{i-1}^{n+1}}{2} \right) \left(\frac{I_{i+1}^n - I_{i-1}^n}{2\Delta x} \right) \right\} \\ & + \frac{\alpha}{2} \left\{ \left[\frac{u_i^{n+1} + u_{i-1}^{n+1}}{2} - \left| \frac{u_i^{n+1} + u_{i-1}^{n+1}}{2} \right| \right] \left[\frac{I_{i+1}^n - I_i^n}{\Delta x} \right] + \right. \\ & \quad \left. \left[\frac{u_i^{n+1} + u_{i-1}^{n+1}}{2} + \left| \frac{u_i^{n+1} + u_{i-1}^{n+1}}{2} \right| \right] \left[\frac{I_i^n - I_{i-1}^n}{\Delta x} \right] \right\} \\ & + (1 - \alpha) \left\{ \left(\frac{v_j^{n+1} + v_{j-1}^{n+1}}{2} \right) \left(\frac{I_{j+1}^n - I_{j-1}^n}{2\Delta y} \right) \right\} \\ & + \frac{\alpha}{2} \left\{ \left[\frac{v_j^{n+1} + v_{j-1}^{n+1}}{2} - \left| \frac{v_j^{n+1} + v_{j-1}^{n+1}}{2} \right| \right] \left[\frac{I_{j+1}^n - I_j^n}{\Delta y} \right] + \right. \\ & \quad \left. \left[\frac{v_j^{n+1} + v_{j-1}^{n+1}}{2} + \left| \frac{v_j^{n+1} + v_{j-1}^{n+1}}{2} \right| \right] \left[\frac{I_j^n - I_{j-1}^n}{\Delta y} \right] \right\} \end{aligned}$$

$$\begin{aligned}
& + (1 - \alpha) \left\{ \left(\frac{w_k^{n+1} + w_{k-1}^{n+1}}{2} \right) \left(\frac{I_{k+1}^n - I_{k-1}^n}{2\Delta z} \right) \right\} \\
& + \frac{\alpha}{2} \left\{ \left[\frac{w_k^{n+1} + w_{k-1}^{n+1}}{2} - \frac{|w_k^{n+1} + w_{k-1}^{n+1}|}{2} \right] \left[\frac{I_{k+1}^n - I_k^n}{\Delta z} \right] + \right. \\
& \left. \left[\frac{w_k^{n+1} + w_{k-1}^{n+1}}{2} + \frac{|w_k^{n+1} + w_{k-1}^{n+1}|}{2} \right] \left[\frac{I_k^n - I_{k-1}^n}{\Delta z} \right] \right\} \quad (80)
\end{aligned}$$

However, since a geometrically varying mesh was utilized in the z -direction, the spatially centered z -derivatives must be approximated with the formulation presented in section III.2, and the increment Δz replaced by either Δz^+ or Δz^- in the windward differences as appropriate.

The remaining terms of the energy equation, including both components of the heat flux, were approximated in the same manner as were the diffusive terms of the momentum equations. The conductive components of the heat flux terms were obtained by expanding the tensorial form and carrying out the indicated differentiations and then replacing each component by its spatially centered finite difference form. Those forms in the z -direction were appropriately modified to account for the geometric mesh variation. The diffusive transport of enthalpy term,

$$\left(\sum_k^N G_{\text{diff } k} \cdot h_k \right)_{,j} \quad (81)$$

was first simplified for a binary gas mixture and rewritten as,

$$(G_{diff\ 1} [h_2 - h_1]),_j \quad (82)$$

where $G_{diff\ 1}$ is the diffusive flux of species "1" and h_1 and h_2 are the specific enthalpies of species "1" and species "2" respectively. The last expression was then expanded utilizing the definition of $G_{diff\ 1}$, that is,

$$G_{diff\ 1} = -\rho D \frac{\partial m_1}{\partial x_j}$$

where $D = D_{12} = D_{21}$ for a binary gas mixture and where m_1 is the mass fraction of species "1" gas, resulting in the following form which was then approximated by finite difference expressions:

$$\begin{aligned} & \rho D \left\{ \frac{\partial (h_2 - h_1)}{\partial x} \frac{\partial m_1}{\partial x} + \frac{\partial (h_2 - h_1)}{\partial y} \frac{\partial m_1}{\partial y} + \frac{\partial (h_2 - h_1)}{\partial z} \frac{\partial m_1}{\partial z} \right\} \\ & + (h_2 - h_1) \left\{ \frac{\partial \rho D}{\partial x} \frac{\partial m_1}{\partial x} + \frac{\partial \rho D}{\partial y} \frac{\partial m_1}{\partial y} + \frac{\partial \rho D}{\partial z} \frac{\partial m_1}{\partial z} \right\} \\ & + \rho D (h_2 - h_1) \left\{ \frac{\partial^2 m_1}{\partial x^2} + \frac{\partial^2 m_1}{\partial y^2} + \frac{\partial^2 m_1}{\partial z^2} \right\} \end{aligned} \quad (83)$$

The derivatives of the product (ρD) were not expanded further, but rather, retained in this form since the gradients of this quantity would pose less difficulty in numerically evaluating them as would evaluating each of the expanded gradient terms separately. Additionally, the spatially centered and one-sided derivative terms in the z-direction were modified accordingly to account for the geometric variation of the mesh in that coordinate direction.

III.4.4 Conservation of Species

The conservation of species partial differential equation for the k^{th} species, Eq (22), was also approximated by a corresponding finite difference equation. In this case, the differencing was formulated similarly to that of the advection terms of the energy equation utilizing the donor-cell forms developed earlier for the SOLA-ICE algorithm. Rivard, Butler, and Farmer (Ref 46) also utilized difference forms for the species conservation equation which were handled similarly to those they developed for their energy conservation equation; however, their program (RICE) was not donor cell fluxed.

The general form of this conservation equation which temporarily includes the source terms from chemical reactions to show all contributory effects is written as follows:

$$(\rho_k)_{,t} + \underbrace{(\rho_k U_j)_{,j}}_{\text{advection}} = \underbrace{(\rho D_{m_{k,j}})_{,j}}_{\text{diffusion}} + \underbrace{S_k}_{\text{source}} \quad (84)$$

The actual finite difference construction to represent this partial differential equation was accomplished in two steps after neglecting any and all source terms. Firstly, the advective fluxing was modeled in the same manner as the global energy advection terms employing the donor-cell methodology. Secondly, the diffusive fluxes were modeled similarly to the stress tensor terms of the momentum equations. The partial derivative expansions for both the advective and diffusive terms are presented respectively as follows:

Advection :

$$(\rho_k U_j)_{,j} =$$

$$\rho_k \left[\frac{\partial u}{\partial x} + \frac{\partial v}{\partial y} + \frac{\partial w}{\partial z} \right] + u \frac{\partial \rho_k}{\partial x} + v \frac{\partial \rho_k}{\partial y} + w \frac{\partial \rho_k}{\partial z} \quad (85)$$

Diffusion :

$$(\rho \mathcal{D} m_{k,j})_{,j} =$$

$$\begin{aligned} & \left(\frac{\partial \rho \mathcal{D}}{\partial x} \right) \left(\frac{\partial m_k}{\partial x} \right) + \left(\frac{\partial \rho \mathcal{D}}{\partial y} \right) \left(\frac{\partial m_k}{\partial y} \right) + \left(\frac{\partial \rho \mathcal{D}}{\partial z} \right) \left(\frac{\partial m_k}{\partial z} \right) \\ & + \rho \mathcal{D} \left[\frac{\partial^2 m_k}{\partial x^2} + \frac{\partial^2 m_k}{\partial y^2} + \frac{\partial^2 m_k}{\partial z^2} \right] \end{aligned} \quad (86)$$

As in the global energy equation, the quantity $(\rho \mathcal{D})$ was treated as a property of the fluid and difference expressions were computed accordingly for both the uniform and geometrically varying meshes in the respective spatial coordinate directions.

III.4.5 Boundary Conditions

The "no slip", continuative outflow, and prescribed inflow boundary conditions were implemented through the use of "dummy cells" as opposed to using higher order difference approximations. The "no-slip" condition on the injection surface required that the following sub-conditions be strictly enforced:

- (1). the normal velocity vanish on the surface, and,
- (2). the tangential velocities vanish on the surface.

Implementation of the boundary conditions associated with the upper surface of the computational domain was accomplished in two steps. The first step covered the entire upper surface with a "no-slip" boundary which was physically accomplished by the following mechanism:

$$\begin{aligned}
 w(i,j,k_{\max}-1) &= 0, \text{ for every } i,j \\
 u(i,j,k_{\max}) &= -u(i,j,k_{\max}-1), \text{ for every } i,j \\
 v(i,j,k_{\max}) &= -v(i,j,k_{\max}-1), \text{ for every } i,j
 \end{aligned}
 \tag{87}$$

Additionally, the variables, ρ and I , were constrained to enforce the adiabatic wall by the following numerical prescription:

$$\begin{aligned}
 I(i,j,k_{\max}) &= I(i,j,k_{\max}-1), \text{ for every } i,j \\
 \rho(i,j,k_{\max}) &= \rho(i,j,k_{\max}-1), \text{ for every } i,j
 \end{aligned}
 \tag{88}$$

The second step redefined the variables at the jet orifice to conform to the prescribed jet inflow values. Each of the affected variables was overwritten with the requisite exhaust jet data.

The windward face of the computational domain was similarly manipulated to enforce the prescribed boundary defined by the aircraft altitude and Mach number. The parameters in the $(1,j,k)$ and $(2,j,k)$ locations were enforced to equal one another for every "j,k" in the domain for all time. This numerical prescription embodies the assumption that the windward face is sufficiently far upstream to be unaffected by the flow injection and interaction downstream. In all

cases examined, this boundary was physically placed to ensure that this assumption was valid. The ambient conditions enforced on this boundary were obtained from the atmosphere subroutine described in Appendix A which details the 1962 Standard atmosphere properties as a function of aircraft pressure altitude.

The remaining boundaries, all of which are continuative outflow, were prescribed initially as follows:

Front Lateral Face :

$$\begin{aligned} v(i,1,k) &= v(i,2,k) , \text{ for every } i,k \\ u(i,1,k) &= u(i,2,k) , \text{ for every } i,k \\ w(i,1,k) &= w(i,2,k) , \text{ for every } i,k \\ P(i,1,k) &= P(i,2,k) , \text{ for every } i,k \end{aligned} \quad (89)$$

where P is any property of the fluid mixture, e.g. I , etc.

Back Lateral Face :

$$\begin{aligned} v(i,j_{\max}-1,k) &= v(i,j_{\max}-2,k) , \text{ for every } i,k \\ u(i,j_{\max},k) &= u(i,j_{\max}-1,k) , \text{ for every } i,k \\ w(i,j_{\max},k) &= w(i,j_{\max}-1,k) , \text{ for every } i,k \\ P(i,j_{\max},k) &= P(i,j_{\max}-1,k) , \text{ for every } i,k \end{aligned} \quad (90)$$

Lower Face :

$$\begin{aligned}
w(i,j,1) &= w(i,j,2) , \text{ for every } i,j \\
u(i,j,1) &= u(i,j,2) , \text{ for every } i,j \\
v(i,j,1) &= v(i,j,2) , \text{ for every } i,j \\
P(i,j,1) &= P(i,j,2) , \text{ for every } i,j
\end{aligned} \tag{91}$$

Leeward Face :

$$\begin{aligned}
u(\text{imax}-1,j,k) &= u(\text{imax}-2,j,k) , \text{ for every } j,k \\
v(\text{imax},j,k) &= v(\text{imax}-1,j,k) , \text{ for every } j,k \\
w(\text{imax},j,k) &= w(\text{imax}-1,j,k) , \text{ for every } j,k \\
P(\text{imax},j,k) &= P(\text{imax}-1,j,k) , \text{ for every } j,k
\end{aligned} \tag{92}$$

After the solution advanced through both the pressure iteration phase of each computational time cycle and the subsequent solution of the momentum equations, the continuative boundary conditions were imposed.

III.5 Stability Requirements

To ensure the stability of the numerical algorithm, the three following constraints were strictly enforced during each time step and for every cell within the computational domain:

- (1). The fluid must not travel a distance greater than any cell dimension,
- (2). The fluid momentum must not diffuse a distance greater than any cell dimension, and,

- (3). The fluid energy must not diffuse a distance greater than any cell dimension.

Explicit mathematical expressions for these limits, with the exception of the mass transport limit, are not possible to formulate for the coupled non-linear differential equations of the model. However, when the momentum and energy equations were approximated by the corresponding pure diffusion counterparts, Cloutman et al (Ref 44) provided two-dimensional mean flow expressions derived from von Neumann stability analyses which were easily extended to fully three-dimensional turbulent flows comprised of one fluid species. These expressions which are meant to serve only as guides and not exact mathematical prescriptions are presented as follows:

x-momentum :

$$\left\{ \frac{\alpha}{2} \left[\frac{|u|}{\Delta x} \Big|_{\max} + \frac{|v|}{\Delta y} \Big|_{\max} + \frac{|w|}{\Delta z} \Big|_{\max} \right] + \frac{\mu_{\text{eff}}}{\rho} \left[\frac{4}{3} \frac{1}{\Delta x^2} + \frac{1}{\Delta y^2} + \frac{1}{\Delta z^2} \right] \right\} \Delta t < \frac{1}{2} \quad (93)$$

y-momentum :

$$\left\{ \frac{\alpha}{2} \left[\frac{|u|}{\Delta x} \Big|_{\max} + \frac{|v|}{\Delta y} \Big|_{\max} + \frac{|w|}{\Delta z} \Big|_{\max} \right] + \frac{\mu_{\text{eff}}}{\rho} \left[\frac{1}{\Delta x^2} + \frac{4}{3} \frac{1}{\Delta y^2} + \frac{1}{\Delta z^2} \right] \right\} \Delta t < \frac{1}{2} \quad (94)$$

z-momentum :

$$\left\{ \frac{\alpha}{2} \left[\frac{|u|}{\Delta x} \Big|_{\max} + \frac{|v|}{\Delta y} \Big|_{\max} + \frac{|w|}{\Delta z} \Big|_{\max} \right] + \frac{\mu_{\text{eff}}}{\rho} \left[\frac{1}{\Delta x^2} + \frac{1}{\Delta y^2} + \frac{4}{3\Delta z^2} \right] \right\} \Delta t < \frac{1}{2} \quad (95)$$

energy :

$$\left\{ \frac{\alpha}{2} \left[\frac{|u|}{\Delta x} \Big|_{\max} + \frac{|v|}{\Delta y} \Big|_{\max} + \frac{|w|}{\Delta z} \Big|_{\max} \right] + \frac{\gamma}{Pr_t} \frac{\mu_{\text{eff}}}{\rho} \left[\frac{1}{\Delta x^2} + \frac{1}{\Delta y^2} + \frac{1}{\Delta z^2} \right] \right\} \Delta t < \frac{1}{2} \quad (96)$$

As the direct result of numerical experimentation undertaken to verify the utility of the above expressions, it was observed that a time increment less than or equal to one-fourth the value obtained by satisfying the cellular mass transport constraint, that is,

$$t \leq \min \left\{ \frac{\Delta x}{|u|}, \frac{\Delta y}{|v|}, \frac{\Delta z}{|w|} \right\} \quad (97)$$

provided an effective means to determine the proper temporal increment to ensure numerical stability. If this time step when substituted in the stability analysis equations defined above results in a donor-cell parameter value which exceeds its constraint, that is $\alpha > 1$, then the temporal increment must be decreased such that the donor-cell, momentum, and energy constraints are satisfied simultaneously.

Because of the violent nature of the high-speed injection and associated viscous flow interactions, the coarseness of the vertical grid directly affected the stability of the numerical solution. For high Mach number crossflows (0.7) with respect to the jet injection Mach number (0.24), a cell stretch factor up to and through 1.2 provided accurate and stable solutions. However, for low Mach number crossflows (0.125) with respect to the jet injection Mach number (0.5), a stretch factor of 1.1 was too large. In the latter case, a stretch factor of 1.05 proved to be small enough to capture the essential near field mixing and to guarantee both the accuracy and stability of the numerical solution. From this discussion, it should be obvious that each injection problem must be carefully analyzed on a case by case basis and that those parameters which can be altered to affect stability must be "tuned" for each problem.

III.6 Convergence Criteria

The cost of solving three-dimensional fluid flow problems is exorbitant and consequently suitable criteria are required to determine when to cease numerical computations. Simply restated, there exists a point in time beyond which the marginal returns from additional computations do not offset the increased cost of acquiring additional information. Many authors have used the criterion of the asymptotic approach to "steady state" of the fluid density from one time step to the next whereby the difference in density is less than some arbitrarily prescribed increment. However, the jet-crossflow interaction problem for real gases required that some criterion be established to determine not only when the change in density was less than some prescribed value,

but also, when the flow field was firmly established to accurately permit computation of the jet trajectory. The criterion chosen to accomplish both of these requirements was the asymptotic change in kinetic energy of the computational domain from one time step to the next being less than some prescribed value. This criterion is mathematically expressed as

$$\frac{(\text{Kinetic Energy})^{n\Delta t} - (\text{Kinetic Energy})^{(n+1)\Delta t}}{(\text{Kinetic Energy})^{t_0}} < \epsilon \quad (98)$$

where ϵ is an arbitrarily small positive value.

This criterion alone is insufficient to determine the "steady-state" solution to the problem because of both the oscillatory behavior of the kinetic energy and the small temporal increments utilized. Local maxima and minima erroneously would indicate convergence by satisfying Eq (98) when obviously it did not exist. If termination of the computations occurred too soon based upon the information contained within the numerical transient solutions, meaningful information concerning the flowfield and its associated properties would not be available. However, by specifying some meaningful minimum time to terminate computations based upon the dynamics of the simulation model, this pitfall was easily avoided.

The time required for a disturbance introduced into the computational domain to decay to negligible levels is directly related to the characteristic time of the computational domain which is defined as follows:

$$t_{\text{char}} = \frac{L}{U_{\infty}} \quad (99)$$

where L is the length of the computational domain, and,

where U_{∞} is the magnitude of the freestream velocity.

It was observed that depending upon the coarseness of the computational grid, the measure of convergence specified by Eq (98) was obtained by at least one characteristic time. For the coarse grids, the required convergence level was attained within two characteristic times. Consequently, when Eq (99) was utilized in conjunction with some multiple of t_{char} as the cutoff time, termination of the computations was effectively accomplished with essentially no additional information to be gained from additional computational effort. These criteria were employed on numerical experiments involving variable property air-air, helium-air, and gas mixture-air jet injection problems at elevated temperatures (1500°K) with outstanding success.

III.7 Summary

The computational domain defined in Section II was divided into a large, but finite, number of rectangular cells, the vertical dimensions of which were prescribed to vary geometrically from the injection surface. The unique finite difference forms required to approximate the terms of the non-linear governing partial differential equations as implemented by the SOLA-ICE algorithm (Ref 44) and as modified to account for the non-uniform mesh in the z -direction were presented. The required equivalent spatially "centered" and one-sided difference forms for both the first and second partial derivatives were derived by

utilizing Taylor series expansions of several variables. The staggered mesh employed by the algorithm presented additional complexity to the modeling as the spatial locations of variables with the same indices were not coincident; consequently, the necessary modifications to the finite difference approximations utilized by the algorithm were presented. The boundary conditions were easily implemented through the use of "dummy" cells which surrounded the computational domain as opposed to the use of higher order, multi-point difference approximations thereby increasing the computational speed by the reduction in complexity afforded by this method.

Since a modified donor-cell formulation was used, the algorithm required the strict enforcement of the constraints that no cellular mass, momentum, or energy diffuse a distance greater than any cell dimension during any given time step for each and every cell within the computational domain. Explicit numerical stability expressions derived from von Neumann stability analyses of the two-dimensional pure diffusion counterparts of the momentum and energy equations (Ref 44, Eqs (52)-(54)) were expanded for three-dimensional turbulent flows. The rationale for choosing the extremely successful convergence criterion for this problem, the asymptotic approach to "steady-state" of the change in kinetic energy of the computational domain from one time step to the next, in conjunction with a computational cutoff time based on some multiple of the domain characteristic time was also detailed. The results of the research of the jet-crossflow interaction problem for real gases at elevated temperatures are presented in the next section.

IV. Results of the Numerical Simulation

This section describes the numerical solution of the jet injection-freestream interaction for the chemical laser exhaust gas mixture described in Table I as well as for both pure helium and air jets constrained by the same parameters defining the problem, that is, the Mach numbers of both the jet and the freestream, the ratio of jet to freestream dynamic pressure, and the jet injection temperature were fixed. Numerical analyses demonstrated that the trajectories and general characteristics of the flowfields of the jet-crossflow interaction were essentially unaffected by the turbulent diffusivities associated with the thermal conductivity and the mass transfer binary diffusion coefficient. Consequently, the isopleths from the simulations with molecular values for thermal conductivity and binary diffusion coefficient for the AFWL gas mixture, helium and air injection studies were presented as the trajectories were more easily perceived as well as numerically obtained. Section IV.5 contains the discussion of the effects induced on the heat transfer to the injection surface by the incorporation of the energy transport diffusivities associated with the turbulent nature of the flow interaction. To verify the methodology of the algorithm, numerical simulations were conducted for an air jet injected vertically upwards into a subsonic crossflow from a rectangular jet orifice with an aspect ratio of 4.0 and with a jet to freestream velocity (Mach) ratio of 4.0 (equivalently, a Q ratio of 16) for which experimental flowfield data existed and from which direct comparisons could then be made.

IV.1 Verification of the Numerical Algorithm

The experimental normally upwards injection tests conducted by Weston and Thames (Ref 26) at NASA/Langley for an aspect ratio 4.0 jet with the major axis of the orifice aligned with the streamwise flow was numerically simulated as indicated in Figure 6. The boundary conditions for the computational domain were identical to those already discussed for the downwardly ejecting jet except for the fact that the upper and lower surfaces were interchanged such that the adiabatic "no-slip" injection surface was located on the bottom surface through which the jet was forcibly constrained to be ejected into the Mach 0.125 crossflow at essentially freestream (tunnel) static temperature and pressure. The particular test runs chosen were for a jet to freestream velocity ratio, R , equal to 4.0 and for a jet injection angle of 90 degrees. These data were for the lowest values of R experimentally investigated and were therefore more nearly representative of the real gas injection problem which was to be simulated.

The actual tests were accomplished over a time span of several months, consequently, test conditions varied with the climatic conditions prevalent during each test. The numerical simulation mathematically replicated the injection tests from the reflection plane injection surface of dimension $12D_e$ by $24D_e$ where D_e is the equivalent diameter of the rectangular jet. Additionally, average values of the tunnel static temperature (281.76°K) and pressure ($2130 \text{ lb}_f/\text{ft}^2$) were utilized while constraining the crossflow (tunnel) velocity to be 138 feet per second. Actual experimental flowfield data were provided by Weston to facilitate direct numerical comparison with the mathematical simulation.

IV.1.1 Numerical Solution : Convergence

The experimental tests for $R=4$ were numerically simulated using both a coarse mesh of $29 \times 15 \times 17$ cells in the x , y , and z spatial directions respectively on the CDC Cyber 175 at Wright-Patterson AFB and a more refined mesh of $29 \times 29 \times 26$ cells in the x , y , and z directions respectively on the CDC 7600 at the Air Force Weapons Laboratory, Kirtland AFB, New Mexico. Because the experimental jet was both narrow and small, the jet orifice was modeled by 2×1 cells in the x and y spatial directions respectively in the coarse and refined mesh simulations. Additionally, in each case, a geometric stretch factor, K , of 1.05 was employed to expand the vertical cell dimension from the injection surface; however, the initial cell vertical dimension for the refined mesh was one-half that of the corresponding value of the coarse mesh. Only the fine mesh simulation replicated the actual experimental injection plane dimensions.

As alluded to in Section III.5, the numerical stability was directly affected by the magnitude of the geometric stretch factor. For the coarse grid check case, a K value of 1.1 resulted in a solution which initially appeared to be periodic with time. The convergence plot of this case is presented in Figure 7. After approximately five (5) characteristic times, the periodicity of the solution was firmly established. However in the process of verifying and analyzing the numerical solution, another coarse grid test simulation was made with a K value equal to 1.05. As is evidenced by Figure 8, the "periodic" solution which was apparent for the larger K factor did not recur, but rather, the asymptotic approach to steady state resulted after approximately two (2) characteristic times. When the mesh was further

refined by both halving the initial cell vertical dimension and increasing the number of cells within the computational domain, the solution exhibited an acceptable level of convergence within approximately one (1) characteristic time.

IV.1.2 Numerical Solution : Results

The numerical simulation of Weston's experimental test for a normally injected air jet with $R=4$ produced results which were in agreement with those observed in the wind tunnel. As the jet penetrated the crossflow, it was deflected downstream and in the process, a pair of counter-rotating vortices were formed which also were swept downstream. Figures 10a through 10e depict the numerically computed flowfield in adjacent y-planar cuts through the computational domain where Figure 10a is situated two cells to the left of the jet symmetry plane. As the sweep is made from this plane, through the symmetry plane, and finally concluding with the plane two cells to the right of the symmetry plane (Figure 10e), the physical nature of the jet-crossflow interaction is readily observed. Behind the jet, a wake region with a small recirculation zone is observed which entrains low velocity air near the reflection plane into the jet plume. As the lateral distance from the sides of the jet is increased, the flowfield demonstrates less influence from the relatively high speed jet injection and the velocity tends to return to freestream values.

As Weston's data are the only known experimental flowfield data for rectangular jets being injected into crossflows, it was imperative that specific data be compared to ascertain the accuracy of the numerical solution of the jet-crossflow interaction. The symmetry plane was

chosen because of the additional analysis provided by Weston and Thames in deriving empirical least squares determined expressions for the jet trajectory (based on maximum total pressure) as well as for the locus of centers for the counter-rotating vortex pair (Ref 26, Eq 1 and Table 2). Figure 11 is a vector plot of experimental wind tunnel data (solid vectors) and flowfield data from the refined mesh numerical simulation (dotted vectors) for the jet injection symmetry plane. Since the spatial locations of the test data were not coincidental with those of the simulation, a two-dimensional linear interpolation routine was used to acquire simulation data at the requisite experimental test locations. Excellent agreement was obtained for data along the jet trajectory both in angular orientation and in magnitude. It was disconcerting to observe that the empirical velocity centerline curve also plotted in Figure 11 demonstrated approximately the same slope as the velocity field generated by the numerical solution while the experimental data upon which the empirical curve was based showed marked deviation. However, the least squares analysis performed by Weston and Thames in deriving the trajectory equation was based upon the flowfield data of the exhaust plume in the symmetry plane as well as adjacent lateral planes. Consequently, the empirical expression more closely portrays the actual macroscopic plume behavior. The experimental values of the velocities obtained by the first probe on the rake (highest Z/D_e value) had the greatest distortion induced measurement error. Other near field data did not offer the same degree of agreement as did either the far field or jet trajectory data. The empirically derived curve for the locus of centers of the vortex pair is also presented within the same

figure. It is readily apparent that the data acquired during the experimental phase were more heavily weighted in favor of determining the structure of the vortex pair than determining the jet centerline based on maximum velocity. Because of the paucity of experimental flowfield data on or near the jet trajectory in conjunction with the probe errors induced by the large gradients over the probe orifice in the near field region, the experimental data immediately above and below the empirical curve in Figure 11 were quantitatively compared both in magnitude and flow orientation with the corresponding data from the simulation. The magnitudes of the velocities in the streamwise direction above and below the trajectory in Region I of the figure were underpredicted by the simulation by 7.4 and 12 per cent respectively. The local flow inclination angles from the simulation were 7.9 and 9.5 degrees respectively; the corresponding experimental angles were -0.8 and 1.3 degrees. The inclination of the empirical curve was 19.3 degrees at the intersection of the rake probe axis with the trajectory. Similar data for Region II of the same figure shows that the simulation underpredicted the magnitudes of the streamwise velocities by 2.3 and 8.4 per cent for the upper and lower data respectively. The corresponding local angular orientations varied between 5.9 and 7.3 degrees from the simulation versus the experimentally obtained -2.4 and 1.0 degrees while the inclination of the empirical curve is approximately 16.9 degrees at the intersection of the trajectory and the rake axis. In both regions along the empirically derived curve for the jet trajectory, it is readily observed that the numerical simulation more closely replicates the trends exhibited in the curve than do the experimental data for the symmetry plane.

To demonstrate the effects of the mesh cell sizing on the numerical resolution, Figure 12 is presented which depicts the flowfield in the symmetry plane from the coarse grid simulation. The same general flow pattern as in Figure 10c was discerned but not to the same level of accuracy. However, the same small recirculation zone entrainment of low velocity air near the injection plane was still observed as well as was the same wake behavior of the jet-crossflow interaction downstream of the jet.

Weston and Thames presented pressure coefficient (C_p) data for the rectangular jet aligned with the flow (Ref 26, Figure 6b). However, their presentation was for the ΔC_p derived by subtracting C_p data with the jet off from the corresponding values with the jet on. Despite the fact that the numerical simulation was not optimized to obtain surface pressure distributions, that is, the grid was still too coarse even in the refined mesh case, results were obtained which were nearly in agreement with experimental surface pressure measurements. Figure 13a depicts C_p contour data derived from the mathematical simulation. A large wake region (negative C_p) exists laterally and downstream of the jet while a small positive pressure region exists immediately upstream of the jet. The vortex structure is also observed from this figure as well as is the characteristic kidney shape of each C_p contour.

Figure 13b shows the C_p contour data for the wake region which Weston and Thames included in Reference 26. The C_p jet off values which they subtracted out in their presentation varied between +0.03 with two anomalous variations of magnitude 0.05 in C_p . Essentially, the data contained in their presentation are equivalent to the data in Figure

13a; however, the ambient temperature and pressure at which the experimental data were obtained are not known. Both figures demonstrate similar behavior with the experimental values exhibiting more pronounced and intense variations. To quantify the comparison between the experimental and analytical results, C_p data for a streamwise station $X/D_e = 0.0$ which were provided by Weston were depicted in Figure 13c with the corresponding data derived from the simulation. This figure shows what appears to be a constant difference acting in conjunction with a rotation in the data. Because of the velocity averaging scheme employed in the simulation, such an aberration in the data is entirely consistent with the coarseness of the mesh which was utilized. As the lateral distance increases, both sets of data demonstrate the same trend.

Another similar experiment conducted by D. J. Peake (Ref 47) experimentally measured the surface pressure distribution on the bottom surface of a wing in which an aspect ratio 4.0 rectangular jet was embedded with the major axis aligned with the streamwise flow. The R values for his tests were fortuitiously 4.0 and 4.1; the crossflow velocities were 60 and 120 feet per second, respectively. Figures 14a and 14b were reproduced from Peake's work (Ref 47, Figures 10a and 10e) and depict the pressure coefficient contours experimentally determined on the flat region of the lower wing surface. The quantity which Peake used to nondimensionalize the spatial locations was not the equivalent diameter of the rectangular orifice but rather was the square root of the orifice area.

The flow over the wing surface in which Peake embedded the

rectangular jet was affected by the upstream planform geometry, the effects of which became more pronounced as the crossflow velocity was increased while maintaining the R value. Because the crossflowing airstream was subsonic (60 and 120 feet per second), distortions of the pressure coefficient contours induced by the upstream and finite edge conditions associated with the experimental apparatus negated meaningful comparisons between the experimental and analytical data for regions outside the near wake zone. To that end, comparisons were made for X/D_e and Z/D_e pairs (2.25,1.1) and (2.75,1.0) for which the analytically determined C_p values were 0.25 and 0.20 respectively (see Figure 13). At the corresponding locations in Peake's non-dimensional terminology, (2.54,1.24) and (3.10,1.13) respectively, it was observed from Figure 14a that for a crossflow velocity of 60 feet per second the corresponding values of the pressure coefficient were 0.25 (nominal difference) and 0.20 (nominal difference). Whereas in Figure 14b at the same prescribed coordinates, the corresponding values of C_p were 0.30 and 0.24 with associated differences of +20 per cent each. The larger discrepancies accompanying the increase in crossflow velocity (120 feet per second) can not be attributed only to the slight increase in R (4.1 vice 4.0) although there is necessarily some tangible effect. The effect of the flat plate injection surface on the flowfield as pointed out by Weston and Thames (Ref 26) is not as benign as previously thought. Therefore, a modified wing surface with only a small region of negligible curvature is even more insidious. Additionally, Fearn and Weston (Ref 48) have shown that errors in comparisons between corresponding C_p contours on the surface of a flat plate in regions of

low pressure gradients for two identical experiments at the same set of conditions can very easily vary in spatial orientation by as much as an equivalent diameter. Consequently, the overall agreement between the simulation and the experiment is even further enhanced.

Perhaps the most information regarding the surface pressure distribution was obtained from Figure 15 which presents a three-dimensional C_p surface plot for the injection plane and the associated contour plot of it projected onto the x-y plane beneath it. The surface plot demonstrates the typical flat plate pressure distribution which is characterized by a pressure rise at the leading edge which decays rapidly to a null value. Just ahead of the jet, a positive pressure region exists which abruptly becomes negative aft of the jet orifice. A pressure disturbance issues forth laterally from the sides of the jet which rapidly decays prior to reaching the lateral plate boundaries. Also observable from the figure is a positive pressure region aft of the jet which forms a "spine-like" surface which gradually dissipates over the entire remaining length of the injection plane. This turbulent region was also observed by Weston in the wind tunnel (Ref 49) but unfortunately it was never measured quantitatively. In the contour plane, a contour of this positive C_p zone is displayed as are the characteristic kidney shapes of the wake region and the positive C_p region contours ahead of the jet.

IV.2 Airborne Chemical Laser Exhaust

The analysis of the high temperature (1500 °K) exhaust gases generated by an airborne chemical laser and subsequently discharged from an aspect ratio 1.75 rectangular jet orifice embedded in the aft lower

surface of a wide-bodied air vehicle fuselage into the high subsonic ($M=0.7$) ambient crossflow at a pressure altitude of 11 kilometers (tropopause) is presented within this subsection. The computational domain and the requisite finite difference formulations of both the governing equations and the boundary conditions have been described in Sections II and III. The inherent differences between this study and that previously conducted to verify the algorithm, that is, the vertical isothermal air injection problem for $R=4$, are significant. This case (and the succeeding ones) involved a high temperature subsonic rectangular jet being injected into a cold crossflowing gas not necessarily comprised of the same species as that of the injectant. The Q ratio was also markedly different; Q for this and the subsequent studies was constrained to the value of 0.15 while the corresponding Q value for the Weston experiment was 16. Additionally, the scales of both problems differed appreciably. For example, the boundary layer thickness upstream of the high temperature jet was approximately equal to $D/14$ where D is the streamwise dimension of the rectangular jet; in Weston's experiment, the corresponding upstream boundary layer thickness was approximately $D/36$ where D again is the streamwise dimension of the rectangular jet. However, the boundary layer thickness associated with the simulations for hot gaseous injectants was two orders of magnitude greater than that of the isothermal case. In dimensional terms, the actual boundary layer thickness was approximately 0.3 meters for the airborne chemical laser simulations.

IV.2.1 Numerical Solution : Convergence

The numerical simulation of the exhaust jet-crossflow interaction

was accomplished for both coarse and refined subdivisions of the computational domain. The coarse mesh simulation conducted on the CDC Cyber 175 at Wright-Patterson AFB utilized $29 \times 13 \times 13$ cells in the x, y, and z spatial coordinate directions while the refined mesh simulation conducted on the CDC 7600 at Kirtland AFB used $42 \times 21 \times 23$ cells in the corresponding spatial directions. The jet orifice was modeled by 4×2 and 5×3 cells in the x and y directions for the coarse and refined meshes respectively. The K factors controlling the geometrically varying z-dimension of each cell from the injection surface were 1.20 and 1.09 for the coarse and refined mesh simulations. Despite the large value of K utilized by the coarse mesh simulation which was required to ensure that the near field mixing processes were essentially captured within the computational domain, the criterion to establish convergence (Figure 16) exhibited both numerical stability and the associated approach to steady-state after approximately two (2) characteristic times. The corresponding data for the refined mesh (Figure 17) exhibited an acceptable level of convergence within one (1) characteristic time. As is evidenced by Figure 17, the convergence of the solution was accelerated by the modification of the three factors which governed both the stability and accuracy of the algorithm, and consequently, of the numerical solution. From time $t=0$ to approximately $t=0.03$ seconds, the donor-cell parameter was equal to 0.7, the over-relaxation factor was 1.4, and the temporal increment was equal to 0.00015 seconds. Because the magnitude of the change in domain kinetic energy was relatively large at this point and the associated time to decay to approximate steady-state conditions would invariably exceed the

allocated computational resources on the CDC 7600, the decision was made to both verify and demonstrate that convergence could be accelerated by actively modifying the governing parameters affecting both stability and convergence. The donor-cell and over-relaxation parameters as well as the temporal increment were reduced to 0.9, 1.35, and 0.0001 seconds respectively. The corresponding step change in the incremental value of the domain kinetic energy depicted in Figure 17 resulted.

IV.2.2 Numerical Solution : Results

The results of both numerical simulations of the high temperature, low molecular weight exhaust gases injected into and interacting with the high-subsonic ambient crossflow satisfied all espoused research objectives, namely, the methodology not only provided the means to determine the trajectory of the exhaust plume, but, also to determine the location and extent of any recirculation region as well as any region with possibly large rates of heat transfer. The coarse simulation verified the mathematical model and the numerical algorithm; the refined mesh simulation provided the enhanced data which form the basis of the results presented herein. A welcome, but totally unanticipated result of both simulations, was the mathematical verification of a flow interaction phenomenon which was experimentally observed and also equally unanticipated. Thus the simplified methodology provided a mathematical tool of sufficient accuracy which was capable of duplicating physical phenomena and thereby provided the means to study the nature of violent injection problems.

Trajectory Analysis

As the low density jet impacted the ambient crossflow, only moderate penetration was achieved, namely the jet centerline remained within one D of the injection plane for the range of interest of distances aft of the jet orifice. Consequently, the mixing processes associated with the jet-crossflow interaction are confined to a region within close proximity to the injection surface. To understand the physical nature of these processes, contour plots of the gas mixture density, temperature, exhaust gas species mass fraction, and molecular weight were utilized. From these isopleth presentations, trajectory data were easily obtained from which comparisons to existing empirical formulae were made.

Figure 18 is a density contour map of the symmetry plane from which it is observed that as the jet enters the crossflow, the crossflow impacts the windward side of the jet and is compressed ahead of the jet orifice by the "quasi-solid" appearance of the jet to the crossflow. Because of this flow stagnation, low density gas is permitted to diffuse upstream of the jet within the boundary layer which is evidenced by the contours forming a "lip-like" region ahead of the jet orifice. Also from the figure, it is apparent that the low density gas mixture is contained within a stream tube, the upper surface of which is less than $0.5 D$ from the injection plane.

Similar results are observed in Figure 19 in which contours of constant temperature in degrees Kelvin are depicted. High temperature (low density) gases are constrained to a central stream tube and the jet plume cools rapidly to essentially freestream values in approximately $2.0 D$ on the windward side. Between the stream tube and the injection

surface, a region of high temperature gas exists which is characterized by large temperature gradients. Ahead of the jet, isotherms corresponding to the density contours of the previous figure show large streamwise gradients which are characteristic of a compression zone. Thermal diffusion in the boundary layer occurs ahead of the jet because of the essentially stagnated flow within this region. Both Figures 18 and 19 show that the region immediately aft of the jet is a region of high temperature, low density gas. It is revealing to note that regions in the isotherm presentation on the windward side of the jet centerline exist at temperatures greater than that associated with the gaseous injectant. The local high temperature zones are caused by conversion of kinetic to thermal energy within the mixing region. Finally, there appear to be at least three regions of possibly large rates of heat transfer to the injection plane, namely, the large gradient regions ahead and aft of the jet orifice as well as a large region aft of the orifice which extends approximately $4 D$ in the streamwise direction.

Because the exhaust species are corrosive by virtue of the fact that the mixture contains halogen compounds, it was imperative to ascertain the trajectory of the jet as well as the composition of the near field gases within the high temperature gradient regions. Figure 20 shows that the high temperature gradient region within the jet wake is composed predominately of air. In a distance of only $0.25 D$ aft of the jet orifice, the 0.05 mass fraction contour for the exhaust gas shows increased separation from the surface as the streamwise distance is increased. Ahead of the jet, the species mass fraction contours replicate the upstream diffusion evidenced in both Figures 18 and 19.

However, unlike the data displayed in these figures, Figure 20 shows that the gaseous injectant is confined to a region even closer to the injection surface than indicated by the density and temperature isopleths. This behavior is indicative of the fact that molecular diffusion although affecting the jet-crossflow interaction does not play a role which is as significant as either the thermal diffusion or convective processes. Also apparent from this figure is the recirculation region comprised of a mixture of exhaust gas and entrained air on the leeward side of the jet (wake region), the maximum exhaust gas mass fraction of which is approximately 0.35.

Figure 21 depicts contour data for the molecular weight of the gas mixture. It is obvious that the low density (low molecular weight) exhaust gas is indeed constrained to a small diameter stream tube which undergoes rapid cooling. The high temperature region aft of the jet and along the injection surface is comprised of heavy molecular weight gas (air) in which large gradients of molecular weight, in addition to those of temperature, exist. Thus, it is apparent that molecular diffusion occurs to a greater extent within the wake recirculatory region than it does on the windward side of the exhaust plume where convection is dominant. Consequently, the nature of the low Q (0.15) injection is predominately controlled by convective processes with minimal contributory effects from molecular diffusion upon the trajectory of the exhaust gas jet plume.

The jet trajectories determined from the density, temperature, gas species mass fraction, and molecular weight coincide as indicated in Figure 22. In fact, the composite trajectory curve appeared to vary in

accordance with experimental observations and experimentally derived empirical expressions, that is, Z/D is proportional to X/D raised to the one-third power; similarly, the slope varies with X/D raised to the negative two-thirds power. Figure 23 depicts isopleths of constant Mach number for the symmetry plane. These contours show the same slope as the superimposed trajectory curve determined from Figures 18 through 21. It is interesting to note that the jet centerline curve closely approximated the Mach 0.24 contour, a value which is identical to that of the jet injection Mach number.

Flowfield Analysis

In addition to the determination of the jet plume trajectory and the regions of possibly high heat transfer rates from the analyses of the contour data presented in Figures 18 through 23, further information was obtained from analyses of the flowfield itself and its inherent properties. Figure 24a depicts the velocity field of the symmetry plane of the jet from which the extent of the wake recirculation zone is easily obtained. This region which extends from the aft portion of the jet orifice to a position $1.25 D$ further aft along the injection surface does not extend normally beyond $D/4$ from the injection surface. Consequently, coupled with the large temperature gradient prevalent in this region, the recirculation zone further augments the heat transfer from the gas to the surface. At the position $3.2 D$ from the center of the jet, a wall vortex (recirculation zone) formed and extended to a point on the surface $4.5 D$ from the jet center. As observed from Figures 24b through 24c which are adjacent y-planar cuts of the computational domain situated one and two cells respectively from the

symmetry plane (Figure 24a), the lateral span of the secondary recirculation zone does not exceed 0.3 D. From the knowledge of fluid dynamic flows of single species perfect gases, a recirculation zone only occurs in the presence of an adverse pressure gradient. To verify that the mathematically predicted wall vortex was not the result of spurious computations due to error uncertainties of the algorithm, the pressure, temperature, molecular weight, and ratio of specific heats in the symmetry plane along the surface of the injection plane were plotted in Figure 25. As evidenced by this figure, the pressure increased upstream of the jet and subsequently fell rapidly aft of the jet orifice from which point the flowfield attempted to recover from the pressure defect. Approximately 2.2 D aft of the jet center, an adverse pressure gradient formed thereby providing the necessary requirement for the development of any recirculation zone. The temperature along the adiabatic wall increased impulsively from the freestream value ahead of the jet orifice to a local maximum at the jet exit. The temperature then dropped rapidly to 50 degrees Kelvin above ambient at a point 2.2 D from the jet center which coincided with the streamwise location of the adverse pressure gradient. However, temperatures greater than the melting temperature of aluminum alloy (923 °K) employed in aircraft construction persisted 0.2 D aft of the diffuser exit. The molecular weight variation exhibited the same behavior with the jet-crossflow mixing aft of the jet along the injection surface being essentially completed within 1.4 D of the jet center after which the gas mixture tended to recover to ambient values. The specific heat ratio variation mirrored the molecular weight variation and recovered to a value representative of pure air by 1.4 D aft of the jet center.

The presence of this wall vortex which had been observed to a smaller scale in the less accurate coarse grid simulation was totally unanticipated. A similar occurrence had been observed by Zakanycz (Ref 50) in experimental binary gas mixing research for a coflowing helium jet injected into air. The presence of the experimentally occurring wall vortex was observed only after numerical correlation data for the measured turbulence intensities exhibited severe discrepancies. As will be shown in subsequent hot air and helium injectant simulations, this phenomenon appears to occur only when gases of two vastly different molecular weights are mixed. Recurrence of this wall vortex formation was observed for the hot helium jet but not for the hot air jet. Whether a similar phenomenon occurs for a more heavy molecular weight gas injected into a lighter molecular weight gas is pure conjecture at this time as is the range of molecular weights for which this phenomenon is a function. However, the presence of this wall vortex embedded between the wall and the high temperature, large gradient region in the jet wake could add an appreciable increment to the heat transfer in this region computed in any simplified analysis which did not account for its presence. If the aft portion of the injection surface was modified to simulate the curvature of the fuselage of the wide-bodied air vehicle, it is doubtful that the wall vortex would disappear because increased curvature introduces additional buoyancy effects into the flowfield thereby almost positively assuring that some vortex region would exist despite the pressure relief afforded by the increased curvature.

Figure 26 presents pressure coefficient data for the symmetry plane. From observation of the data, there exist two main pressure

centers. In the compression zone ahead of the jet, a large positive pressure cell exists approximately $D/2$ ahead of the jet and $D/2$ down from the injection surface. A smaller negative pressure cell exists in the wake region at the aft edge of the jet orifice ($D/2$) and apparently centered on or very close to the injection surface itself. This low pressure region entrains high temperature waste gases thereby creating the high heat transfer which was identified earlier from trajectory contour data.

IV.3 Simplified Analyses

Because of the exorbitant amount of computational resources required to solve the three-dimensional Navier-Stokes for real gas mixtures with varying transport and thermodynamic properties, two additional simulations were made to determine whether simplified analyses could be utilized to obtain useful engineering data which would, in fact, replicate the data obtained from more costly gas mixture analyses. These simplified analyses included a hot helium jet and a hot air jet constrained by an injection temperature of 1500 °K, an injection Mach number of 0.24, and an injection to freestream dynamic pressure ratio of 0.15. Additionally, it was further anticipated that the perfect gas simulation for hot air injected into the cold ambient crossflow would provide some means of correlating real gas mixture injection with that of the more simply modeled hot air injection.

IV.3.1 Helium Jet

The simulation of an aspect ratio 1.75 rectangular jet of pure helium at a temperature of 1500 °K being injected into a Mach 0.7

crossflow at an aircraft pressure altitude of 11 kilometers was accomplished by dividing the computational domain into $29 \times 13 \times 13$ cells in the x , y , and z spatial coordinate directions respectively such that the CDC Cyber 175 at Wright-Patterson AFB was capable of handling the resultant core requirements. A K value of 1.20 was employed to expand the geometrically varying z -dimension of each cell from the injection surface. The jet orifice was modeled by 4×3 cells in the x and y directions in the injection plane respectively. The numerical solution was terminated after an acceptable level of convergence had been obtained as is evidenced by Figure 27. The typical approach to steady-state was observed and computations were terminated after $t=0.34$ seconds which corresponds to approximately 2.5 characteristic times.

The flowfield data of the symmetry plane are presented in Figure 28. The recirculation zone in the wake region appears to be more extensive than that predicted by the simulation utilizing the more refined mesh. A minute indication of the wall, or secondary, vortex along the injection plane at approximately $4.0 D$ from the jet center is also indicated. However, the coarse grid simulation for helium fails to define the extent of this recirculation zone.

The density isopleths in Figure 29 depict the compression zone ahead of the jet orifice as well as the region characterized by high temperatures and large temperature and molecular weight gradients in the wake near the injection surface. The jet trajectory obtained from this figure is plotted in Figure 22. It is evident that the hot helium injectant trajectory curve replicates the Z/D variation with X/D to the one-third power; however, the error induced by the coarse mesh helium

simulation resulted in the trajectory being situated above the corresponding curve derived from the refined mesh gas mixture simulation. As the X/D value increased, the agreement between these two curves increased.

IV.3.2 Hot Air Jet

The simulation of an aspect ratio 1.75 rectangular air jet at 1500 °K being injected into an ambient crossflow at 0.7 Mach number at an aircraft pressure altitude of 11 kilometers was similarly accomplished by dividing the computational domain into $29 \times 13 \times 17$ cells in the x, y, and z spatial coordinate directions respectively such that the simulation could be conducted on the CDC Cyber 175 at Wright-Patterson AFB. A K factor of 1.20 was also used to expand the z-dimension cell length for every cell measured from the injection surface. Additionally, the jet orifice was modeled by 4×3 cells in the x and y directions respectively embedded in the injection surface. The numerical solution was terminated after $t=0.24$ seconds despite the fact that the solution had exhibited an acceptable level of convergence long before (Figure 30) and no numerical instability appeared probable. The termination time in this case was still less than two characteristic times.

As is evidenced by the flowfield data of the symmetry plane in Figure 31, only the recirculation zone within the wake was discerned from the numerical simulation. As alluded to in Section IV.2.2, the appearance of the wall vortex did not recur which reinforced by the behavior of the flowfield tends to confirm the hypothesis of the vortex being driven by a species diffusive flux caused by gradients in

molecular weight or species concentrations in the presence of a "no-slip" surface.

The density contour plot in Figure 32 depicts a similar compression zone ahead of the jet orifice and the high temperature, large gradient layer in the wake and adjacent to the injection surface. The trajectory curve obtained from this figure was also plotted in Figure 22. However in this case, the trajectory lies below that of the refined grid gas mixture simulation. It too demonstrates the same general behavior as the other trajectories, namely, the penetration depth, Z/D , variation with X/D to the one-third power. Golubev and Klimkin (Ref 51) have shown that for jets with equal initial momenta, "the rate at which the apparent additional mass increases is higher in jets with low density than in jets with high density." Consequently, the lower trajectory for the hot air is thus easily explained by the constraint of constant Q (0.15) which is the ratio of jet to freestream momentum fluxes while also subject to the additional constraint of equal jet injection temperatures. The density of air which is greater than that of helium requires that velocity squared term of air be less than the corresponding term for helium to maintain the constancy of the density-velocity squared product (Q). The resulting exit velocity of the air jet (176 m/sec) was therefore approximately one-third that of the helium jet (547 m/sec) at the diffuser exit for a jet exit Mach number equal to 0.24. Because of the decreased injection velocity, less penetration of the crossflow was achieved. Further attenuation of the jet penetration was caused by the entrainment of the ambient crossflow.

IV.4 Molecular Weight Correction

During the course of the research, it was observed that the jet-crossflow interactions of both low and high molecular weight gas injectants with the ambient crossflow exhibited essentially the same convection dominated behavior and contained essentially the same physical phenomena. The main difference, excluding obvious concentration induced effects, was the degree to which these characteristics were observed. Because of the large differences in molecular weights of the injected gases, it was necessary to employ some correction factor to account for this variation if the trajectories were to collapse into a single curve.

In typical heat and mass transfer problems involving gas injectants not of the same species as that of the dominant gas medium, the ratio of the mass transfer conductance to the corresponding value with "no blowing" is corrected by the following factor which is dependent upon the flow characteristics (Ref 10, pages 322 and 326):

$$G = \left(\frac{\text{freestream molecular weight}}{\text{considered phase surface molecular weight}} \right)^s \quad (100)$$

where s is either $2/3$ or 0.4 for laminar and turbulent flow, respectively. Though no logical relation exists to extend Eq (100) for use at high blowing rates, its use as an empirical correction factor fortuitiously does account for molecular weight variations. In the present research of turbulent rectangular jet injection, the value of the exponent s in Eq (100) was assumed to be 0.4 and the molecular weight of the considered phase was assumed to be identical to that of

the injectant. The results of applying this factor to both simulation and empirically derived jet trajectories are depicted in Figure 22. The correction factor modification clearly demonstrated the proper behavior; with additional analyses and experimentation, enhanced results may be obtained by more accurately describing the exponent. Of all the trajectory expressions analyzed during this research, only that of Callaghan and Ruggeri, Eq (8), shows some promise of being used in conjunction with the molecular weight correction, G , given by Eq (100) for interacting gases with different molecular weights at elevated temperatures to predict the jet plume centerline. In fact, when applied to the conditions imposed on the injected gas mixture and crossflow and utilizing either the streamwise dimension, D , or the equivalent diameter, D_e , of the jet orifice in the expression, the resultant curve varied less than 10 and 5 per cent respectively from that derived from the refined mesh numerical simulation.

IV.5 Turbulence Diffusivity: Heat Transfer Effects

Additional numerical simulations were conducted to ascertain the effects of turbulence diffusivity upon the heat transfer to the injection surface (aircraft fuselage). These effects were essentially bracketed by simulations made with both molecular and turbulent values of the diffusivities for air and helium gaseous injectants at 1500 °K further constrained to the same Q ratio, Mach numbers associated with the jet and freestream, and operating altitude of the previous studies. These sensitivity analyses were accomplished on the CDC Cyber 750 (replacement for the CDC Cyber 175) at Wright-Patterson AFB, Ohio, utilizing the identical coarse meshes described earlier. The "no-slip"

injection surface was defined to be adiabatic, that is, no heat transfer to the surface from the gas was permitted; however, the adiabatic wall temperature does provide an accurate indication of the heat transfer to the surface as it has been sufficiently demonstrated in the literature pertaining to film cooling. In each of the ensuing simulations, the turbulence model utilized was that given by Eq (34). The minimal diffusivity runs employed the effective viscosity in concert with just the molecular (laminar) values of thermal conductivity and mass transfer binary diffusion coefficient (helium runs, only). The turbulent diffusivity runs incorporated the effective values of viscosity, thermal conductivity, and binary diffusion coefficient.

The adiabatic wall temperatures for air with minimal and turbulent diffusivities are presented in contour map form in Figures 33 and 34 respectively from which the nature of the heat transfer to the surface can be directly inferred. When just the molecular value of thermal conductivity was used (Figure 33) only a near field thermal diffusive effect exists such that the wall temperature recovers to essentially freestream values within $D/4$ of the diffuser exit. However, when the full turbulent diffusivities were employed (Figure 34), the thermal diffusion was significantly enhanced. High temperature (>550 °K) regions exist approximately $D/4$ upstream of the diffuser exit, $D/2$ laterally from the diffuser exit, and $3D$ aft of the diffuser exit along the center line. This drastically large region of elevated wall temperature poses severe thermal protection problems which must be solved.

The corresponding adiabatic wall temperature presentations for

helium with both minimal and fully turbulent diffusivities are presented in Figures 35 and 36, respectively. The solution for the minimal diffusivity run was still developing when the simulation was terminated. However, the extent of the high temperature region is far greater than the associated region for air (Figure 33). When the full set of diffusivities was employed as evidenced in Figure 36, the increased thermal diffusion is even more drastic than that produced by the turbulent diffusivity run for air. Not only does the high temperature region encompass more of the injection surface, but also, it is evident that an exceptionally large region exists in which the local temperature (adiabatic wall) is in excess of the melting temperature of aluminum alloys employed in aircraft construction. This melting region is contained approximately within the subregion $D/4$ upstream of the diffuser exit, $D/2$ laterally from the diffuser exit, and $2.5 D$ aft of the diffuser exit. As is evidenced by Figure 36, surrounding this melting region a far larger region exists in which the aluminum alloys would lose significant percentages of the available structural strength and consequently would lead to structural deformation. Because the AFWL gas mixtures are comprised of approximately 86 per cent helium, the temperature distribution on the injection surface (fuselage) and the associated heat transfer to it should virtually replicate the corresponding behavior and characteristics associated with the pure helium jet injection.

Based upon these diffusivity sensitivity studies, the heat transfer mechanism to the injection surface can be divided into two coupled facets. First, because of the enhanced diffusivities provided by the

turbulent transport, significant thermal diffusion occurs between the jet plume and the injection surface. However, with an increase in turbulent diffusivity, the second facet of the heat transfer mechanism comes into play. The high turbulent diffusivities associated with the jet plume cause the plume to both expand and cool thereby directly reducing the source of energy for heat transfer to the injection surface. Consequently, the wall temperature then decreases to somewhat lower levels because of both the enhanced turbulent diffusive efficiency and the reduction of available energy within the jet plume.

IV.6 Summary

The hot (1500 °K) exhaust gases from an airborne chemical laser being ejected downwards from an aspect ratio 1.75 rectangular jet orifice aligned with the major axis parallel to the streamwise Mach 0.7 ambient crossflow was successfully simulated. The data acquired from the numerical simulation described the jet plume trajectory, the extent of the recirculation zone in the wake of the jet-crossflow interaction, and the regions of high possible rates of heat transfer. Additionally, the numerical method demonstrated the existence of a secondary wall vortex (recirculation zone) which formed after the jet plume was sufficiently deflected to be essentially aligned with the ambient crossflow (coflowing). The formation of a wall vortex was experimentally observed by Zakanycz (Ref 50) in his experimental investigation of binary gas mixing. Nowhere else in the available literature has this phenomenon been mentioned which apparently only occurs for low molecular weight gases interacting with a higher molecular weight coflowing gaseous medium (air, for example) in the presence of a constraining "no-slip" surface.

Simplified analyses were also conducted to determine if the essential flow phenomena were captured mathematically utilizing a simple binary gas interaction, that is, hot helium injected into crossflowing ambient air, or even more simply, just utilizing a hot air jet being injected into the ambient crossflow. The essential flow features of the exhaust gas mixture simulation were replicated by the helium jet simulation to some extent; however, the accuracy of the coarse grid simulation was not to the same level of accuracy provided by the refined mesh gas mixture simulation. Additionally, the wall vortex formation which did become apparent in the helium injectant simulation failed to recur for the hot air jet-crossflow interaction problem thereby adding credence to the hypothesis that diffusive fluxes induced the formation of this secondary wall vortex.

Not only were useful engineering data obtained from the simplified numerical algorithm, but, also the utility of the methodology as a learning and prognostic tool to study the effects of violent jet-crossflow interactions was demonstrated. The flowfields for both real gases and hot air showed essentially the same basic structure and characteristics because of the dominance of the convective processes. However, the effects of species concentration gradients which apparently induced a secondary recirculation zone to form could not be duplicated by utilizing only one gas in the jet-crossflow interaction problem. Sufficient evidence was obtained to warrant the simplification of a gas mixture injection problem by replacing the mixture with a representative gas such that an effective binary gas mixture in the flowfield would result with the attendant savings in computational resources; if

chemical reactions were permitted to occur within the simulation, this simplification could not obviously be made. The coarse grid utilized in the simplified analyses resulted in numerical errors which were unacceptable for quantitative descriptions of the observed flow phenomena but which were acceptable for qualitative investigations. For results of engineering utility, a finer subdivision of the computational domain is required and a geometric stretch factor, K , not exceeding 1.09 should be used because of the inherent inaccuracy of the numerical algorithm when a non-uniform mesh is employed.

The application of a molecular weight correction factor given by Eq (100) to the simplified analyses demonstrated that trajectory curves could be synthesized from one another for identical jet and crossflow constraints. Use of this factor in conjunction with the empirical trajectory expression of Callaghan and Ruggeri resulted in less than 5 per cent deviation from the trajectory derived from the refined mesh numerical simulation of the gas mixture (Table I) injectant.

Finally, the effects of the turbulent diffusivities upon the heat transfer to the injection surface were determined for both air and helium gas injection problems. Increased levels of heat transfer to the surface resulted when increased levels of diffusivities were utilized (as indicated by the adiabatic wall temperatures). Regions of severe heating were found to exist for both high temperature air and helium injections at low values of Q . The heating was especially pronounced for the helium case where large surface regions were discerned to exist in which the injection surface adiabatic wall temperatures exceeded both the temperature associated with structural deformation and the melting temperature of aluminum alloys employed in aircraft construction.

V. Conclusions and Recommendations

The high temperature exhaust gases from an airborne chemical laser ejected normally downward from an aspect ratio 1.75 rectangular diffuser orifice mounted in the lower surface of the fuselage of a wide-bodied aircraft into the Mach 0.7 ambient crossflow at an aircraft pressure altitude of 11 kilometers was successfully numerically simulated. A simplified finite difference donor-cell ICE algorithm (Ref 44) was modified to solve the complete set of time dependent, compressible, three-dimensional Navier-Stokes equations in addition to a species conservation equation while employing variable thermodynamic and transport properties. Turbulence closure was achieved through the use of a locally varying velocity defect eddy viscosity model. In the mathematical model of the physical problem, the gas injectant was proscribed from reacting with the ambient crossflow. (C-1) The numerical methodology exhibited the capability to solve violent gaseous injection problems such as the normally ejected jet interacting with an ambient crossflow at both high, and more importantly, low ratios of jet to crossflow momentum flux (16.0 and 0.15).

Constrained by the same injection Mach number, Q value, and temperature, (C-2) the basic structure and characteristics of the jet-crossflow interaction with the Mach 0.7 crossflow at a simulated pressure altitude of 11 kilometers (tropopause) were essentially the same regardless of the jet injection species. (C-3) Convective processes were seen to dominate the jet-crossflow interaction even when helium was the injectant. (C-4) Thermal diffusion was seen to have a significantly greater effect on the resultant gas mixture-air flowfield than molecular diffusion.

The (C-5) penetration of the impacting crossflow by the fully turbulent gas injectants when the Q value was constrained to 0.15 was inversely proportional to the densities of the injectants. Thus, a helium jet penetrated the crossflow farther than the gas mixture (molecular weight 6.6) which in turn penetrated farther than the corresponding air jet. Because the value of Q was constant, the velocity-density squared product of the jet species prior to injection was also fixed thereby requiring the velocity squared term to vary accordingly to satisfy the imposed constraints (Q and M_j). Consequently, the greater velocity (momentum) defect of the heavier molecular weight injectants resulted in proportionately less crossflow penetration. Additionally, (C-6) when the gas mixture injectant which was assumed to be unreactive with the ambient crossflow was replaced by a single representative gas (for example, helium) to reduce the computational complexity, the algorithm produced results which were in agreement with those generated by employing the gas mixture.

As is evidenced by Figure 22, (C-7) utilization of the molecular weight correction factor described in Section IV.4 enabled the trajectory curve of one species to approximately generate the corresponding trajectory of another. (C-8) The empirical relationship derived by Callaghan and Ruggeri, Eq (8), was employed in conjunction with the molecular weight correction factor, Eq (100), to predict the trajectory of the real gas mixture jet being ejected into the ambient crossflow. Excellent agreement was obtained between the refined mesh numerical simulation and the empirically derived trajectories.

Sensitivity studies conducted to determine the effects of the

magnitude of turbulent diffusivities on the heat transfer to the injection surface demonstrated that (C-9) large regions exist on the injection surface in which temperatures exceed the maximum safe temperature of aluminum alloys associated with the onset of permanent structural deformation. Severe heating regions within this zone have temperature levels in excess of the melting temperature of aircraft aluminum alloys. Furthermore, it was observed that (C-10) the heat transfer mechanism from the jet plume to the injection surface was comprised of two coupled phenomena which lead to significant levels of injection surface heating. As the turbulent diffusivities were increased, the heat transfer to the surface increased until a local maximum was obtained, after which, additional increases in diffusivity resulted in lower heat transfer rates to the injection surface by the mechanism described in Section IV.5.

The following recommendations for further study are submitted to provide further refinement to (1) the numerical methodology with the attendant increases in run time per cycle and fiscal charges, and, to (2) the mixing mechanisms involved in high temperature, low molecular weight jet injection into crossflowing gaseous mediums of the same or of a different species:

(R-1) Diffusion - add both the DuFour ("diffusion-thermo") and the Soret ("thermal-diffusion") effects to the numerical algorithm. Because the temperature of the jet and the associated interacting flow is extremely high with correspondingly large temperature gradients, the inclusion of

these "secondary" effects may have a pronounced effect on the computational results.

(R-2) Coordinates - employ a generalized body oriented coordinate (geometry) subroutine replete with the requisite metrics to permit calculations from arbitrarily defined bodies.

(R-3) Species Generation - permit the exhausting gas to chemically react with the ambient crossflow within the wake region of the jet-crossflow interaction.

(R-4) State - modify the solution algorithm to account for gradients in concentration (mass fraction and molecular weight) as well as temperature. The existing algorithm accounts for small variations in pressure in the ICE iteration while essentially neglecting the variations of temperature and concentration. Incorporation of the additional terms in the code would definitely increase its robustness.

(R-5) Radiation - incorporate the effects of radiative heat transfer from the high temperature boundary layer in the wake of the jet.

(R-6) Surface Heat Transfer - remove the constraint of an adiabatic wall to permit calculation of the effects of various gaseous injectants on the heat transfer to the air vehicle surface.

(R-7) Self-Optimization - employ a subroutine in the algorithm to automatically compute and update the donor-cell parameter, over relaxation factor, and temporal increment

during each time step to reduce the computational time required to obtain the asymptotic approach to steady-state of the numerical solution.

(R-8) Molecular Weight - conduct experimental jet-crossflow binary gas studies to obtain quantitative data relating the trajectory of the jet plume with the associated molecular weights of the interacting species.

(R-9) Accuracy - employ a higher order algorithm in conjunction with a substantially refined mesh in the near field region of the jet. This recommendation would require the availability of a computer with vastly greater core capacity than that of the CDC 7600.

Bibliography

1. Abromovich, G. N. The Theory of Turbulent Jets, MIT Press, Cambridge, Mass., 1963.
2. Chan, Tzeng-Long and Kennedy, John F. "Turbulent Nonbuoyant or Buoyant Jets Discharged into Flowing or Quiescent Fluids," Iowa Institute of Hydraulic Research Report No. 140, August, 1972. (Available through DDC as AD-760028)
3. Pratte, Bruce D. and Baines, W. Douglas. "Profiles of the Round Turbulent Jet in a Cross Flow," Journal of the Hydraulics Division, Proceedings of the American Society of Civil Engineers, November, 1967, pages 54-64.
4. Vizel, Y. M., and Mostinskii, I. L. "Deflection of a Jet Injected into a Stream," Inzhenerno-Fizicheskii Zhurnal, Vol 8, No. 2, 1965, pages 238-242, (Journal of Engineering Physics, Vol 8, No 2, February, 1965, pages 160-163)
5. Epshtein, A. M. "Shape of Turbulent Jet Axis in an Unbounded Horizontal Cross Flow," Journal of Engineering Physics, Vol 9, No. 4, October, 1965, pages 303-306.
6. Vaklamov, S. V. "Computation of the Trajectory of a Jet in a Drifting Flow," Inzhenerno-Fizicheskii Zhurnal, Vol 7, No. 10, 1964, pages 112-116. (English translation in FTD-TT-65-1977, Available through DDC as AD-639159)
7. Shandarov, G. S. "Calculation of a Jet Axis in a Drifting Flow," NASA TT-F-10,638, December, 1966. (Translation of "Raschet osi strui v snosyashchem potke," Izvestiya Vysshikh Uchebnykh Zavedeniy, Aviatsionnaya Tekhnika, Vol 9, No. 2, 1966, pages 100-104)
8. Callaghan, E. E. and Ruggeri, R. S. "Investigation of the Penetration of an Air Jet Directed Perpendicularly to an Air Stream," NACA TN-1615, 1948.
9. Margason, R. J. "The Path of a Jet Directed at Large Angles to a Subsonic Free Stream," NASA TN D-4919, November, 1968.

10. Kays, W. M. Convective Heat and Mass Transfer, McGraw Hill Book Company, 1966.
11. Callaghan, E. E. and Bowden, D. T. "Investigation of Flow Coefficients of Circular, Square, and Elliptical Orifices at High Pressure Ratios," NACA TN-1947, September, 1949.
12. Ruggeri, R. S., Callaghan, E. E., and Bowden, D. T. "Penetration of Air Jets Issuing from Circular, Square, and Elliptical Orifices Directed Perpendicularly to an Airstream," NACA TN-2019, February, 1950.
13. Ruggeri, R. S. "General Correlation of Temperature Profiles Downstream of a Heated Air Jet Directed at Various Angles to Air Stream," NACA TN-2855, December, 1952.
14. Jordinson, R. "Flow in a Jet Directed Normal to the Wind," ARC Technical Report R&M No. 3074, 1958.
15. Gelb, G. H. and Martin, W. A. "An Experimental Investigation of the Flow Field About a Subsonic Jet Exhausting into a Quiescent and a Low Velocity Air Stream," Canadian Aeronautics and Space Journal, October, 1966, pages 333-342.
16. Keffer, J. F. and Baines, W. D. "The round turbulent jet in a cross-wind," Journal of Fluid Mechanics, Vol 15, Part 4, 1963, pages 481-496.
17. Slawson, P. R. and Csanady, G. T. "On the mean path of buoyant bent-over chimney plumes," Journal of Fluid Mechanics, Vol 28, Part 2, 1967, pages 311-322.
18. Pratte, B. D. and Baines, W. D. "Profiles of the Round Turbulent Jet in a Cross Flow," Journal of the Hydraulics Division, Proceedings of the American Society of Civil Engineers, HY 6, Vol 93, November, 1967, pages 53-64; Corrected in Journal of the Hydraulics Division, ASCE Proceedings, HY 3, Vol 94, May, 1968, pages 815-816.
19. Lee, C. C. "A Review of Research on the Interaction of a Jet with an External Stream," Technical Note R-184, Brown Engineering Company, Huntsville, Alabama, March, 1966. (Available through DDC as AD-630294)

20. Garner, J. E. "A Review of Jet Efflux Studies Applicable to V/STOL Aircraft," AEDC TR-67-163, September, 1967. (Available through DDC as AD-658432)
21. Kamotani, Y. and Greber, I. "Experiments on a Turbulent Jet in a Cross Flow," AIAA Journal, Vol 10, No. 11, November, 1972.
22. Sforza, P. M., Steiger, M. H., and Trentacoste, N. "Studies of Three-Dimensional Viscous Jets," AIAA Journal, Vol 14, No. 5, May, 1966, pages 800-806.
23. Trentacoste, N. and Sforza, P. "Further Experimental Results for Three-Dimensional Free-Jets," AIAA Journal, Vol 5, No. 5, May, 1967, pages 885-890.
24. Sforza, P. "A Quasi-Axisymmetric Approximation for Turbulent, Three-Dimensional Jets and Wakes," AIAA Journal, Vol 7, No. 7, July, 1969, pages 1380-1383.
25. du Plessis, M. P., Wang, R. L., and Kahawita, R. "Investigation of the Near-Region of a Square Jet," Transactions of the ASME, Journal of Fluids Engineering, September, 1974, pages 246-251.
26. Weston, R. P. and Thames, F. C. "Properties of Aspect-Ratio 4.0 Rectangular Jets in a Subsonic Crossflow," Journal of Aircraft, Vol 16, No. 10, October, 1979, pages 701-707.
27. Chang, Hsin-Chen, et al. "The Roll-up of a Cylindrical Jet in a Cross Flow," ARL 73-0131, December, 1973. (Translation of Ph. D. dissertation of Chang completed in 1942; available through DDC as AD-769477)
28. Braffury, L. J. S., and Wood, M. N. "The Static Pressure Distribution Around a Circular Jet Exhausting Normally from a Plane Wall into an Airstream," ARC CP No. 822, 1965.
29. Wooler, P. T. "On the Flow Past a Circular Jet Exhausting at Right Angles from a Flat Plate or Wing," Journal of the Royal Aeronautical Society, Vol 71, March, 1967, pages 216-218.
30. Williams, J. and Wood, M. N. "Aerodynamic Interference Effects with Jet-Lift V/STOL Aircraft Under Static and Forward Speed Conditions," Zeitschrift fur Flugwissenschaften, July, 1967, pages 237-256.

31. Wooler, P. T., Burghart, G. H., and Gallagher, J. T. "Pressure Distribution on a Rectangular Wing with a Jet Exhausting Normally into an Airstream," *Journal of Aircraft*, Vol 4, No. 6, November-December, 1967, pages 537-543.
32. Wu, J. C., Mosher, D. K., and Wright, M. A. "Experimental and Analytical Investigations of Jets Exhausting into a Deflecting Stream," *AIAA Paper No. 69-223*.
33. Braun, G.W. and McAllister, J. D. "Crosswind Effects on Trajectory and Cross Sections of Turbulent Jets," *Analysis of a Jet in a Subsonic Crosswind*, NASA SP-218, 1969, pages 141-164.
34. Rubbert, P. E. "Calculation of Jet Interference Effects on V/STOL Aircraft by a Nonplanar Potential Flow Method," *Analysis of a Jet in a Subsonic Crosswind*, NASA SP-218, 1967, pages 181-204.
35. Endo, H. and Nakamura, M. "Bending and Development of Three-Dimensional Turbulent Jets in a Crosswind," *FTD-HC-23-1486-71*, August, 1972. (Available through DDC as AD-751-093)
36. Schatzmann, M. "The Integral Equations for Round Buoyant Jets in Stratified Flows," *Zeitschrift fur angewandte Mathematik und Physik*, Vol 29, 1978, pages 608-630.
37. Oh, Y. H. and Harris, J. E. "Numerical Solution of Three-Dimensional Free Turbulent Shear Flows," *Symposium on Turbulent Shear Flows*, University Park, Pa, April 18-20, 1977, pages 1.17-1.23. (Available through DDC as AD-A055654)
38. McGuirk, J. J. and Rodi, W. "The Calculation of Three-Dimensional Turbulent Free Jets," *Symposium on Turbulent Shear Flows*, University Park, Pa., April 18-20, 1977, pages 1.29-1.36 (Available through DDC as AD-A055654)
39. Chien, J. C. and Schetz, J. A. "Numerical Solution of the Three-Dimensional Navier-Stokes Equations with Applications to Channel Flows and Buoyant Jet in a Cross Flow," *Journal of Applied Mechanics*, Vol 42, 1975, pages 575-579.
40. Pantankar, S.V., Basu, D. K., and Alpay, S. A. "Prediction of the Three Dimensional Velocity Field of a Deflected Turbulent Jet," *Transactions of the ASME, Journal of Fluids Engineering*, December, 1977, pages 758-762.

41. Harsha, P. T. "Free Turbulent Mixing: A Critical Evaluation of Theory and Experiment," AEDC-TR-71-36, February, 1961. (Available through DDC as AD-718956)
42. Morkovin, Mark V. "Effects of Compressibility on Turbulent Flow," International Symposium on the "Mechanique de la Turbulence", Centre National de la Recherche Scientifique, Paris, France, 1962, pages 367-380.
43. Hirt, C. W., Nichols, B. D., and Romero, N. C. "SOLA - A Numerical Solution Algorithm for Transient Fluid Flows," Los Alamos Scientific Laboratory, LA-5852, April, 1975. (Available through DDC as AD-A009953)
44. Cloutman, L. D., Hirt, C. W., and Romero, N. C. "SOLA-ICE: A Numerical Solution Algorithm for Transient Compressible Fluid Flows," Los Alamos Scientific Laboratory, LA-6236, July, 1976.
45. Harlow, F. H. and Amsden, A. A. "A Numerical Fluid Dynamics Method for All Flow Speeds," Journal of Computational Physics, Vol 8, 1971, pages 197-213.
46. Rivard, W. C., Farmer, O. A., and Butler, T. D. "RICE: A Computer Program for Multicomponent Chemically Reactive Flows at All Speeds," Los Alamos Scientific Laboratory, LA-5812, March, 1975.
47. Peake, D. J. "The Pressures on a Surface Surrounding a Jet Issuing Normal to a Mainstream," National Research Council of Canada, Aeronautical Report LR-410, November, 1964. (Available through DDC as AD-463295)
48. Fearn, Richard L. and Weston, Robert P. "Induced Pressure Distribution of a Jet in a Crossflow," NASA TN D-7916, 1975.
49. Weston, Robert P. NASA Langley Research Center, Hampton, Virginia, 23665. Personal Communication.
50. Zakanycz, Stephen. "Turbulence and the Mixing of Binary Gases," Ph. D. Thesis, The Ohio State University, 1971.
51. Golubev, V. A. and Klimkin, V. F. "Investigation of Submerged Turbulent Gas Jets with Different Densities," Journal of Engineering Physics, Vol 34, No. 3, March 1978, pages 333-338.

- A.1 U. S. Standard Atmosphere, 1962, U.S. Government Printing Office, Washington, D.C., December, 1962.
- B.1 Hines, William W. and Montgomery, Douglas C. Probability and Statistics in Engineering and Management Science, The Ronald Press Company, New York, 1972.
- C.1 Hirschfelder, J. O., Curtiss, C. F., and Bird, R. B. Molecular Theory of Gases and Liquids, John Wiley and Sons, Inc., 1954. Reprinted with notes added 1964.
- C.2 Svehla, Roger A. "Estimated Viscosities and Thermal Conductivities of Gases at High Temperatures," NASA TR R-132, 1962.
- C.3 Liley, P. E. "Transport Properties of Selected Elements and Compounds in the Gaseous State," TPRC Report 20, Thermophysical Properties Research Center, Purdue University, November, 1962.
- C.4 Reid, Robert C. and Sherwood, Thomas K. The Properties of Gases and Liquids, McGraw-Hill Book Company, Second Edition, 1966.
- C.5 Reid, Robert C., Prausnitz, John M., and Sherwood, Thomas K. The Properties of Gases and Liquids, McGraw-Hill Book Company, Third Edition, 1977.
- C.6 Brokaw, Richard S. "Alignment Charts for Transport Properties Viscosity, Thermal Conductivity, and Diffusion Coefficients for Nonpolar Gases and Gas Mixtures at Low Density," NASA TR R-81, 1961.
- C.7 Brokaw, Richard S. "Viscosity of Gas Mixtures," NASA TN D-4496, April, 1968.
- C.8 Bird, R. Byron, Stewart, Warren E., and Lightfoot, Edwin N. Transport Phenomena, John Wiley and Sons, Inc, 1960.
- C.9 Mechtly, E. A. "The International System of Units, Physical Constants and Conversion Factors," NASA SP-7012, 1964.
- D.1 Stull, D. R. and Prophet, H. JANAF Thermochemical Tables, Second Edition, NSRDS-NB37, National Bureau of Standards, 1971, updated.

D.2 Keenan, Joseph H. and Kaye, Joseph. Gas Tables, John Wiley and Sons, Inc., 1948.

D.3 Eckert, E. R. G. and Drake, Robert M., Jr. Analysis of Heat and Mass Transfer, McGraw-Hill Book Company, 1972.

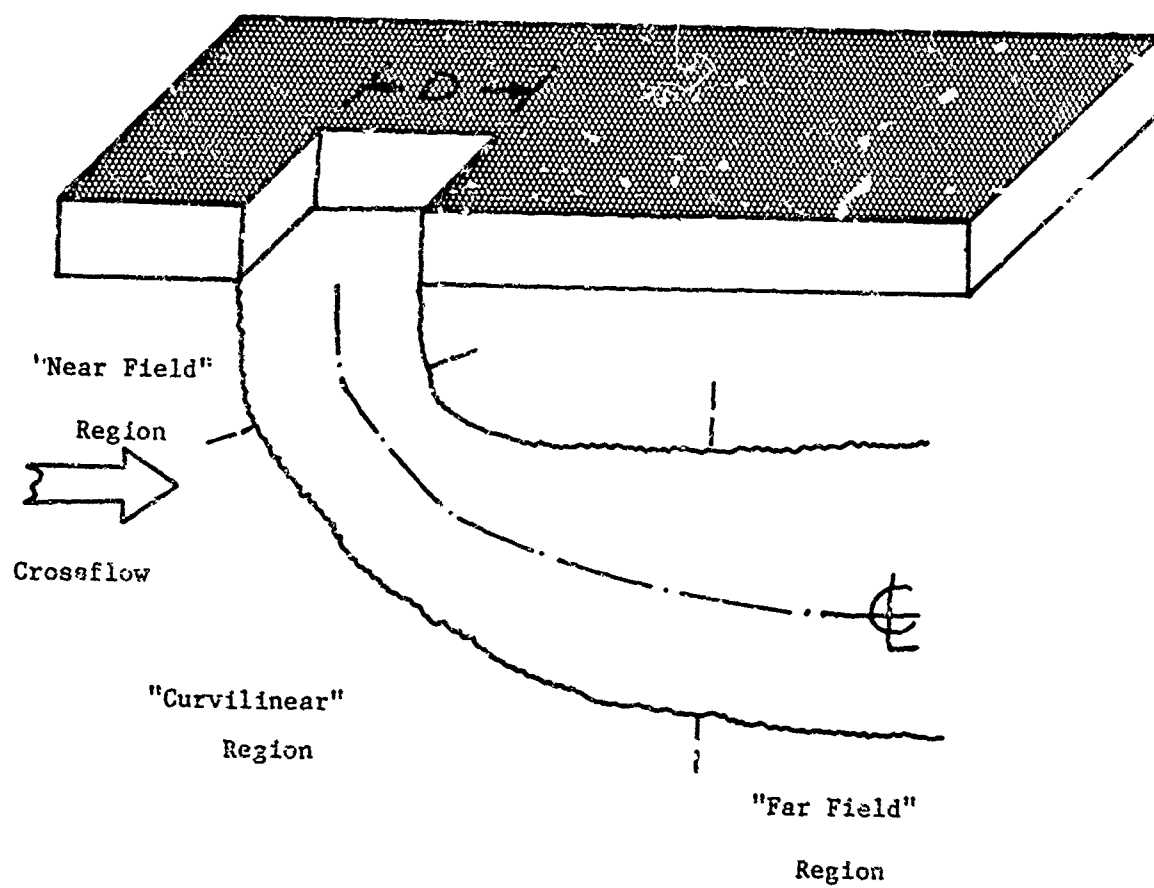


Figure 1. Jet Flowfield Schematic

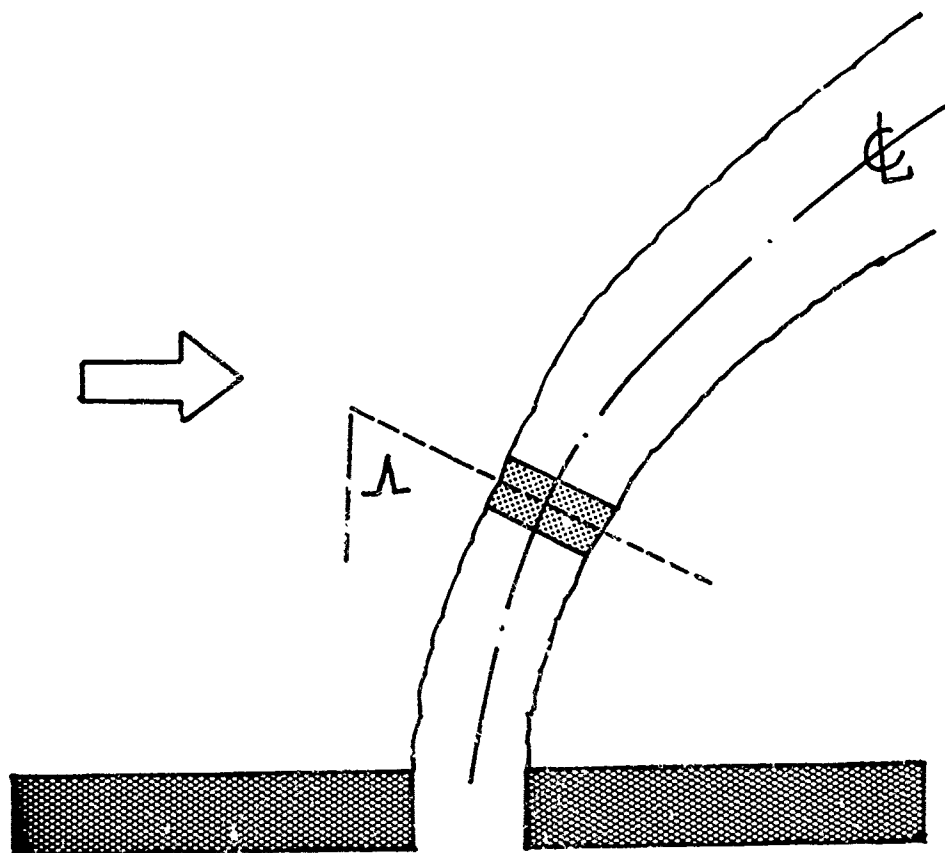


Figure 2. Jet Element Model: Abromovich Model

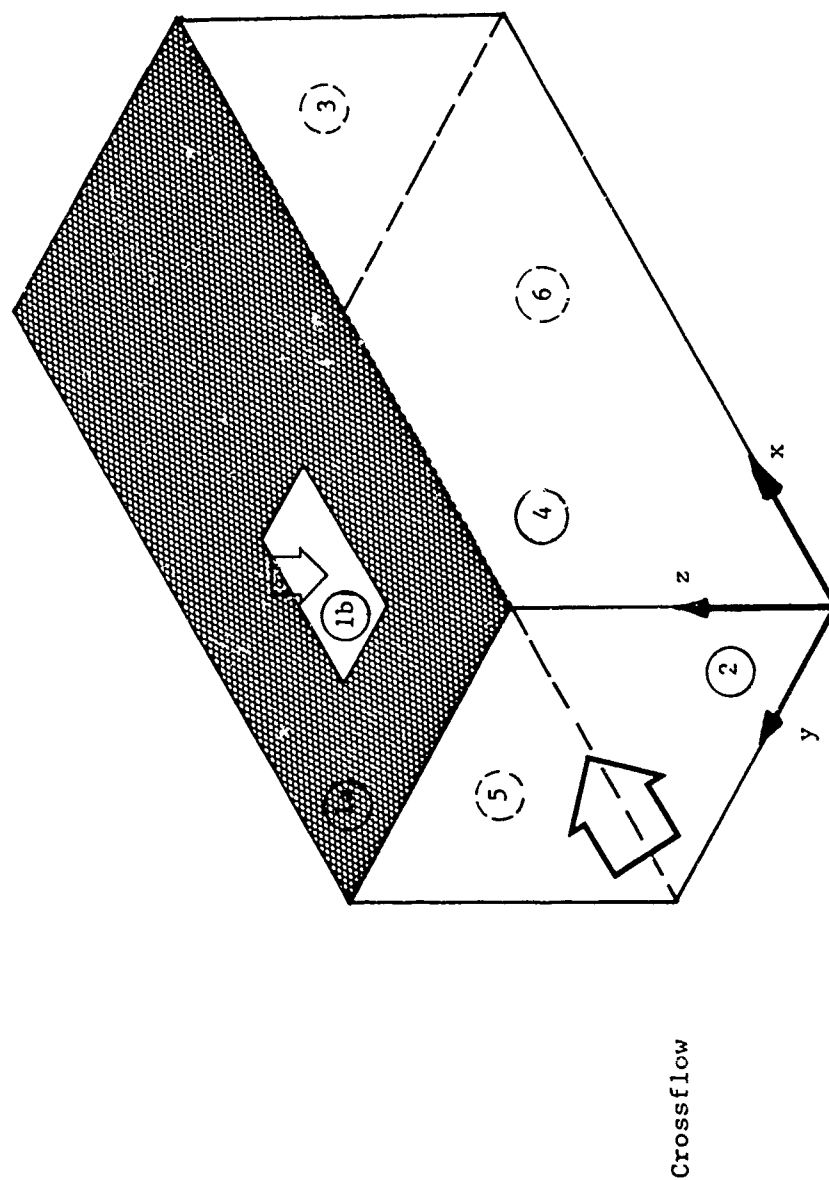
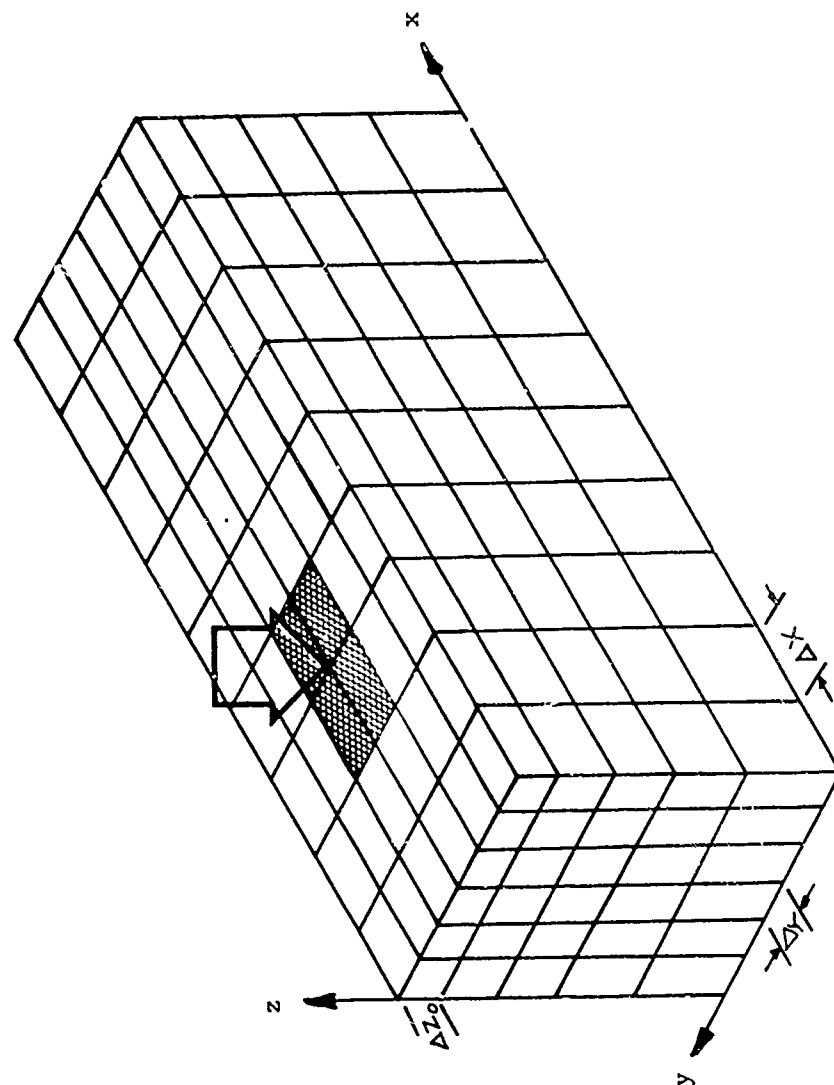


Figure 3. Computational Domain: Aircraft Jet Injection Model



Geometrically
Varying Z-Mesh

$$\Delta z_k = \Delta z_o K^{k-1}$$

Figure 4. Finite Subdivision of Computational Domain

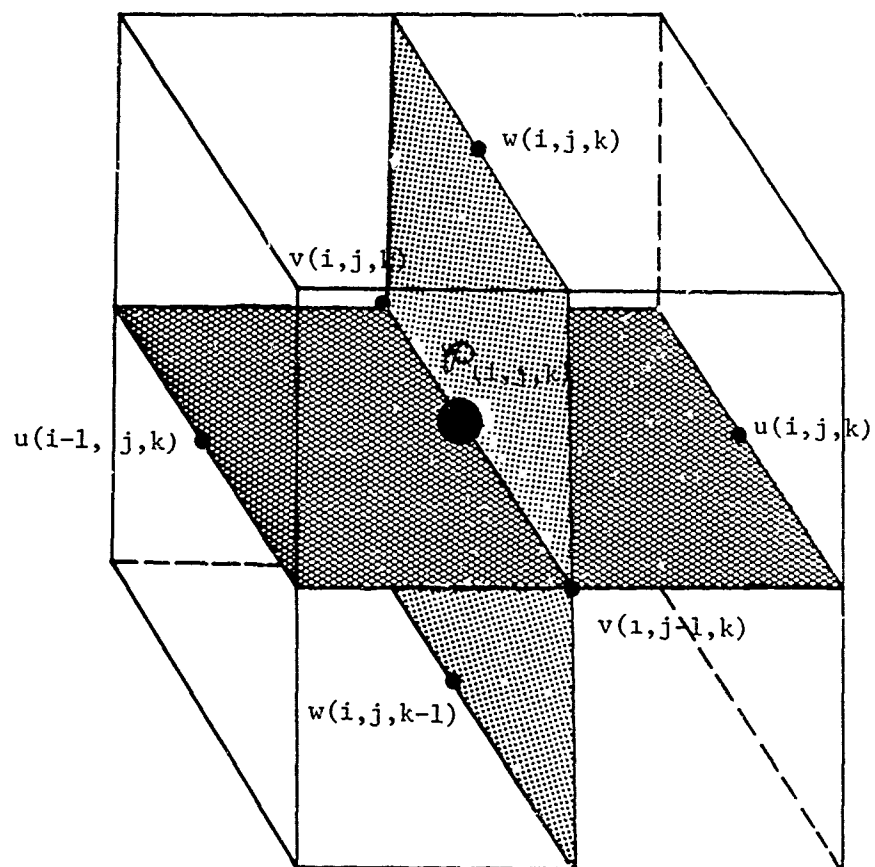


Figure 5. Staggered Mesh: Cell Variable Location

↑
Crossflow

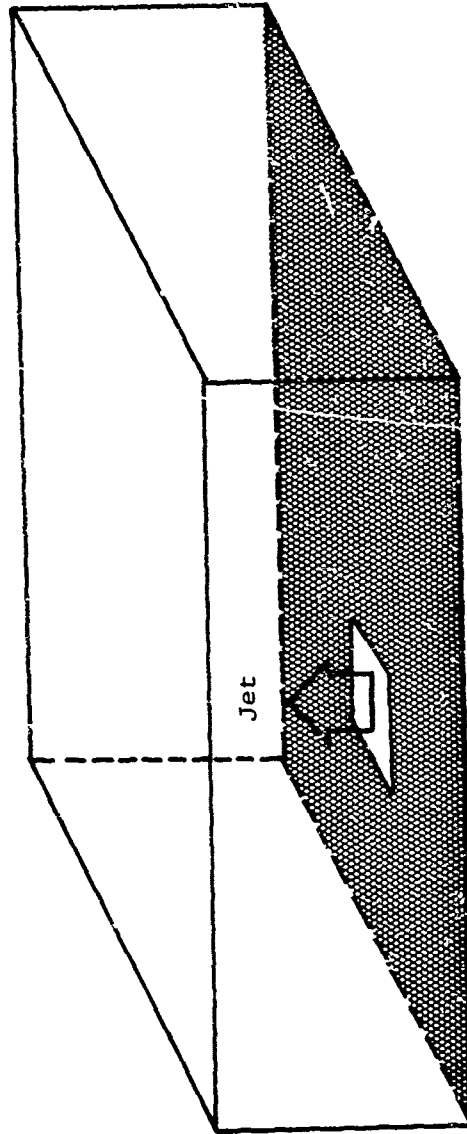


Figure 6. Computational Domain: Weston and Thames Experimental Model

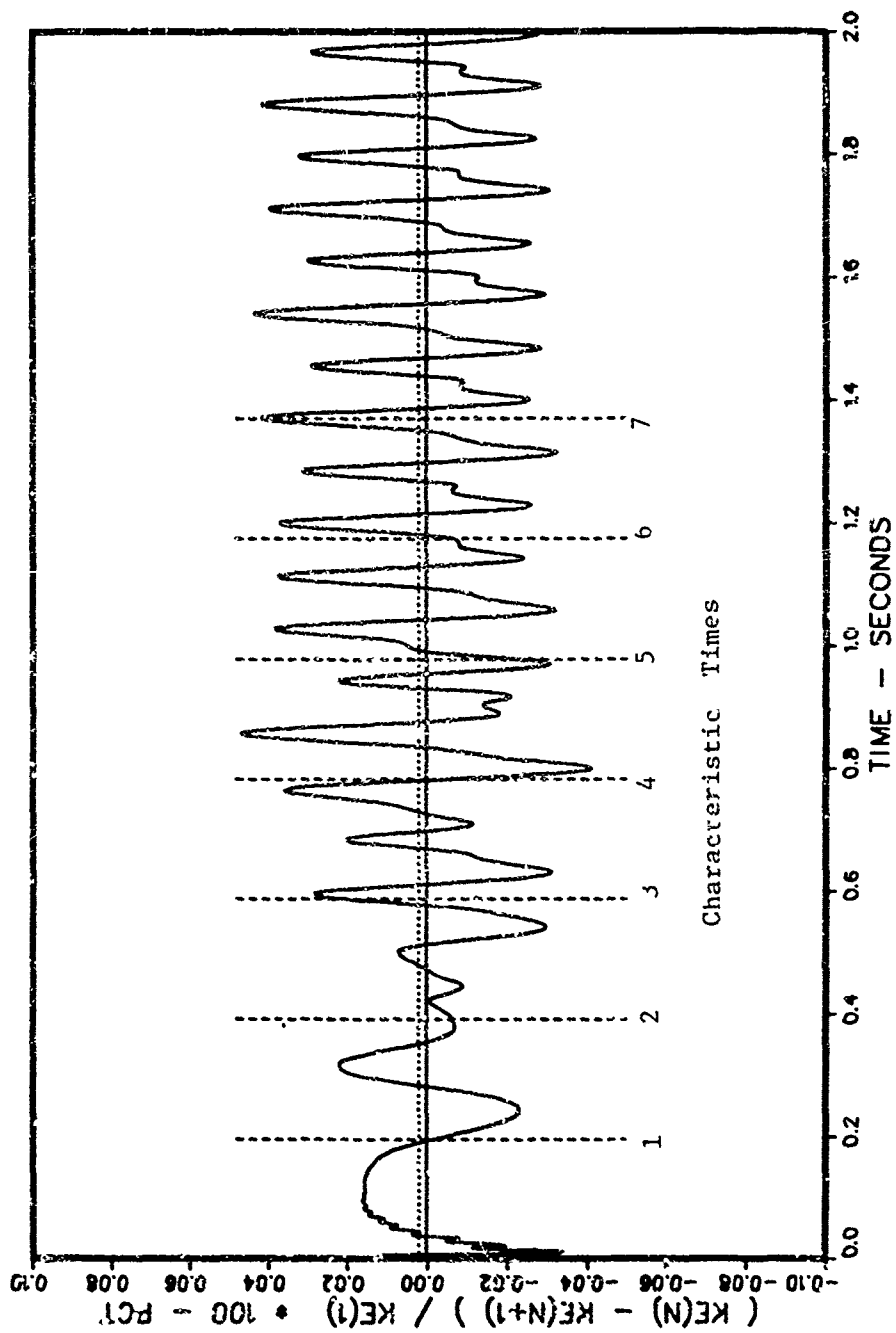


Figure 7. Convergence Criterion: Weston Simulation, K=1.1, Coarse Mesh

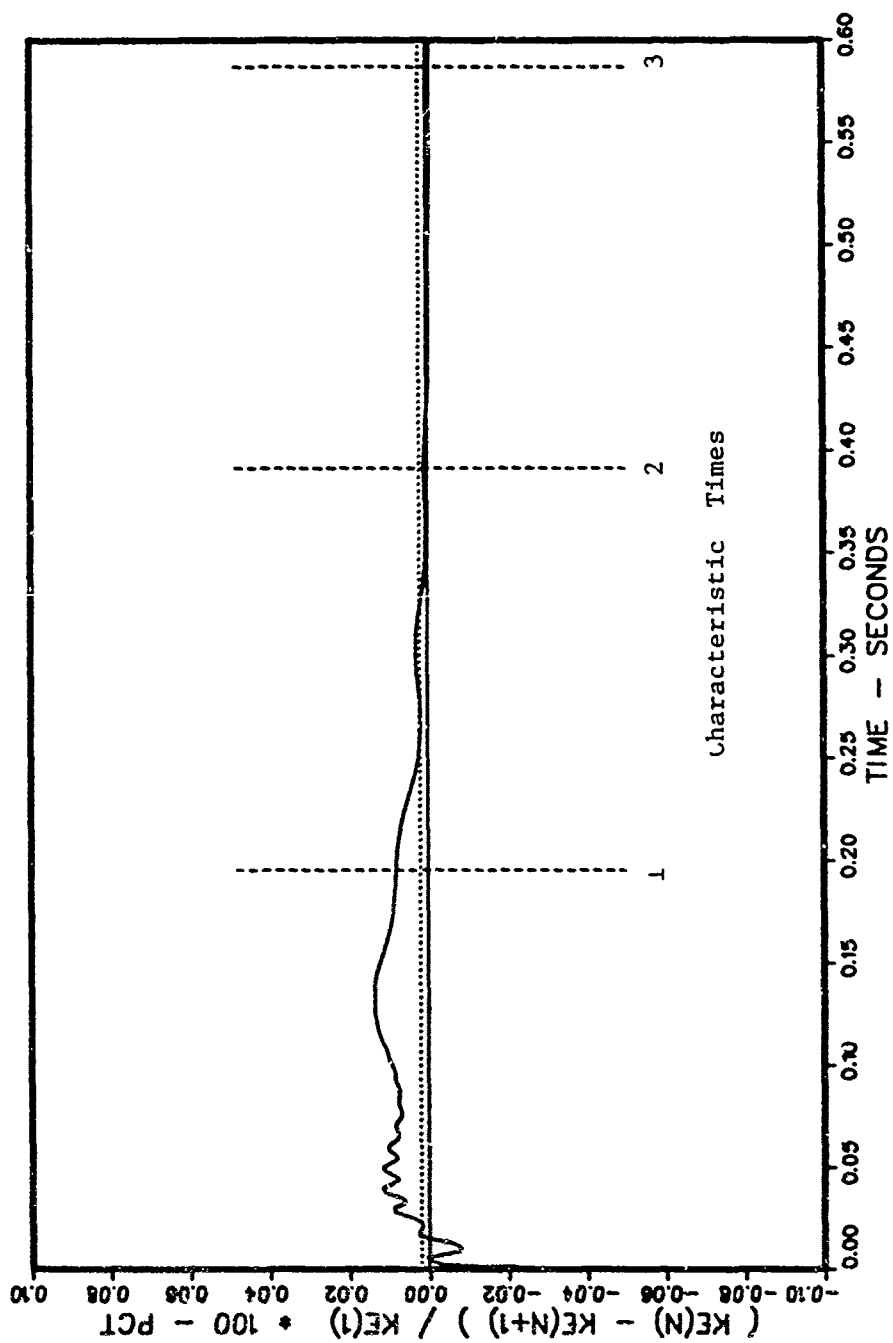


Figure 8. Convergence Criterion: Weston Simulation, K=1.05, Coarse Mesh

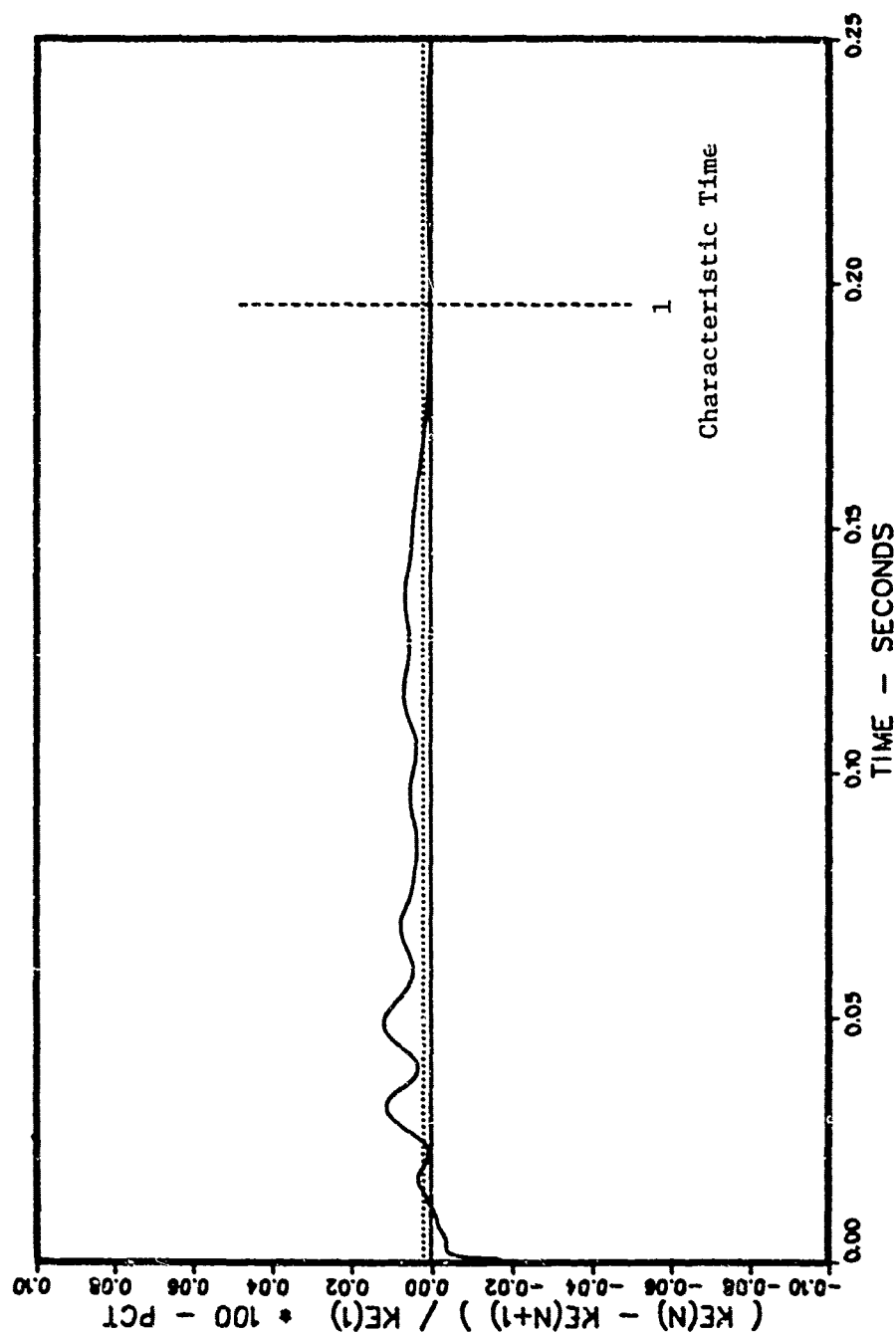


Figure 9. Convergence Criterion: Weston Simulation, $K=1.05$, Refined Mesh

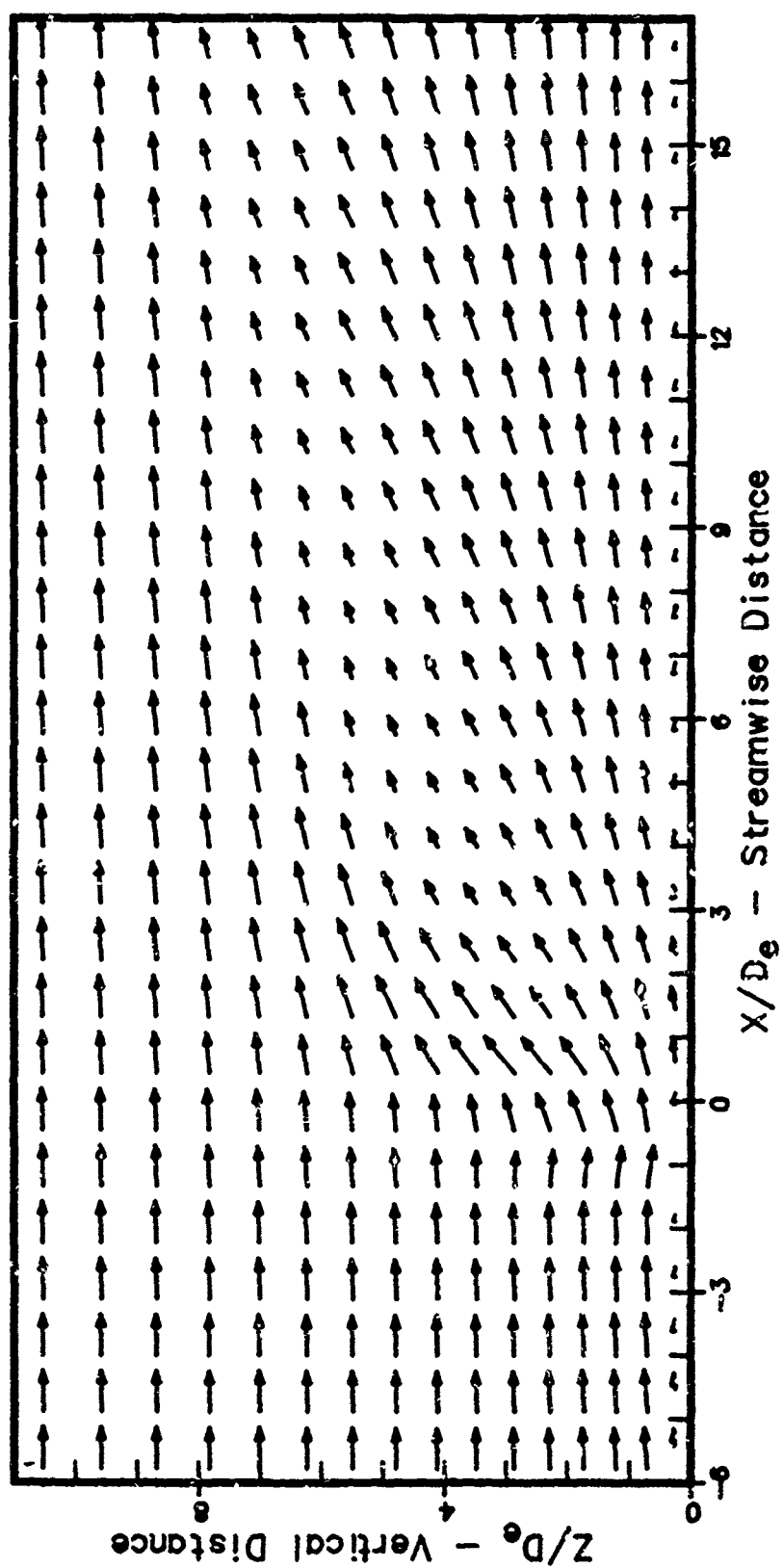


Figure 10a. Y-Plane Flowfield: Symmetry Plane -2

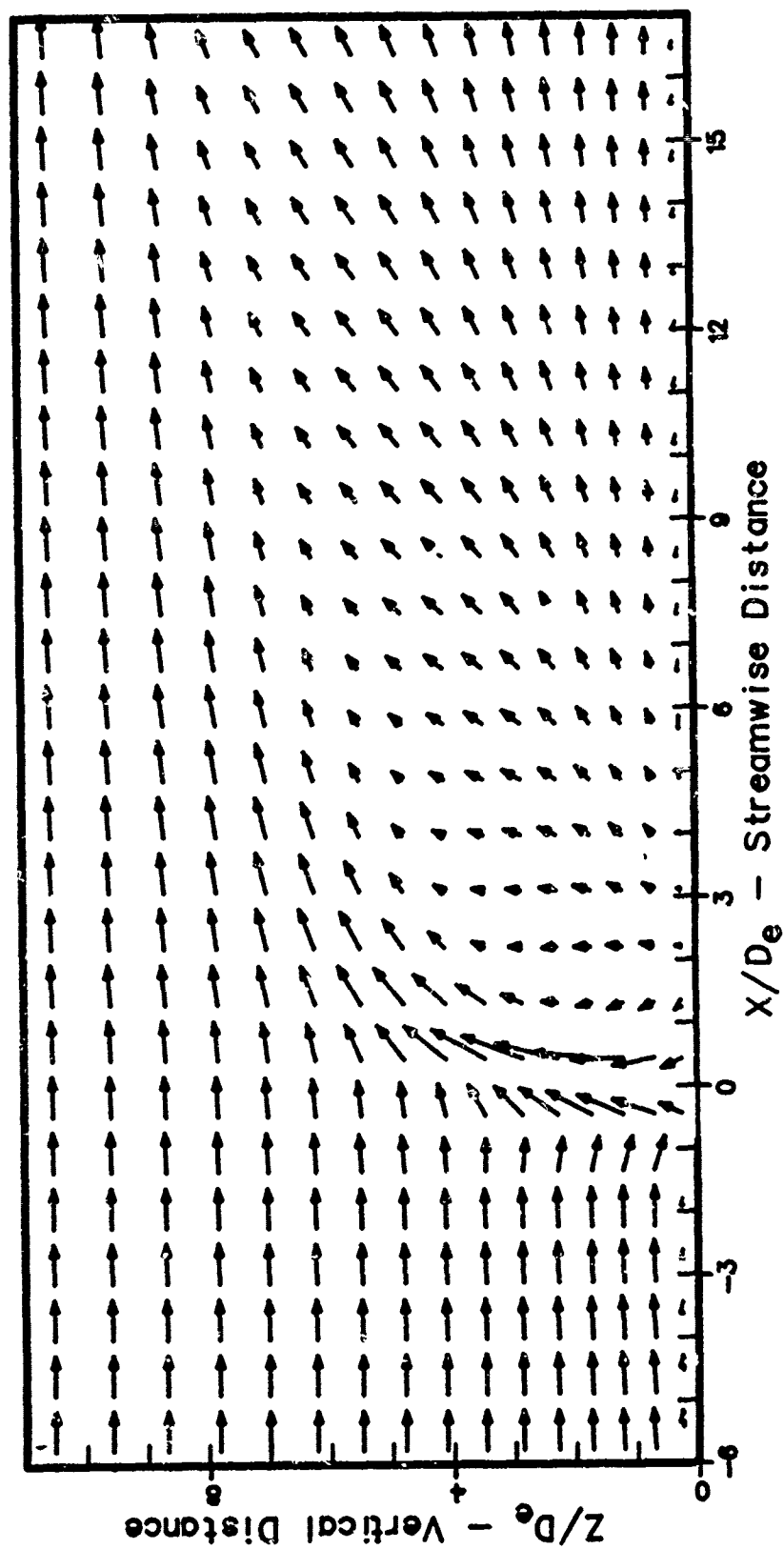


Figure 10b. Y-Plane Flowfield: Symmetry Plane -1

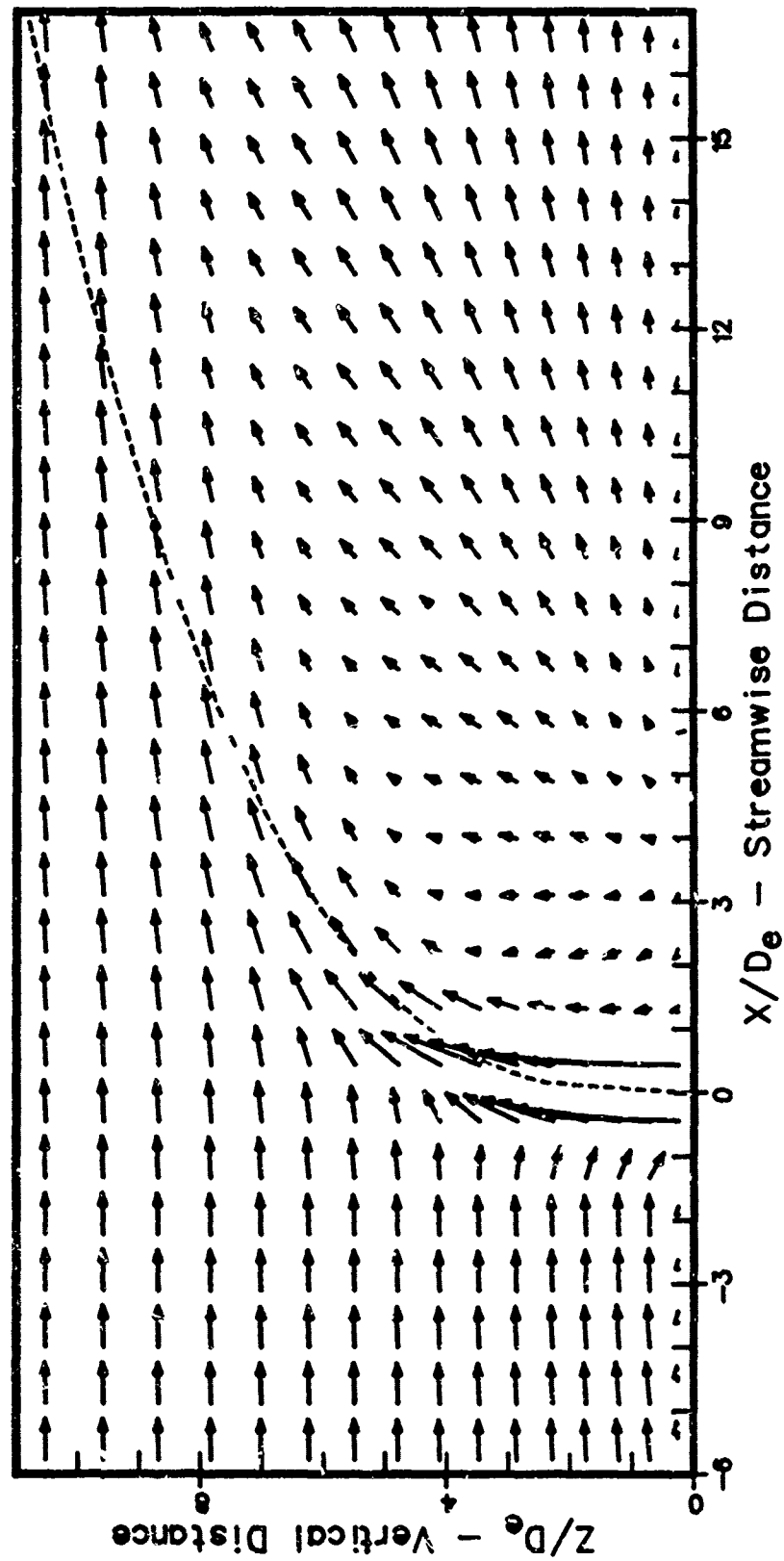


Figure 10c. Y-Plane Flowfield: Symmetry Plane

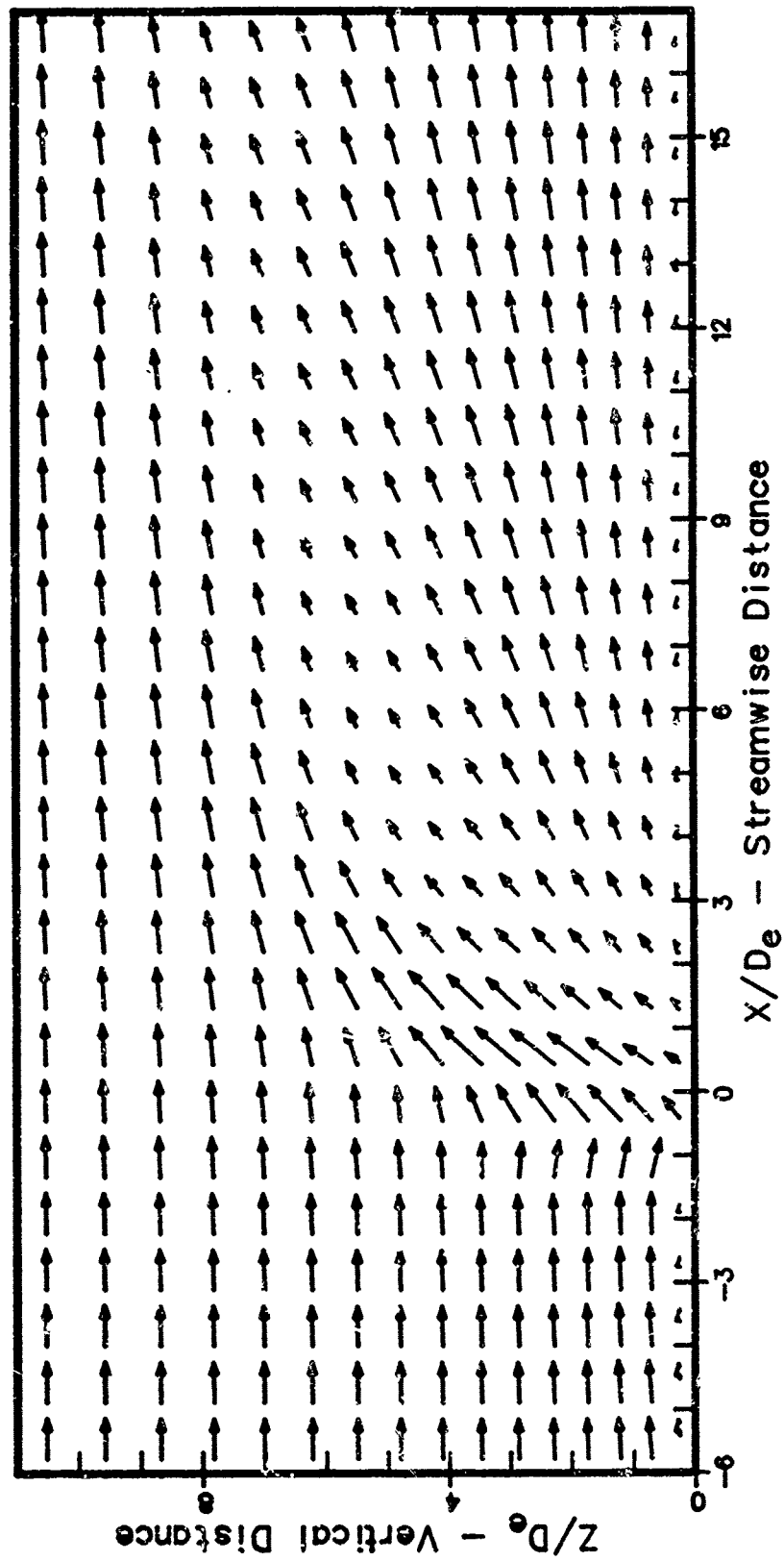


Figure 10d. Y-Plane Flowfield: Symmetry Plane +1

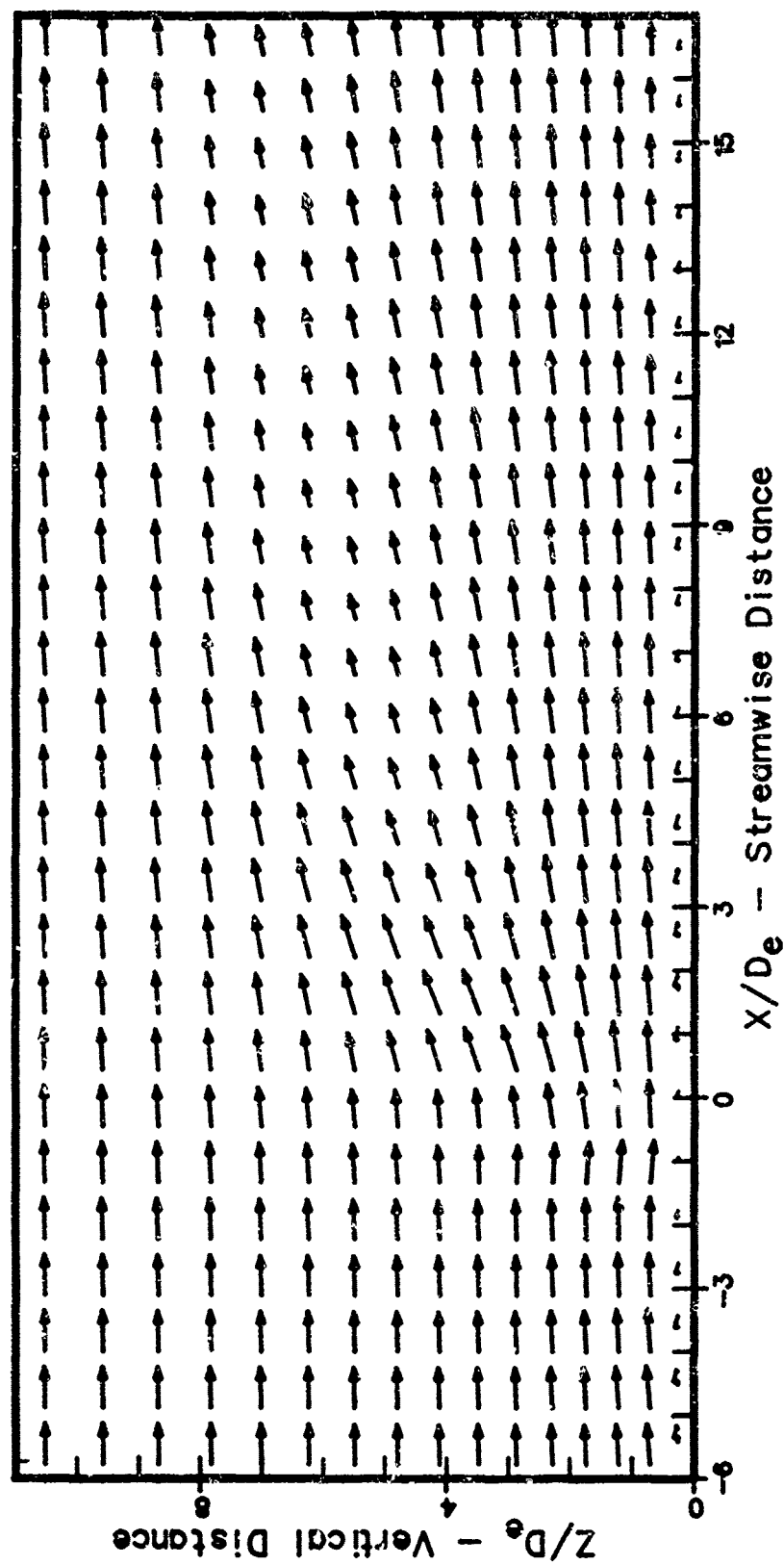


Figure 10e. Y-Plane Flowfield: Symmetry Plane +2

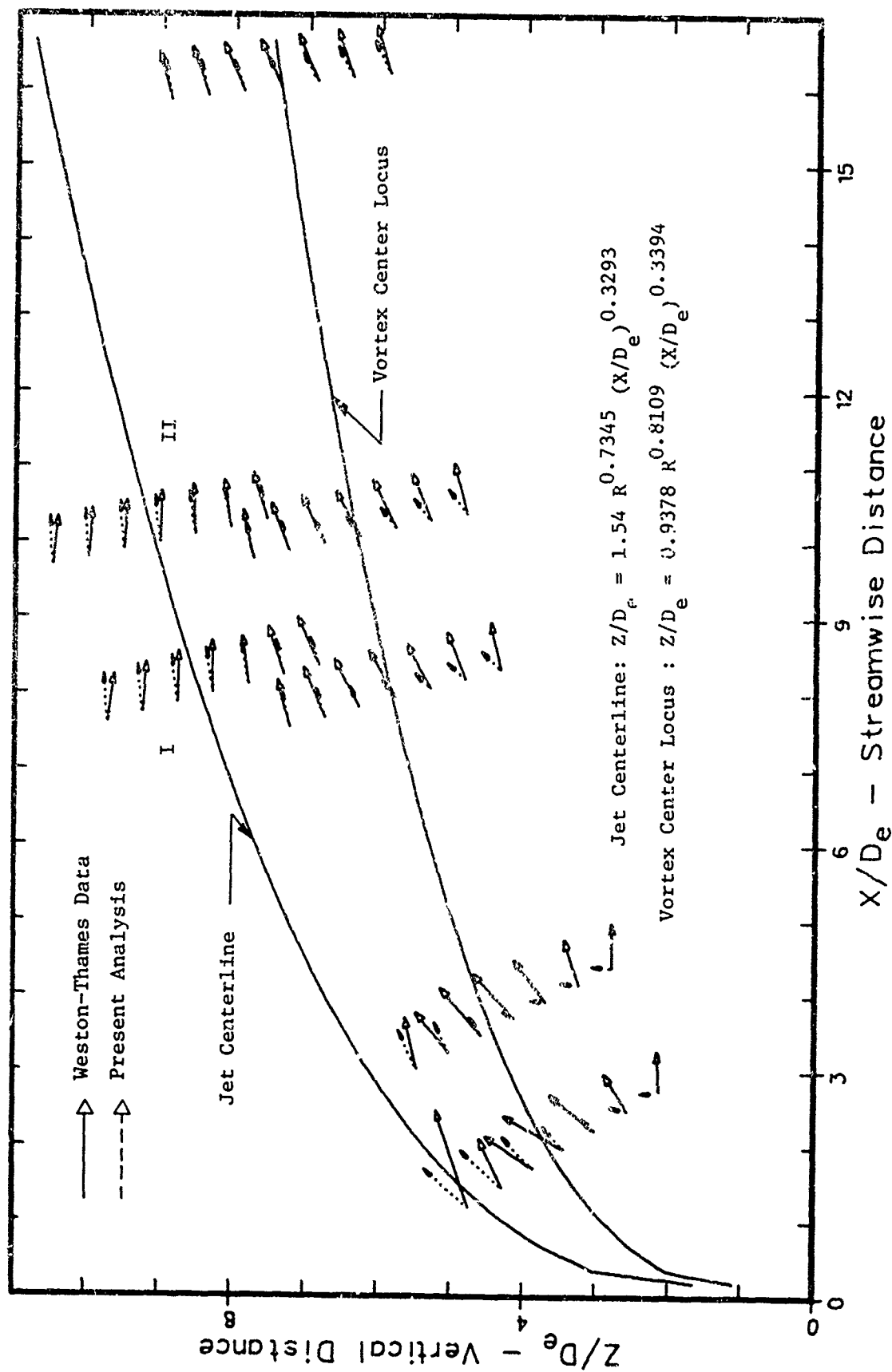


Figure 11. Experimental and Analytical Results, Symmetry Plane

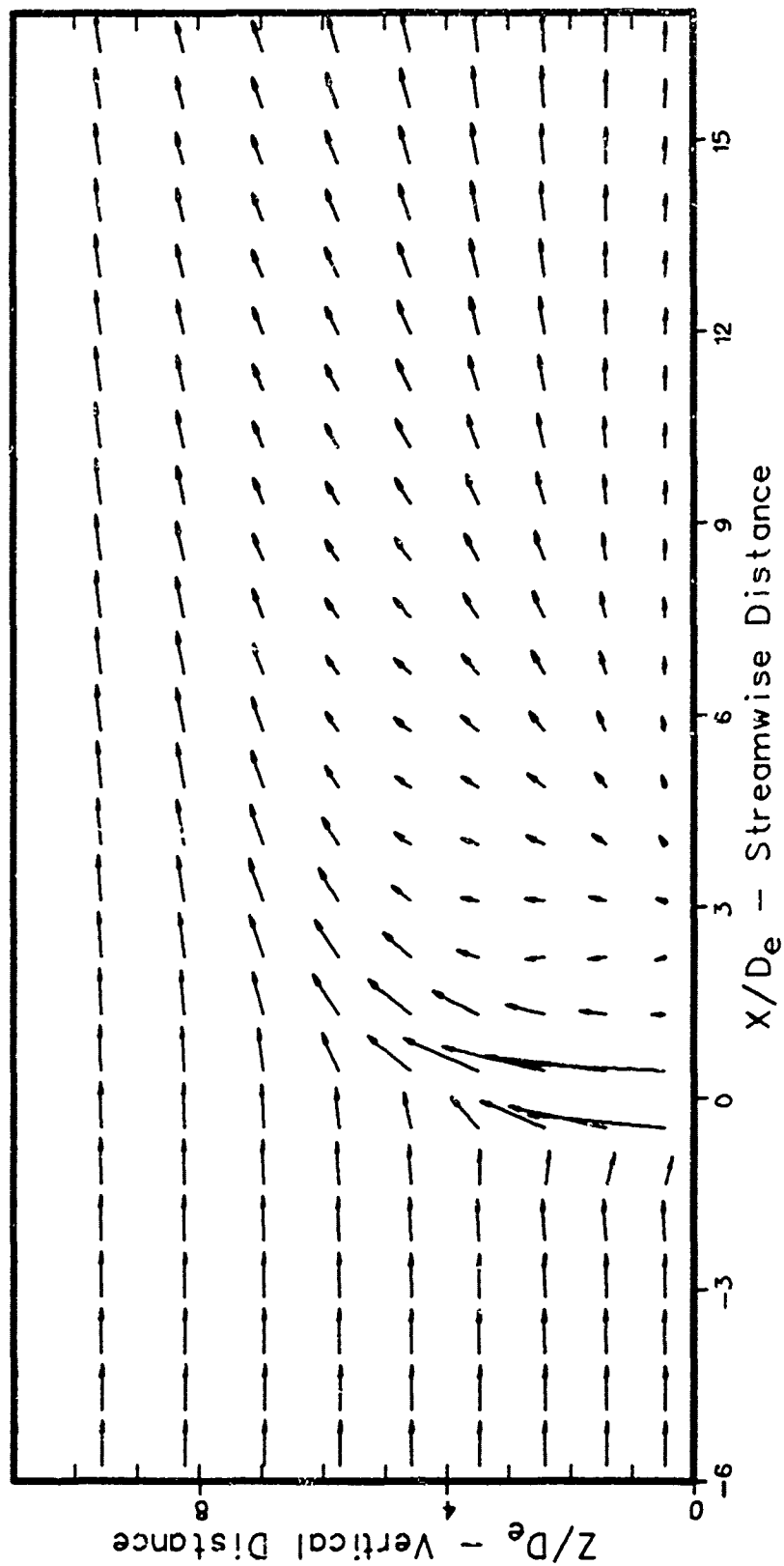


Figure 12. Symmetry Plane Flowfield: Coarse Mesh

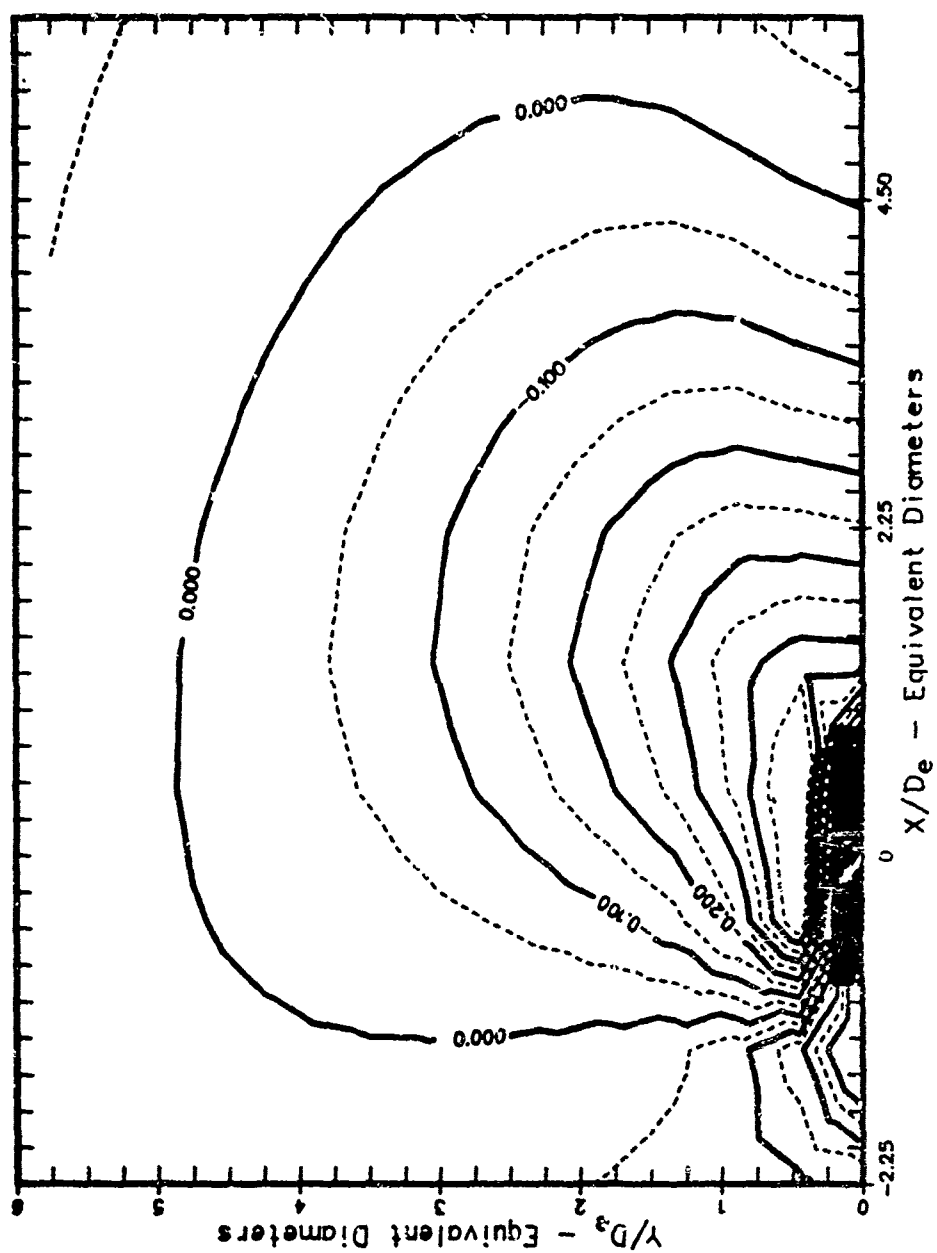


Figure 13a. Pressure Coefficient Contour Map: Right Half-Plane

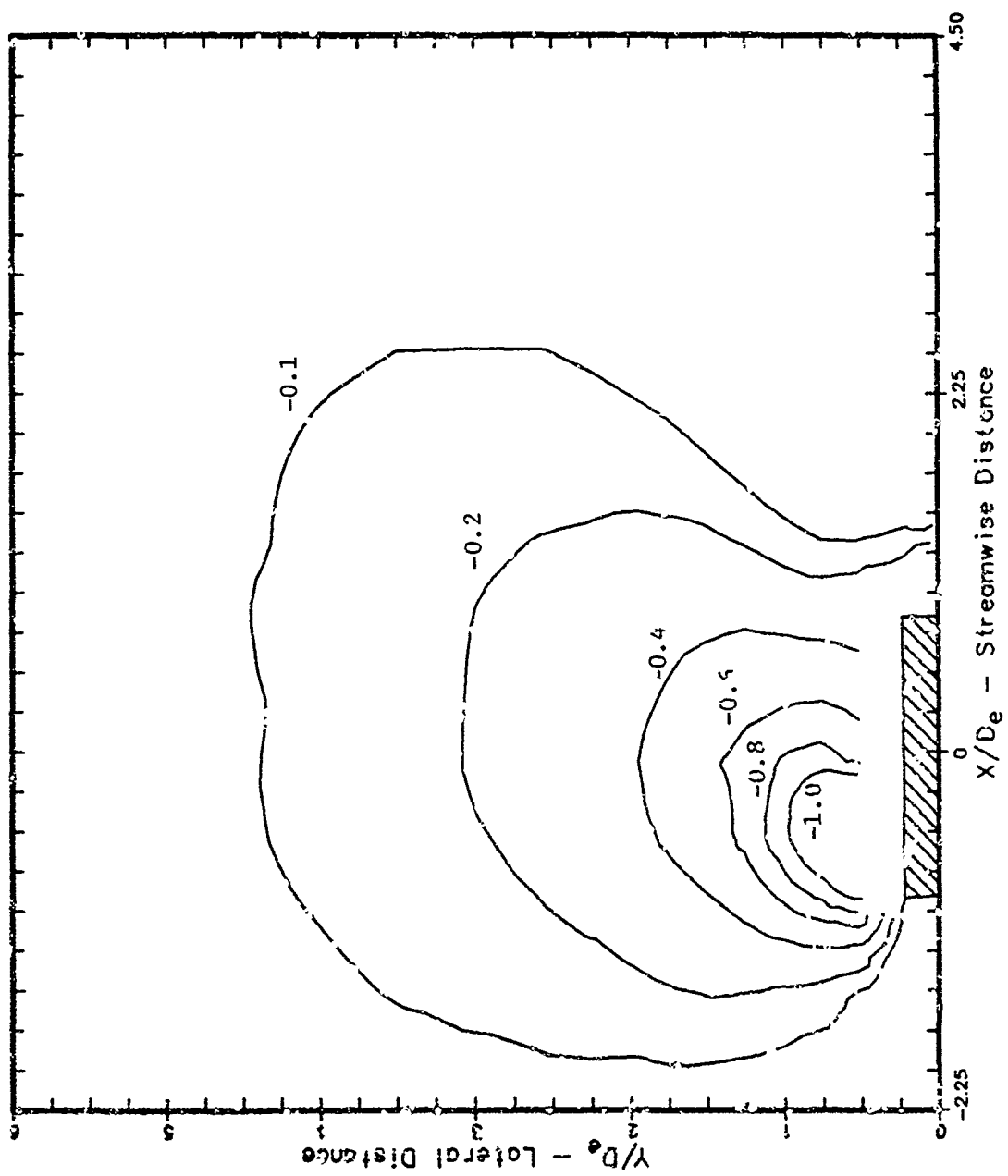


Figure 13b. Weston-Thames Pressure Coefficient Contour Map: Right Half-Plane, $R=4.01$

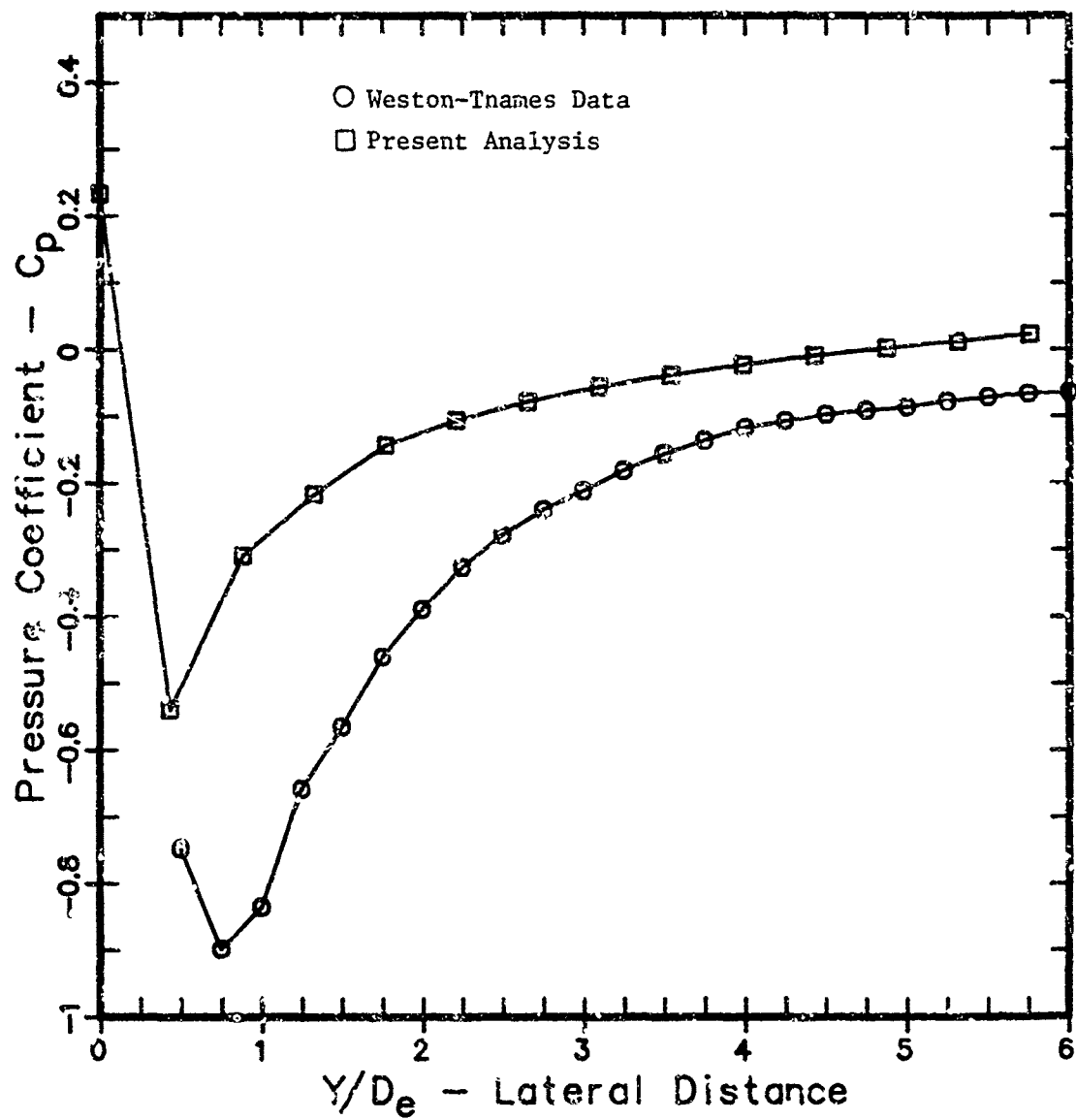


Figure 13c. Pressure Coefficient Correlation: $R=4$, $X/D_e \approx 0.0$

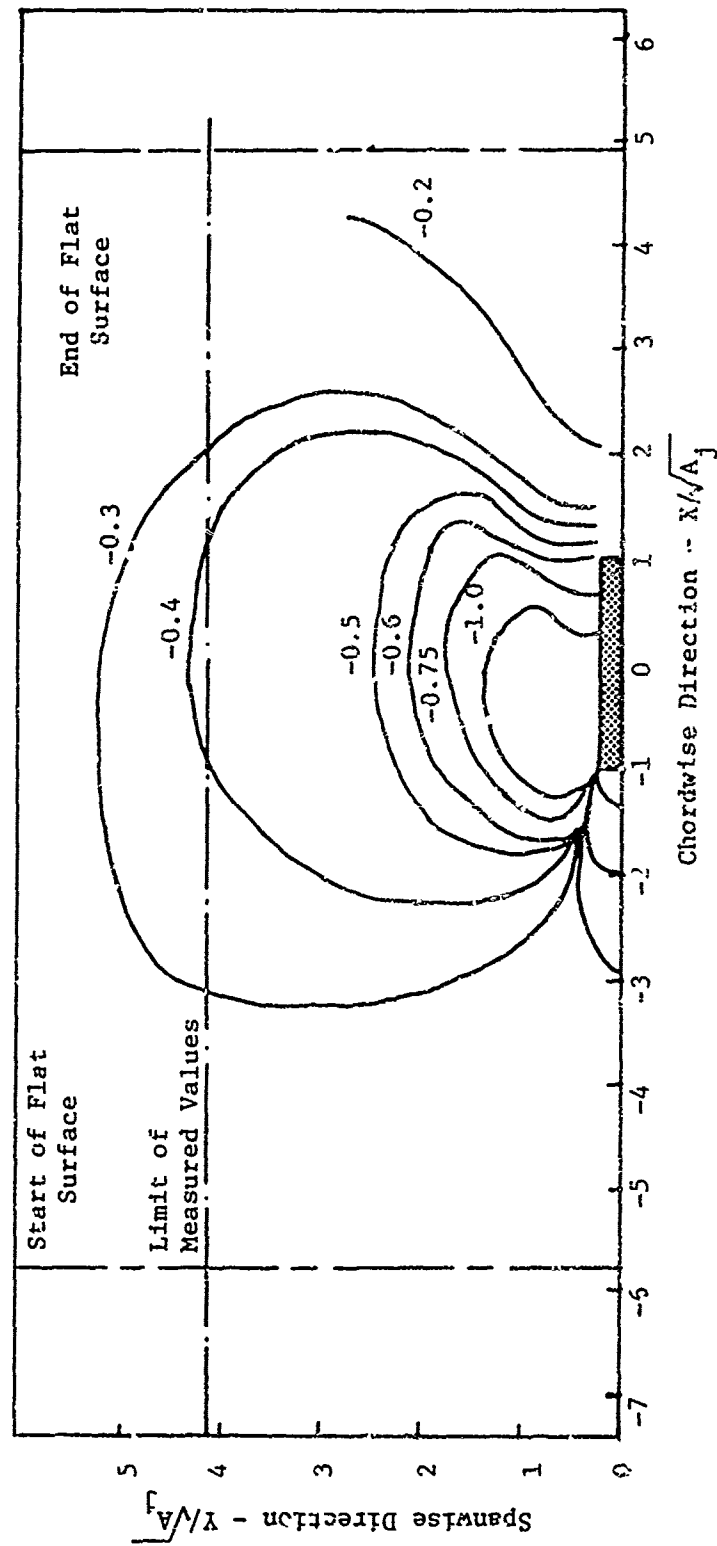


Figure 14a. Peake Experiment Pressure Coefficient Contour Map, $R=4.0$

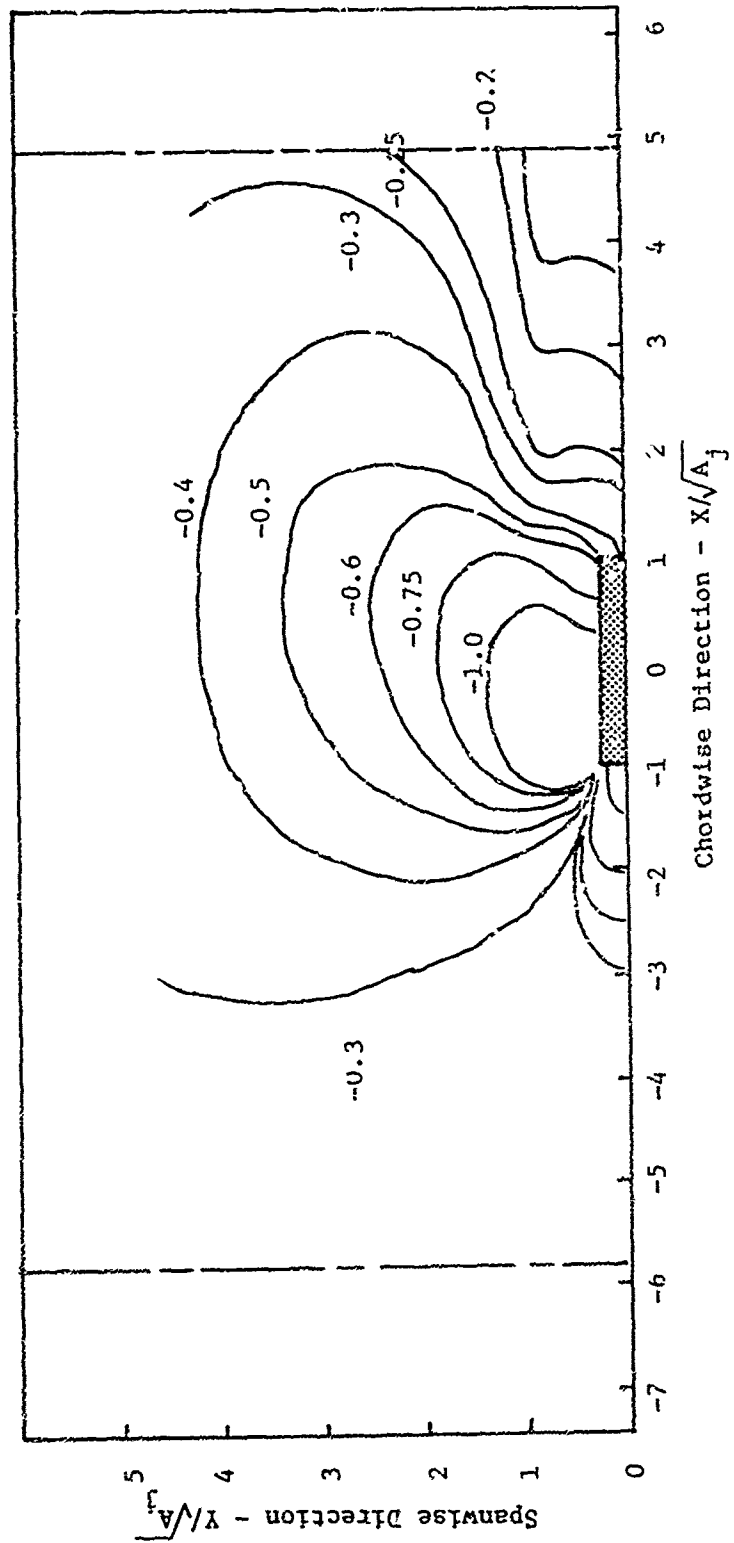


Figure 14b. Peak Experiment Pressure Coefficient Contour Map, $R=4.1$

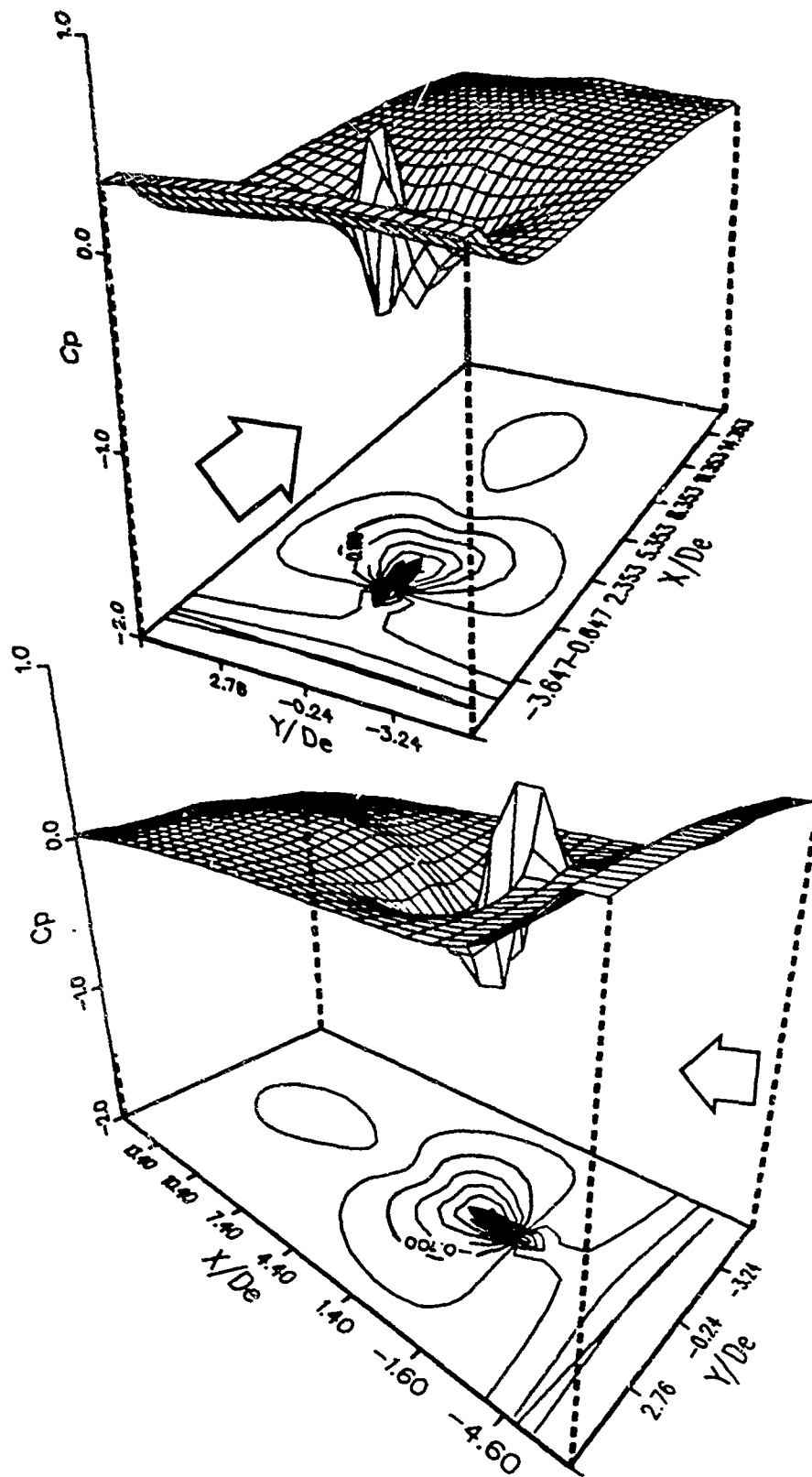


Figure 15. Surface Pressure Distribution

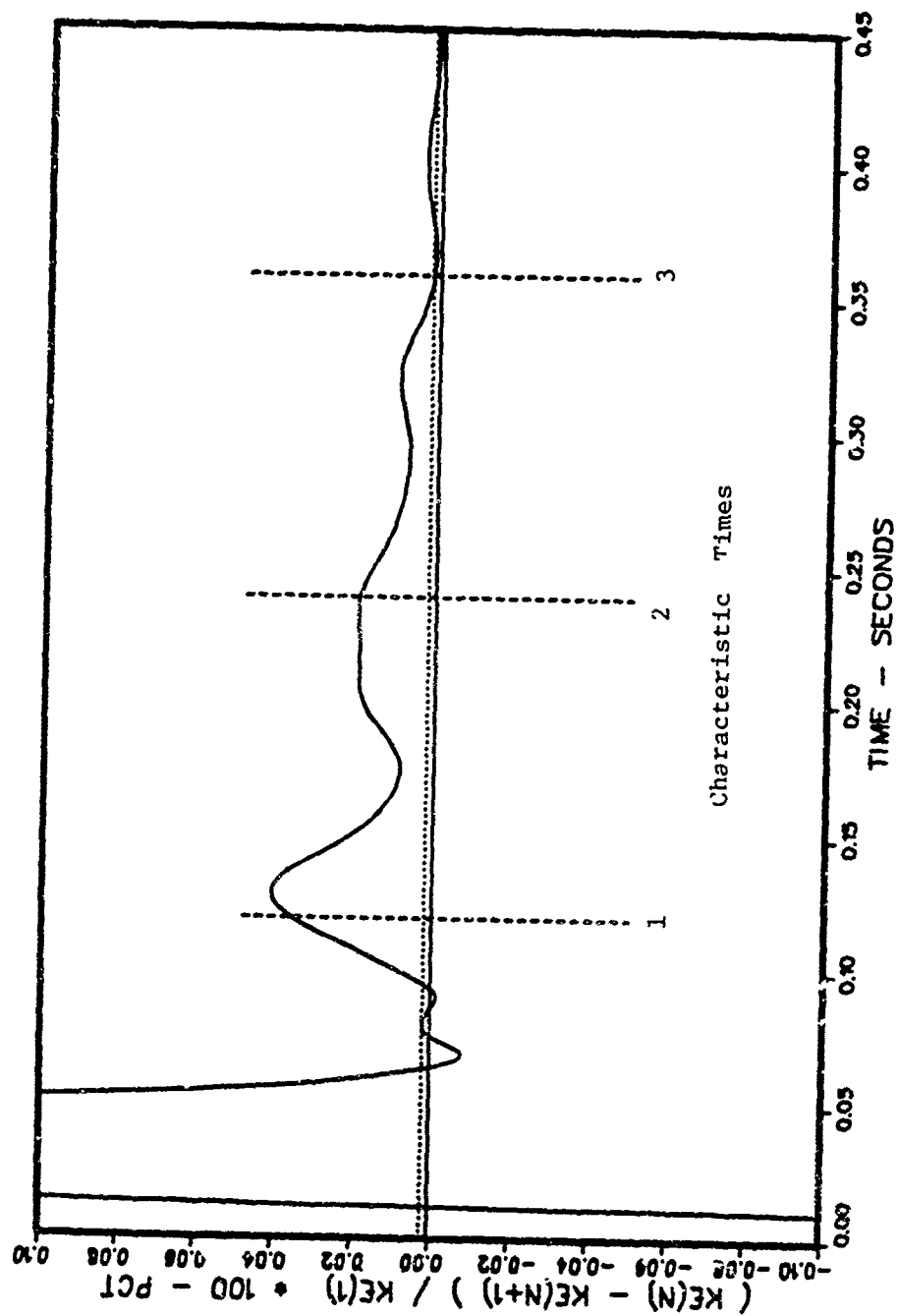


Figure 16. Convergence Criterion: AFWL Gas, K=1.2, Coarse Mesh

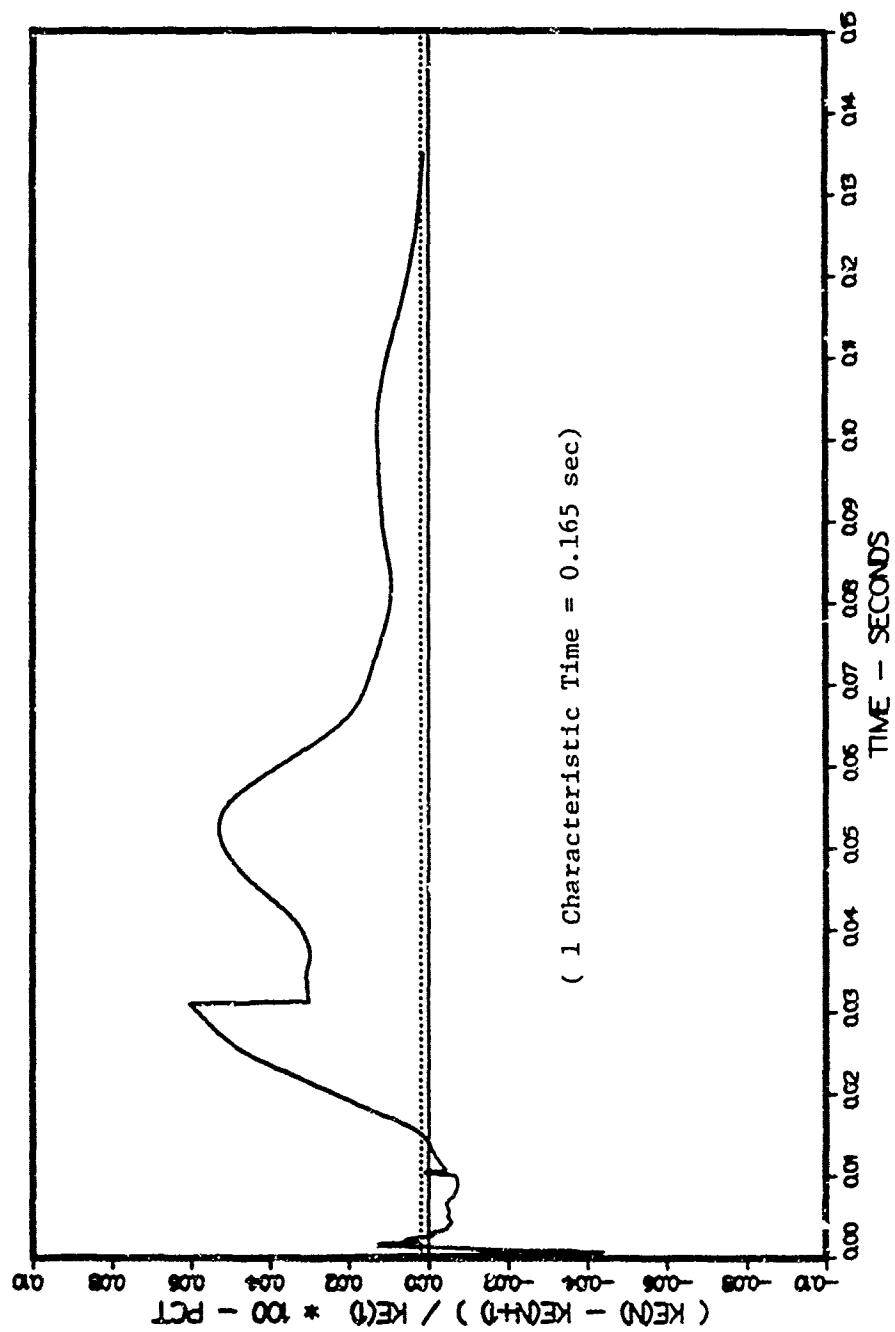


Figure 17. Convergence Criterion: AFWL Gas, K=1.09, Fine Mesh

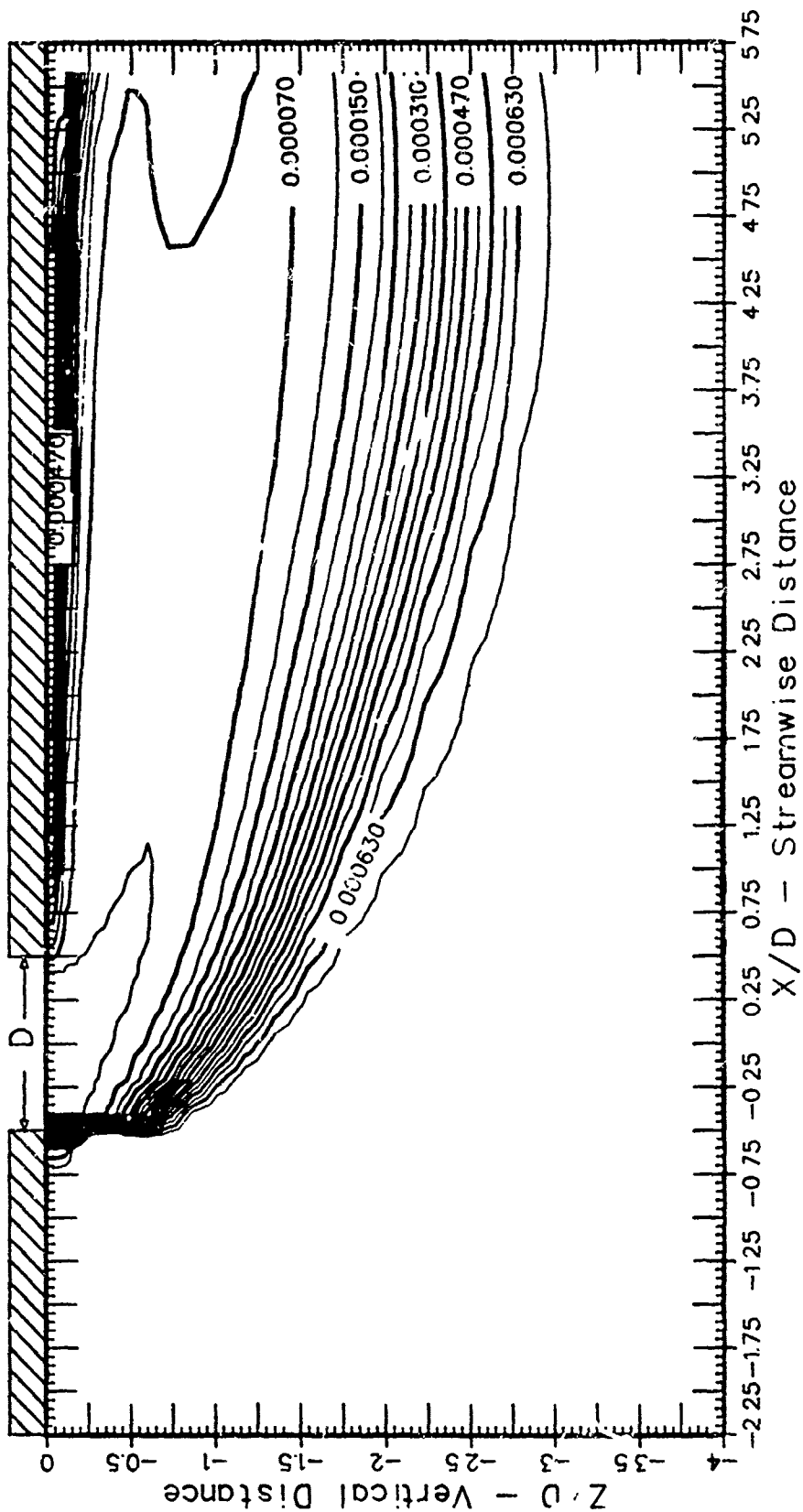


Figure 18. Trajectory Analysis: Density Contour Map, AFWL Gas

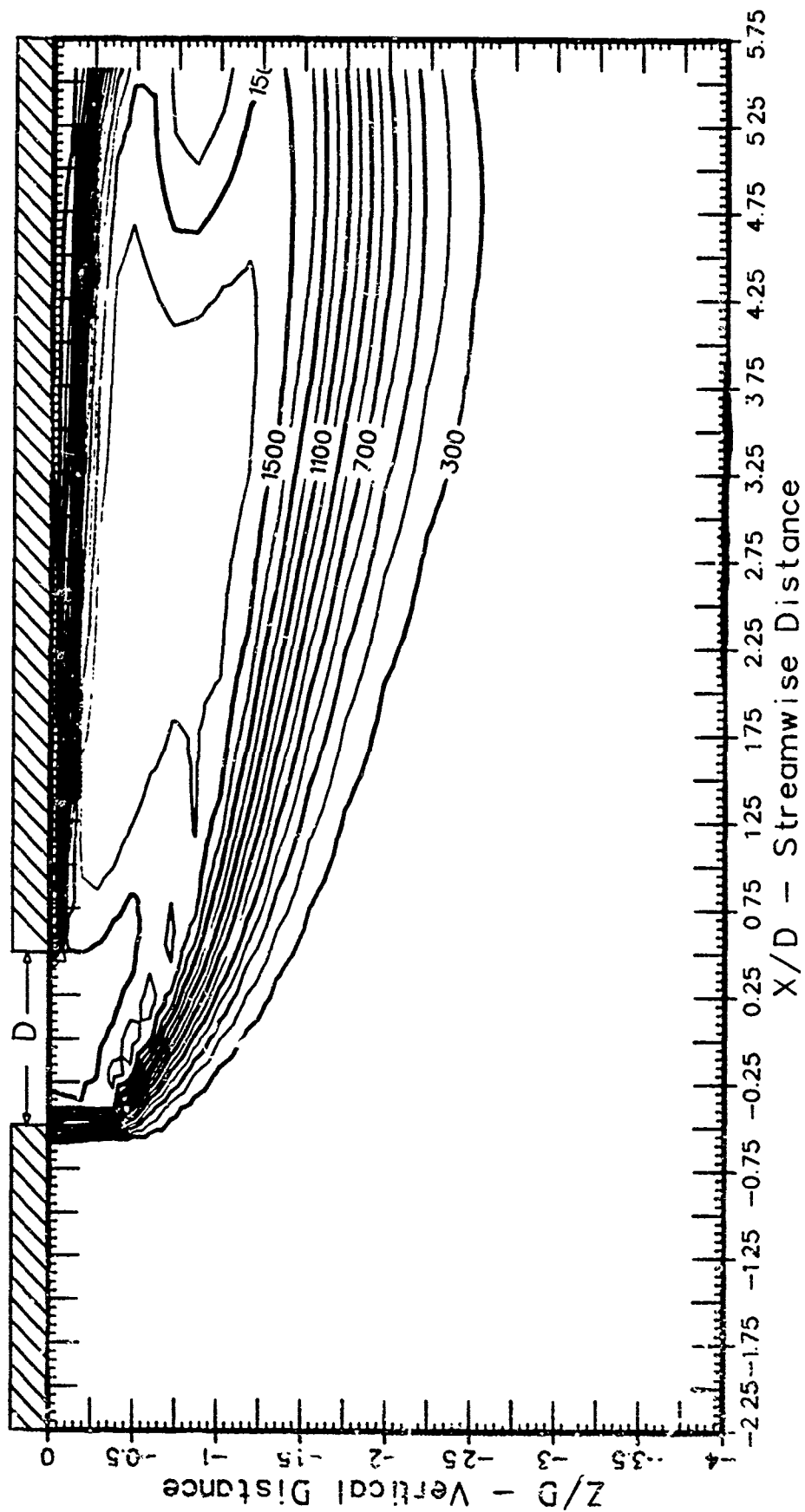


Figure 19. Trajectory Analysis: Temperature Contour Map, AFWL Gas

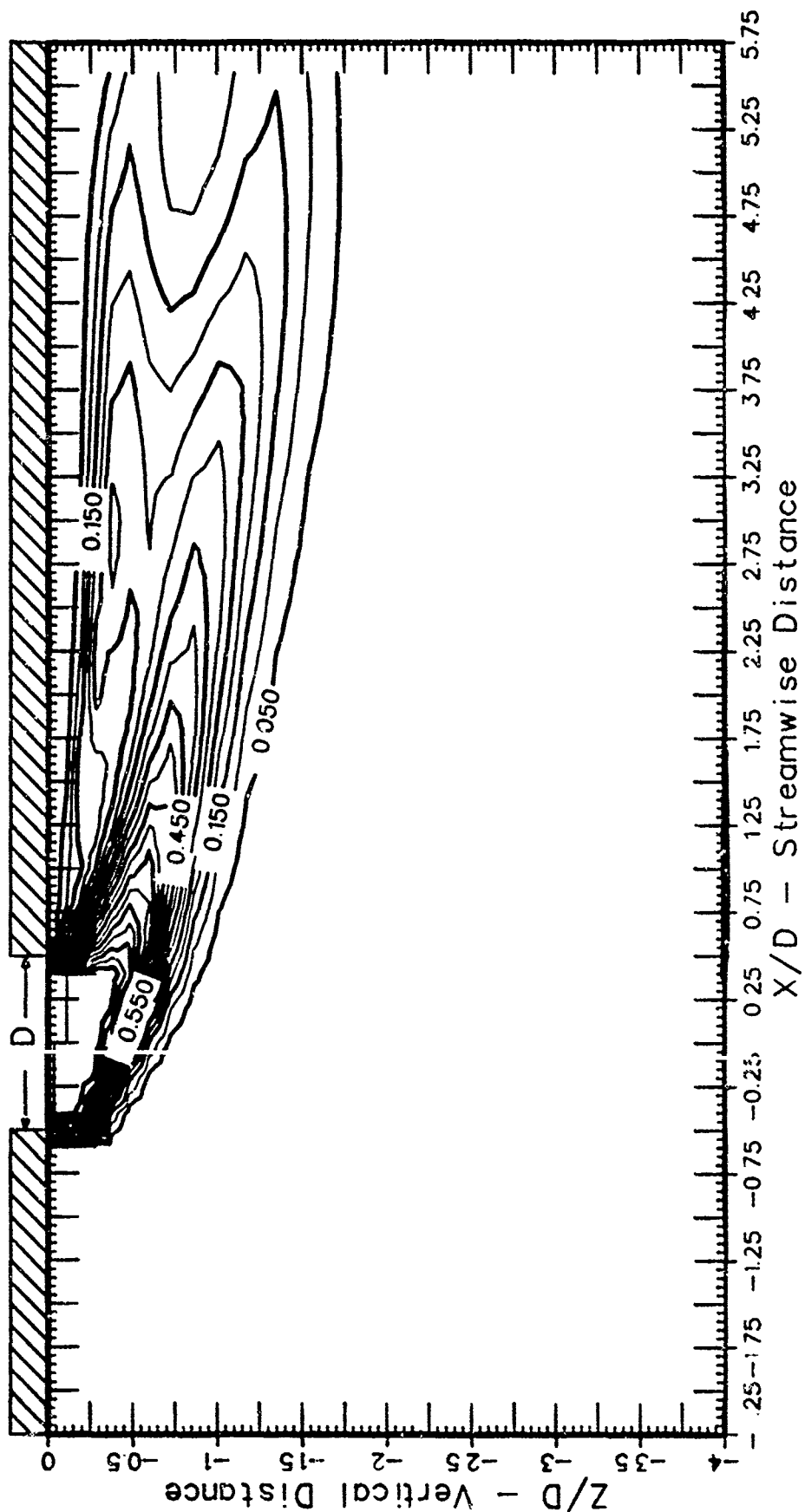


Figure 20. Trajectory Analysis: Mass Fraction Contour Map, AFWL Gas

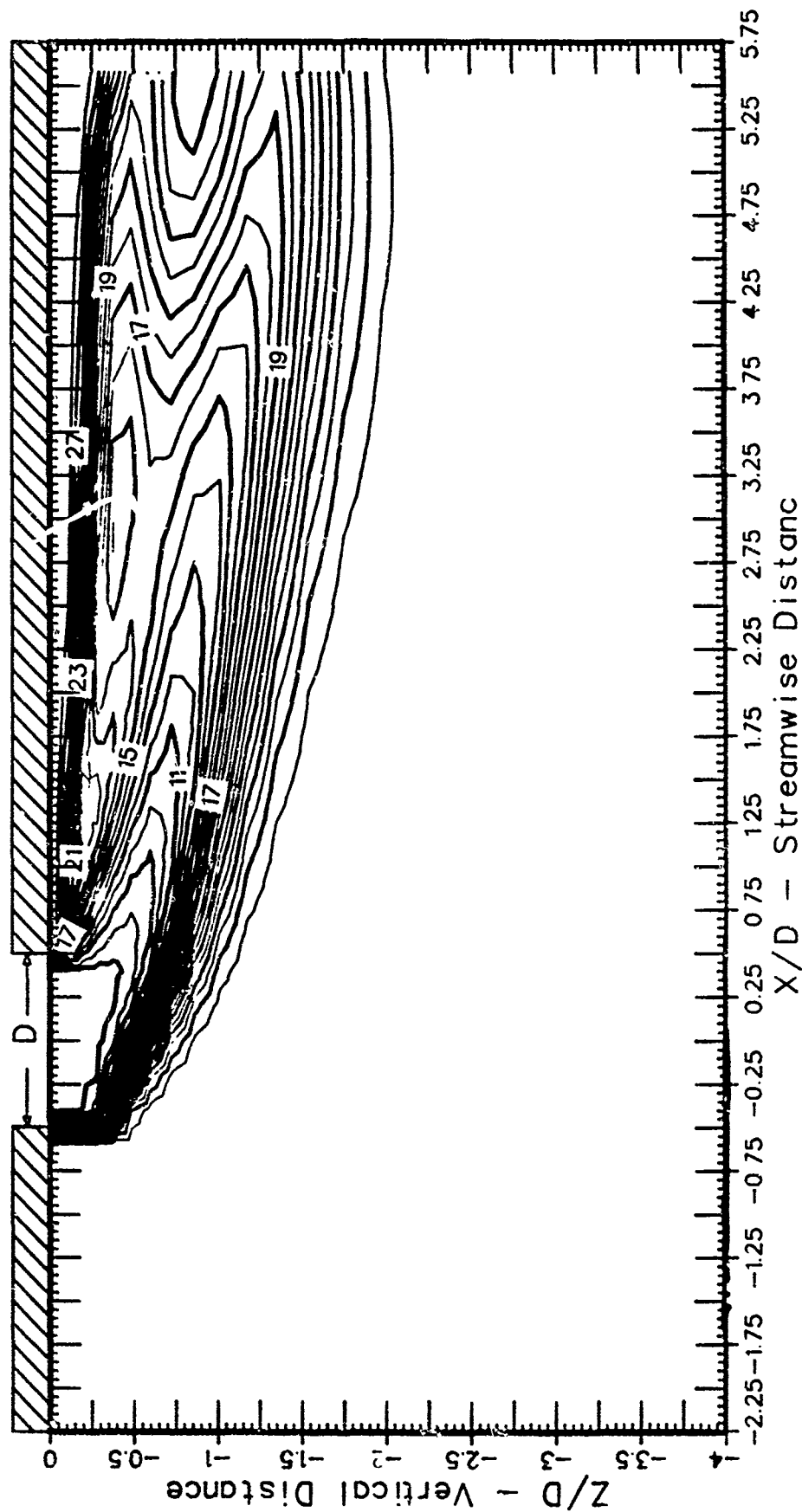


Figure 21. Trajectory Analysis: Molecular Weight Contour Map, AFWL Gas

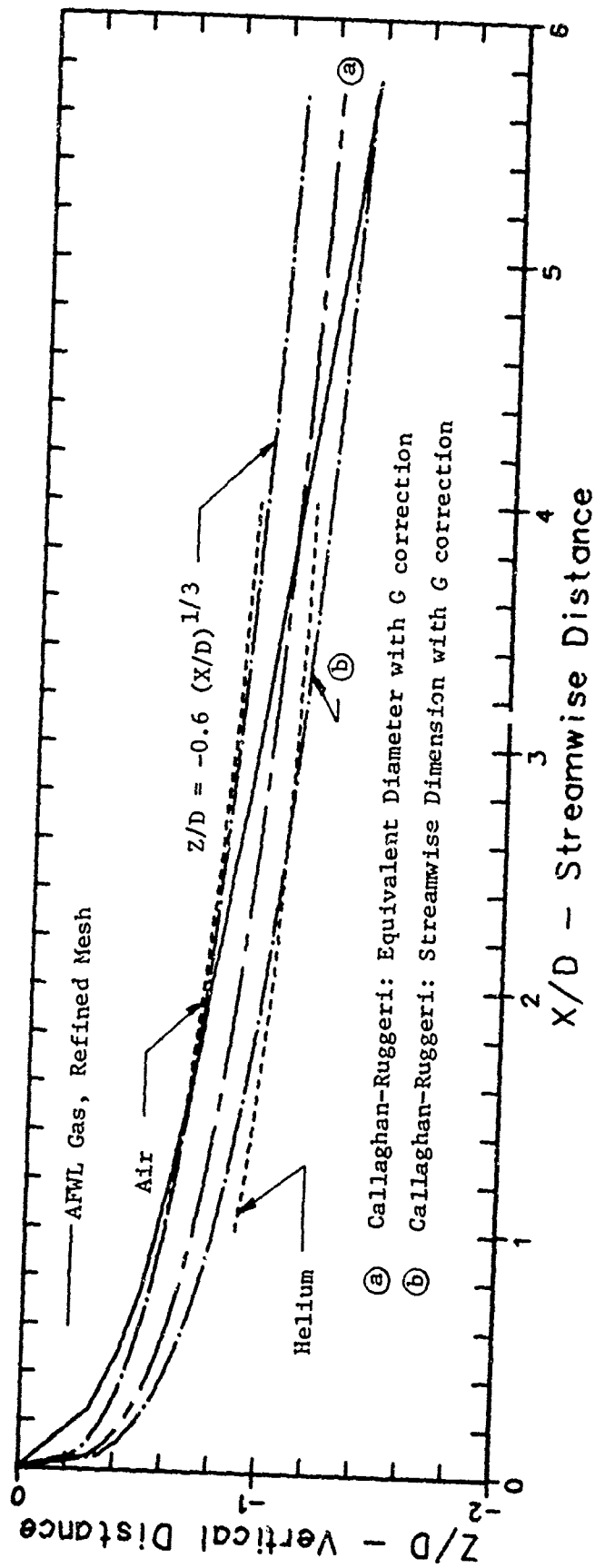


Figure 22. Jet Trajectory Comparisons

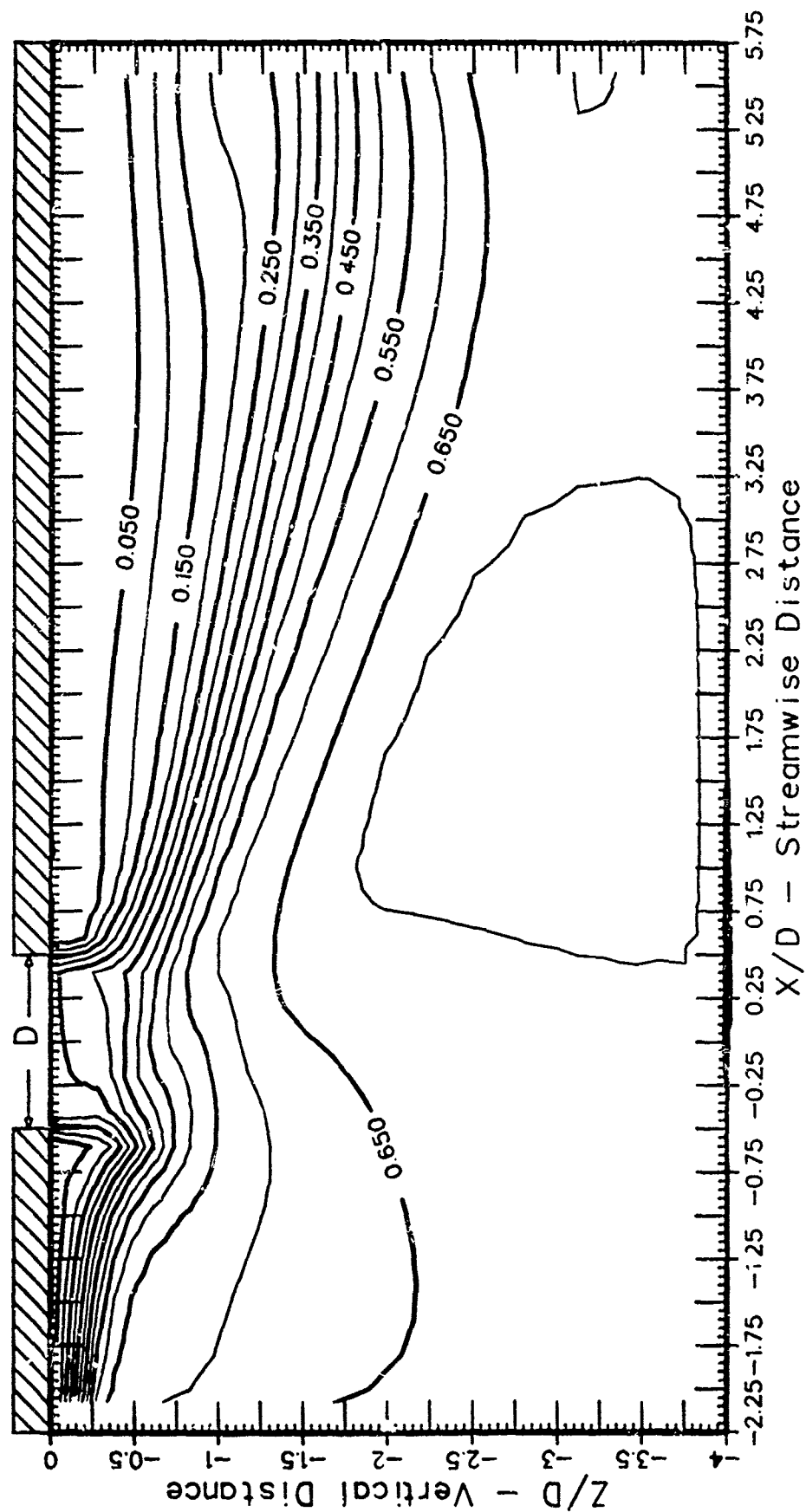


Figure 23. Flowfield Analysis: Mach Number Contour Map, AFWL Gas

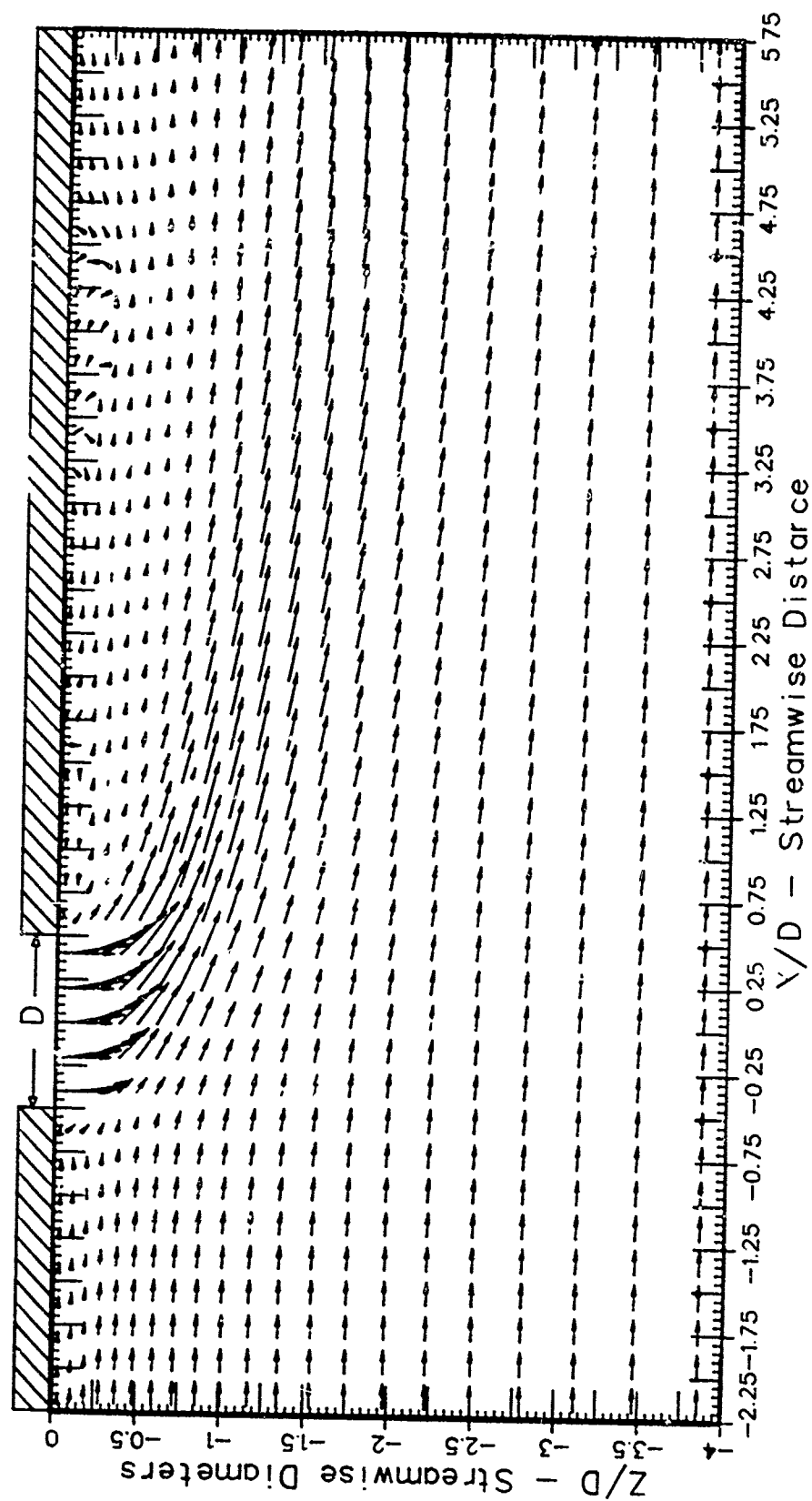


Figure 24a. Flowfield Analysis: Symmetry Plane, AFWL Gas

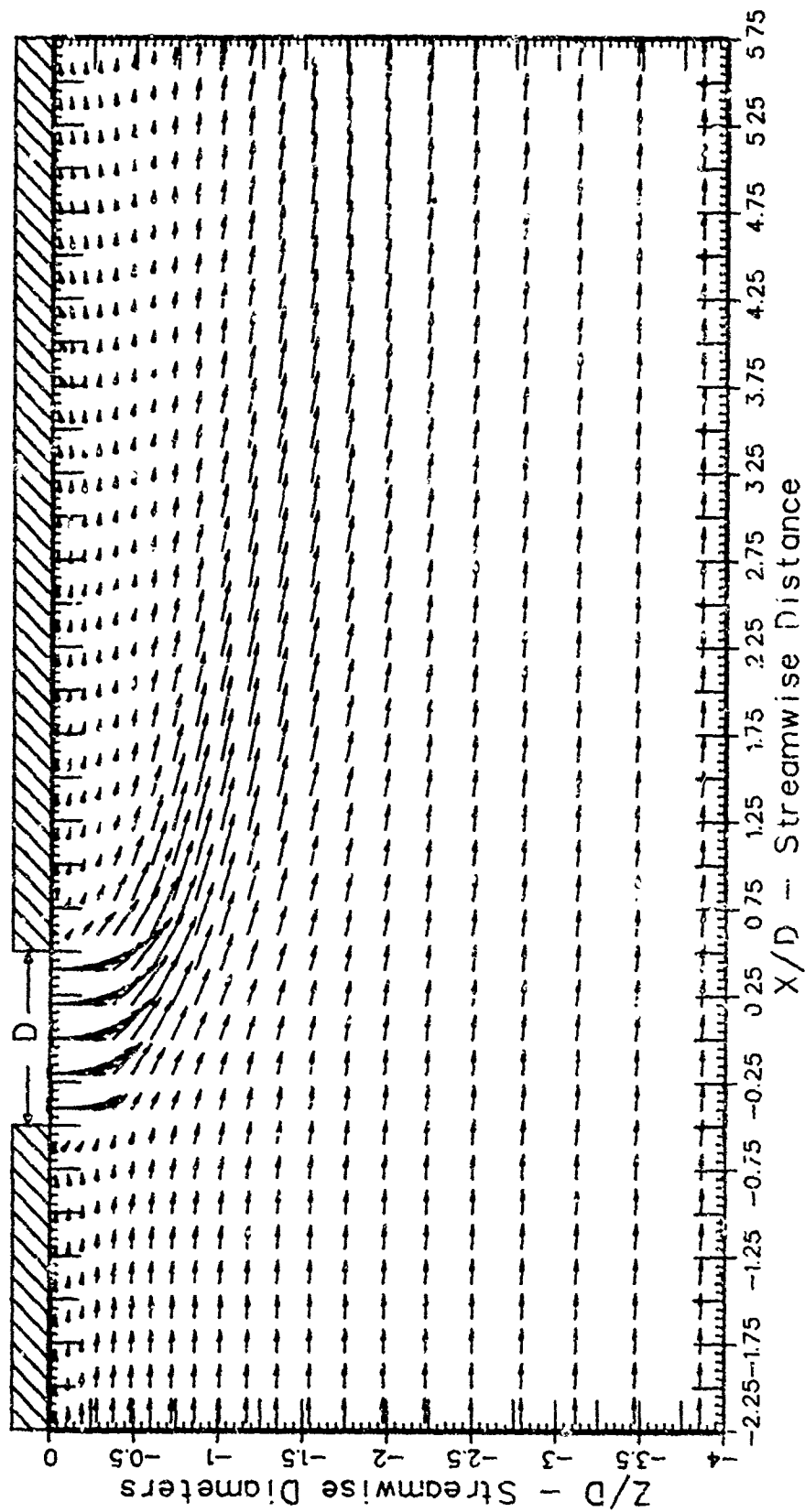


Figure 24b. Flowfield Analysis: Symmetry Plane -1, AFWL Gas

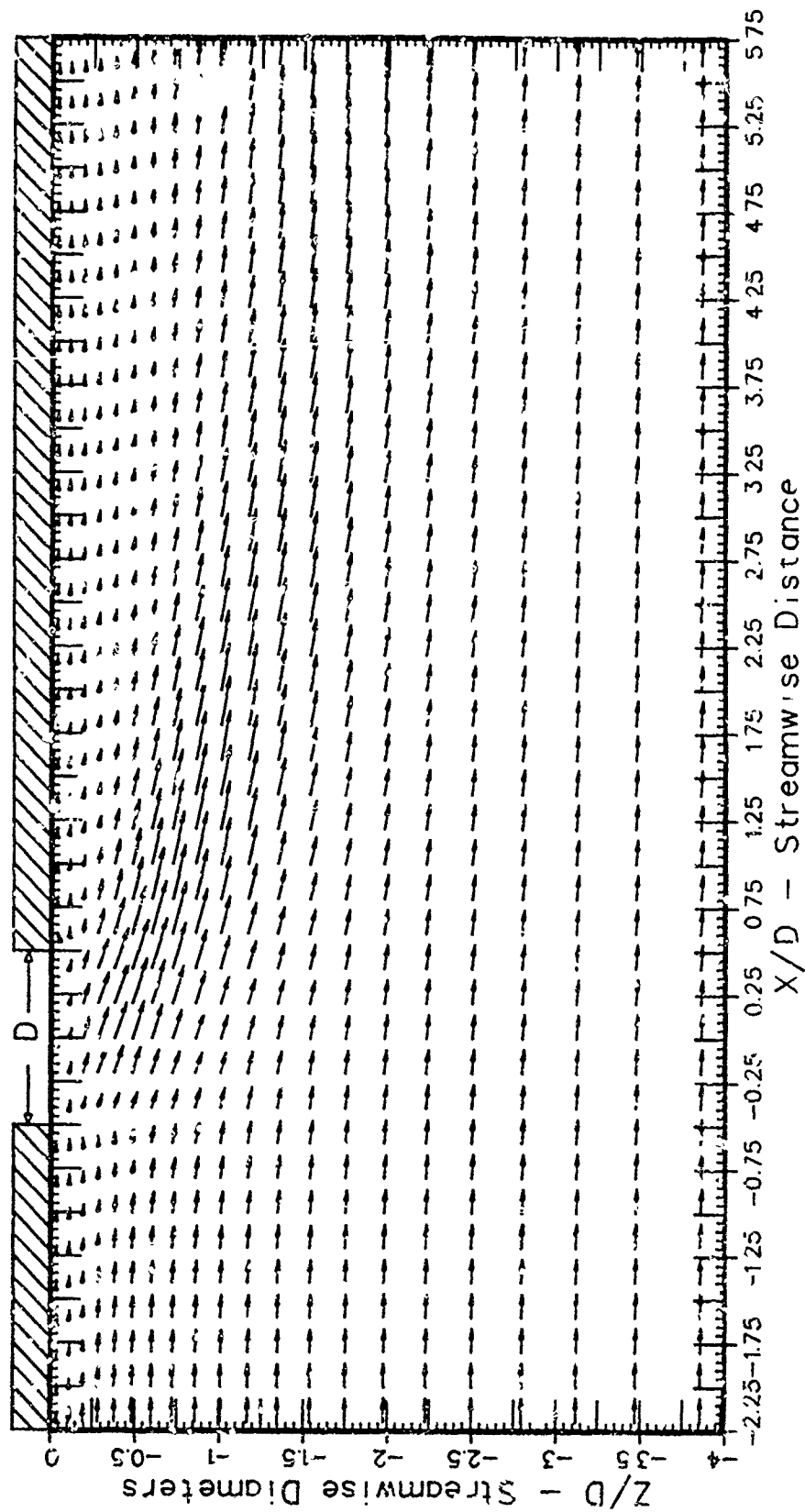


Figure 24c. Flowfield Analysis: Symmetry Plane -2, AFWL Gas

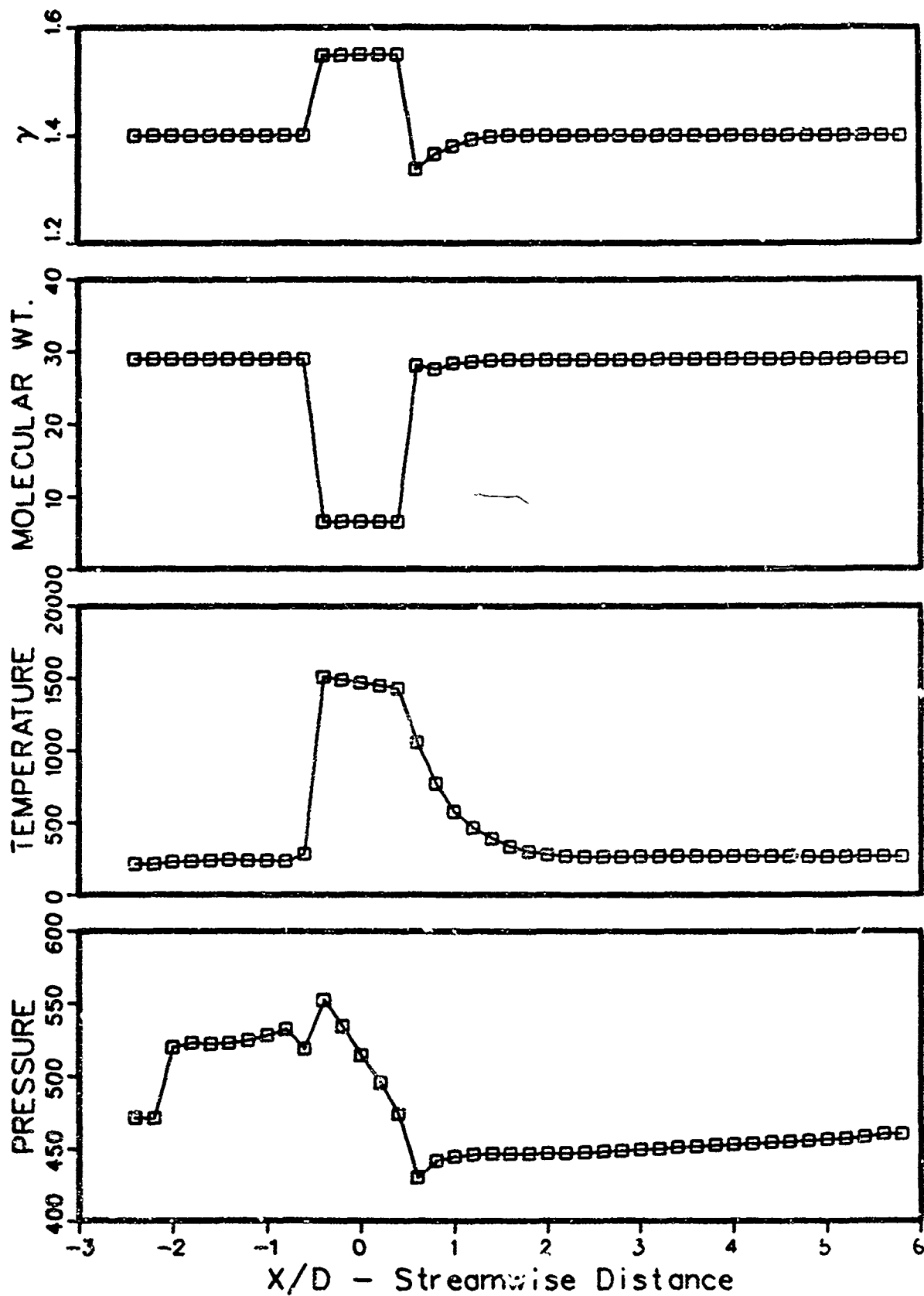


Figure 25. Symmetry Plane Surface Properties

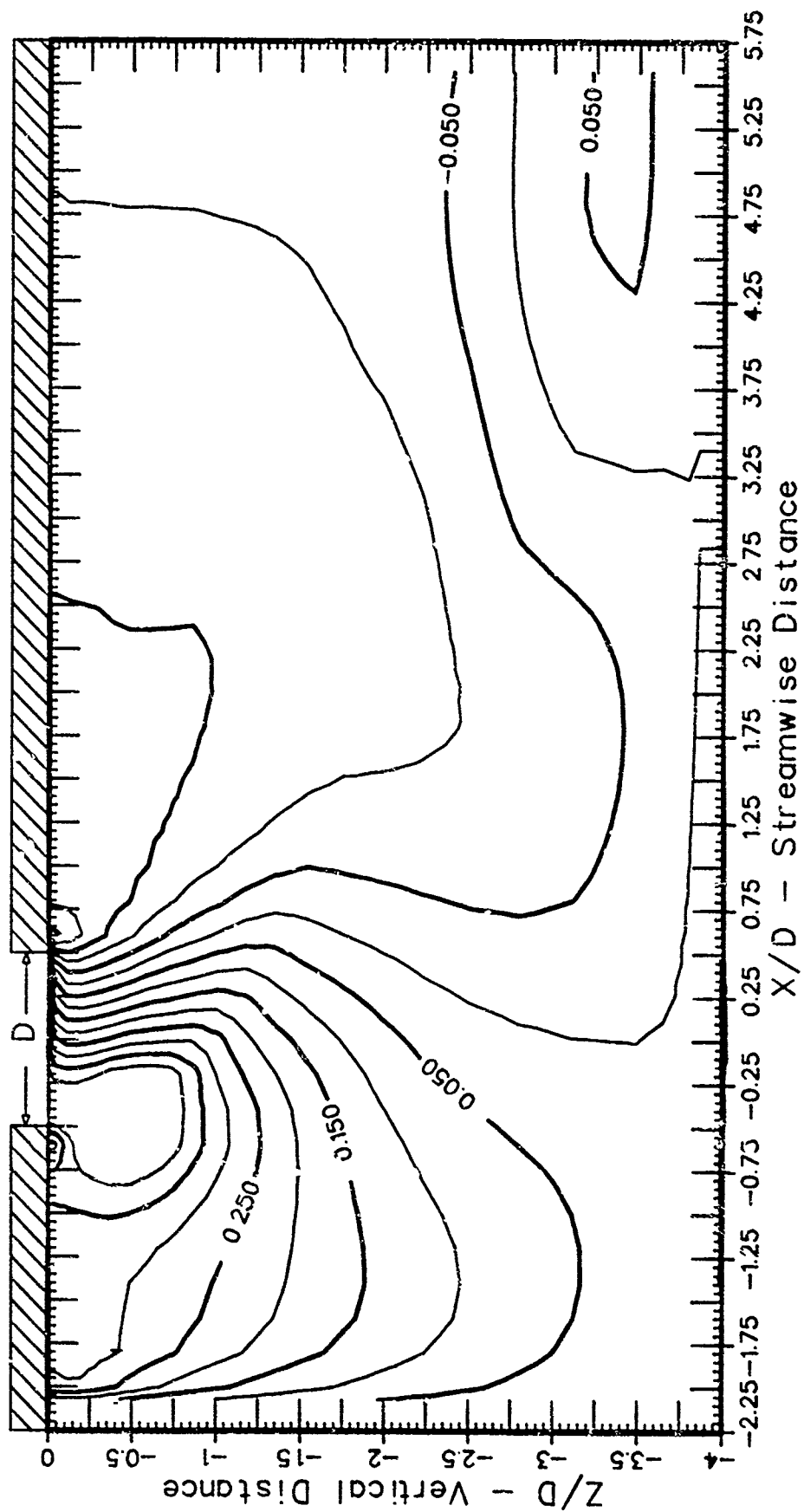


Figure 26. Flowfield Analysis: Symmetry Plane Pressure Coefficient Map

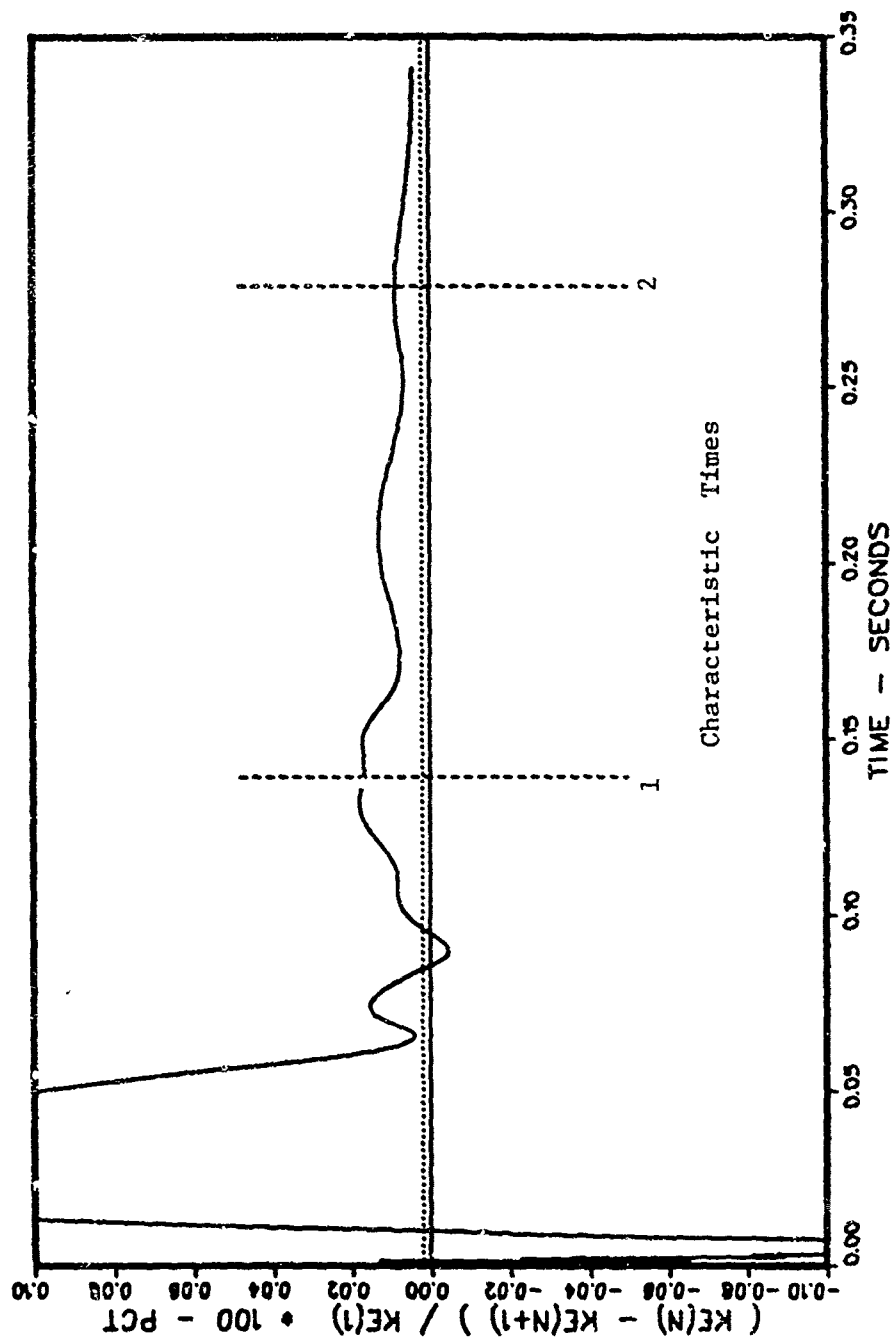


Figure 27. Convergence Criterion: Helium, $K=1.20$, Coarse Mesh

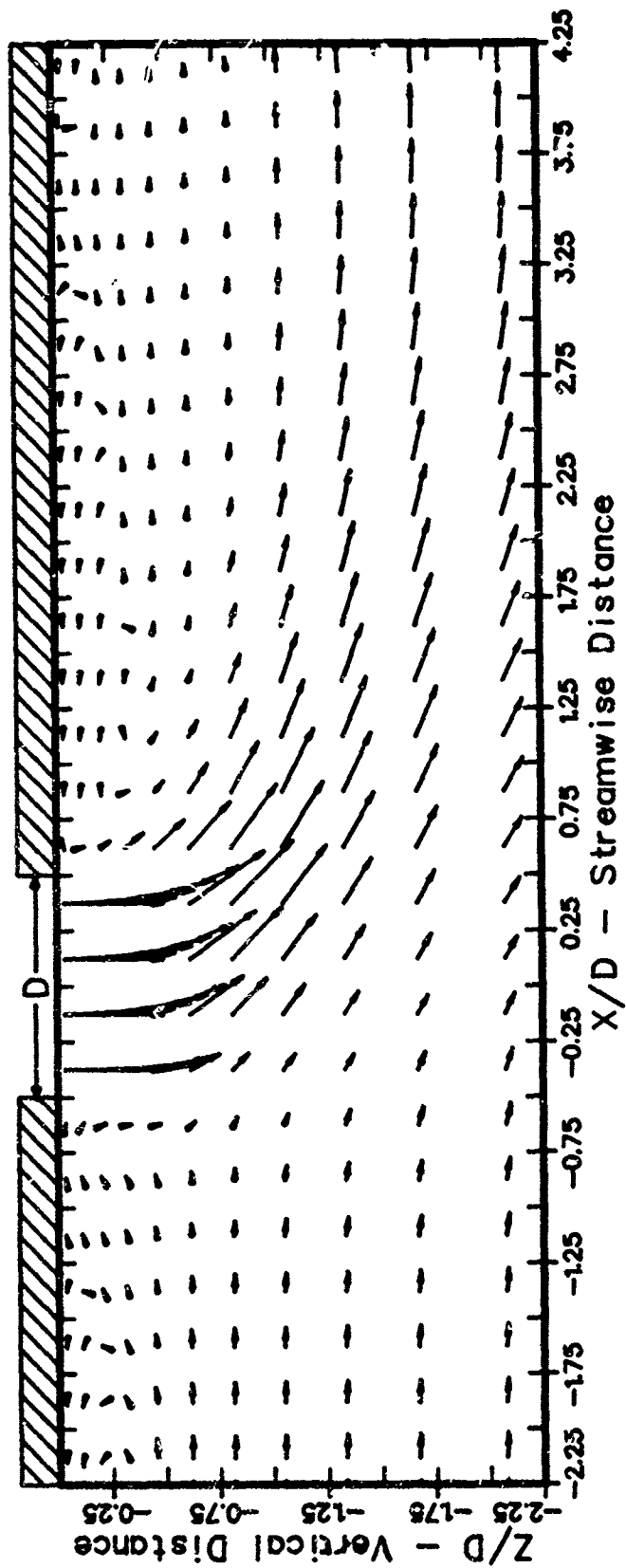


Figure 28. Flowfield Analysis: Helium, $K=1.20$, Coarse Mesh

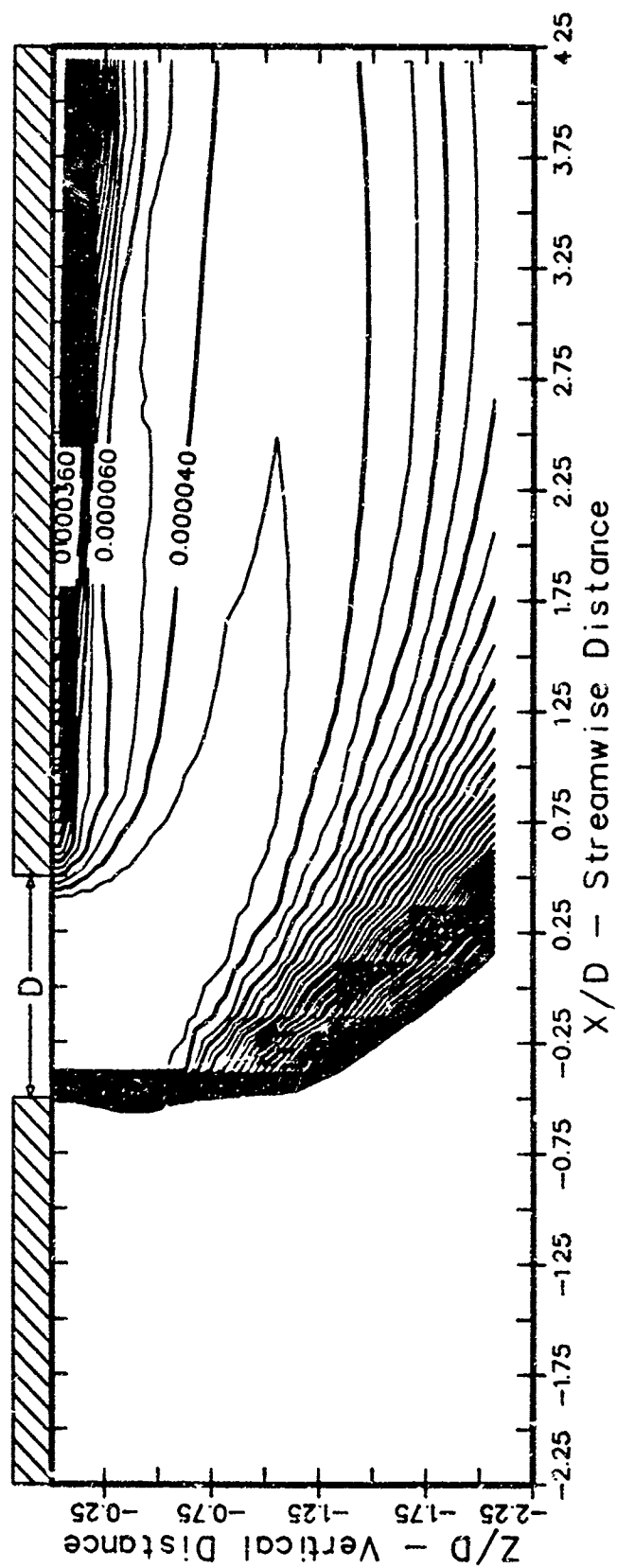


Figure 29. Trajectory Analysis: Helium, $K=1.27$, Coarse Mesh

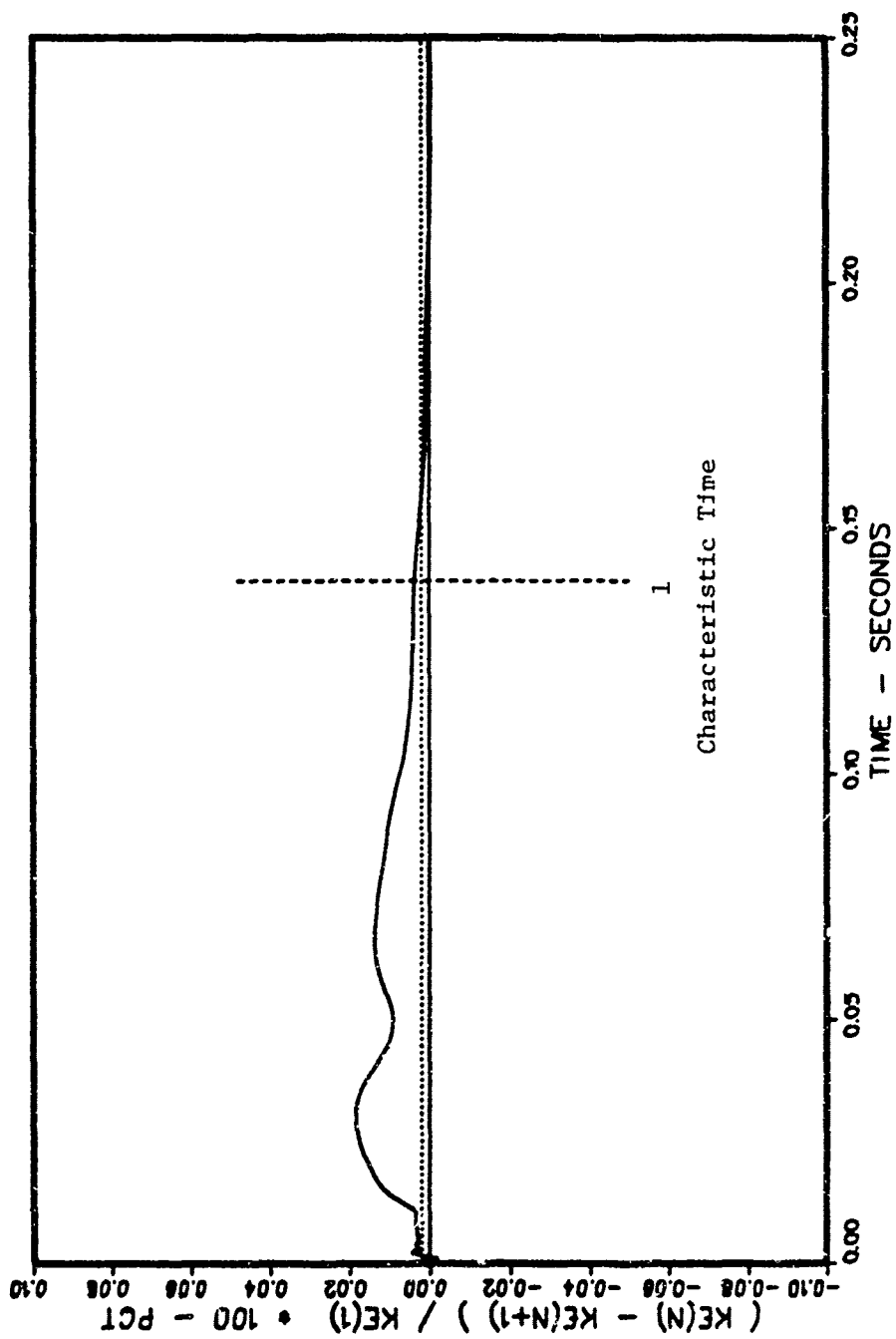


Figure 30. Convergence Criterion: Hot Air, $K=1.20$, Coarse Mesh

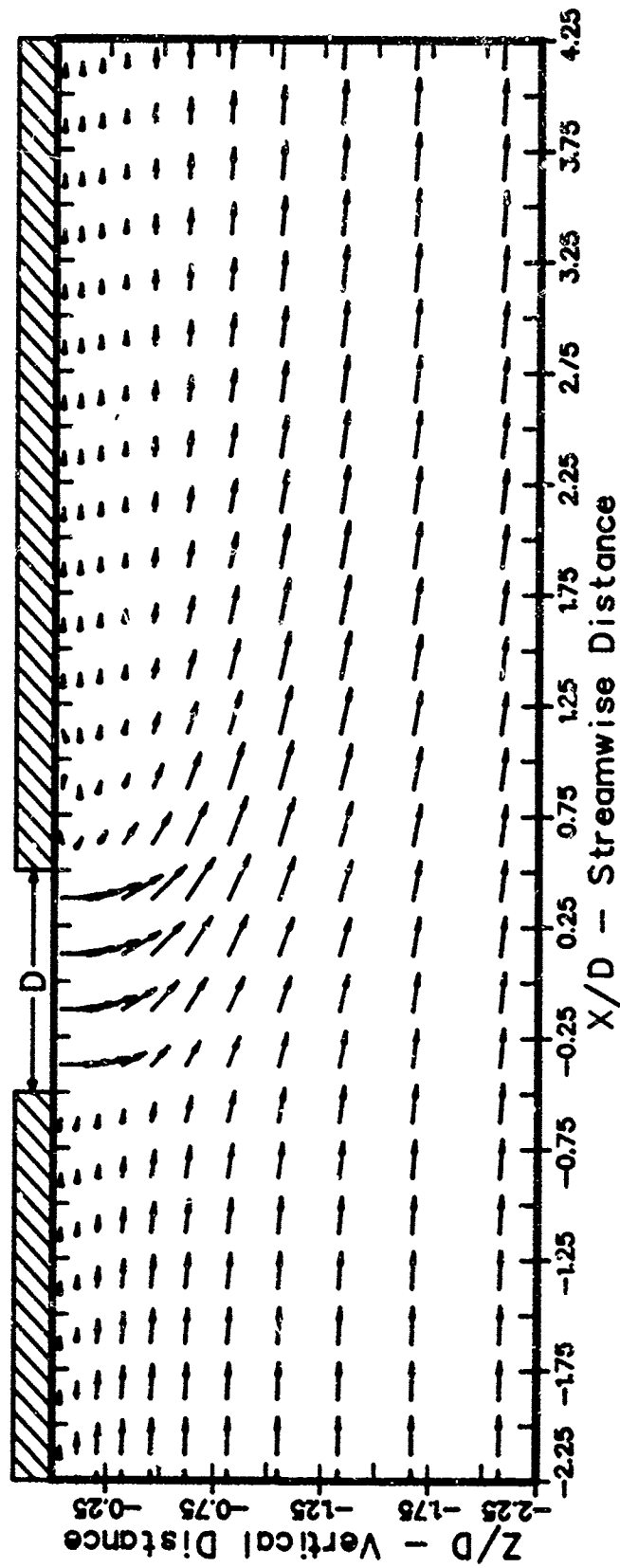


Figure 31. Flowfield Analysis: Hot Air, $K=1.20$, Coarse Mesh

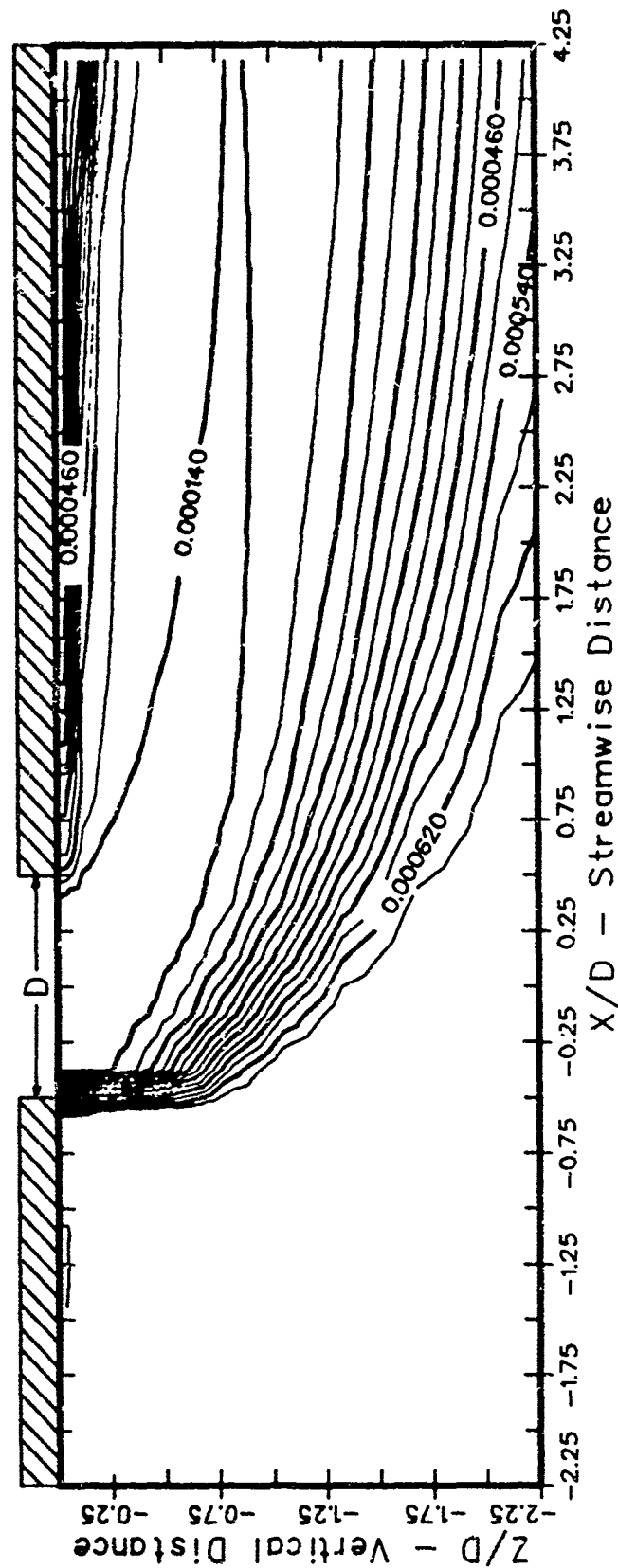


Figure 32. Trajectory Analysis: Hot Air, $K=1.20$, Coarse Mesh

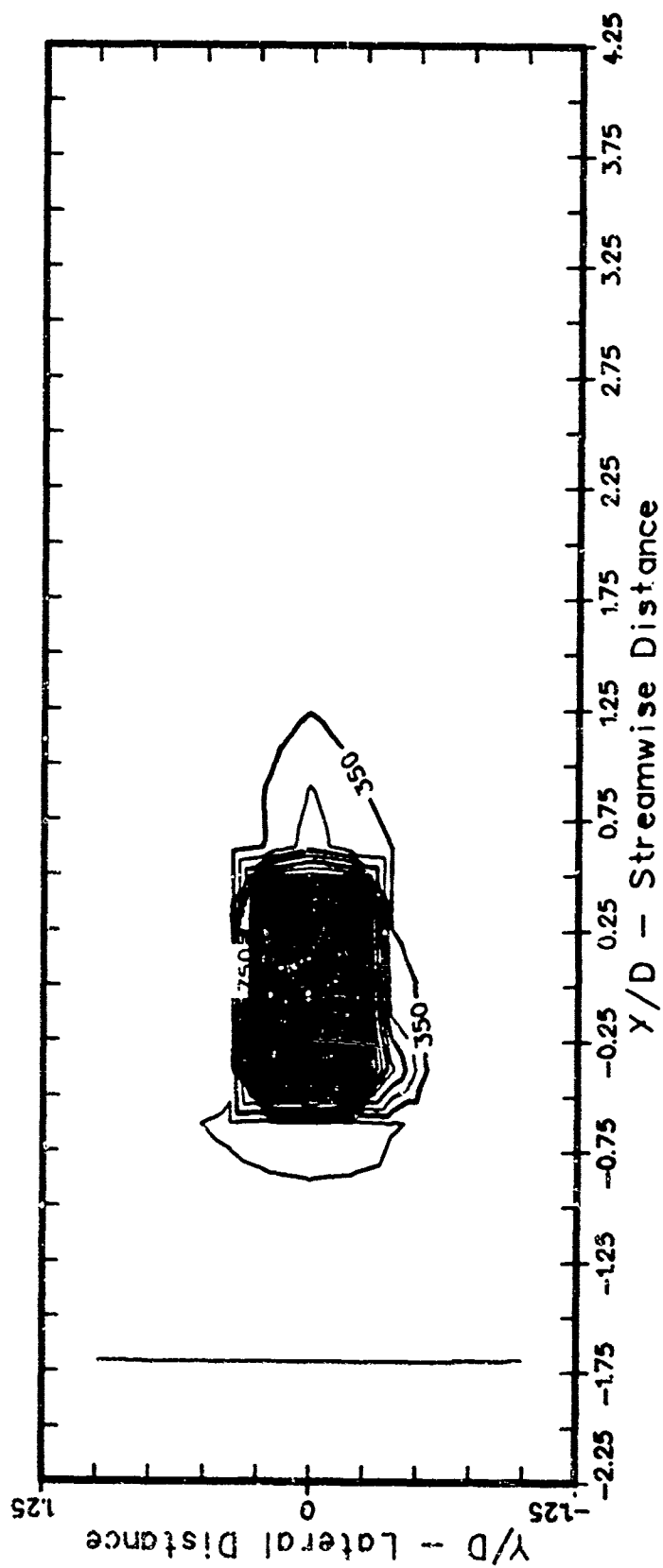


Figure 33. Adiabatic Wall Temperature: Hot Air, $K=1.20$, Coarse Mesh, Molecular

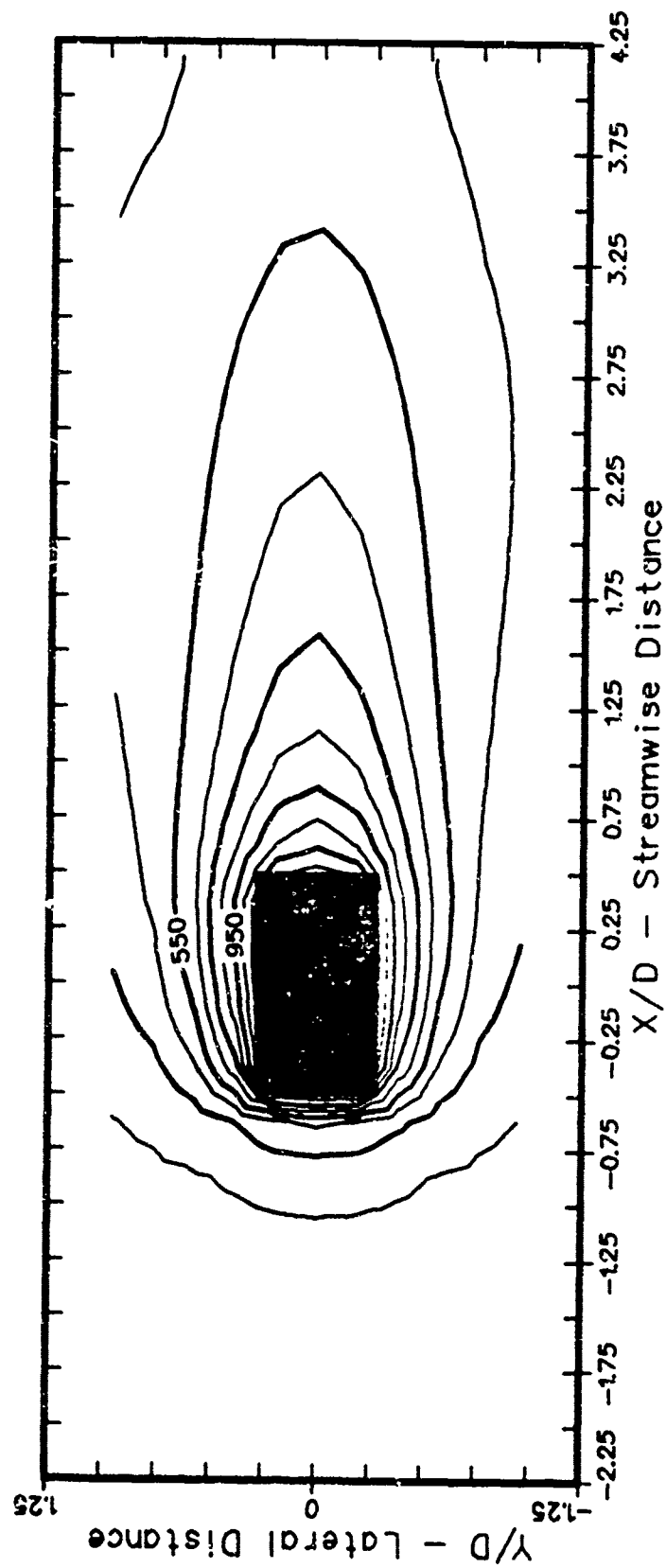


Figure 34. Adiabatic Wall Temperature: Hot Air, $K=1.20$, Coarse Mesh, Turbulent

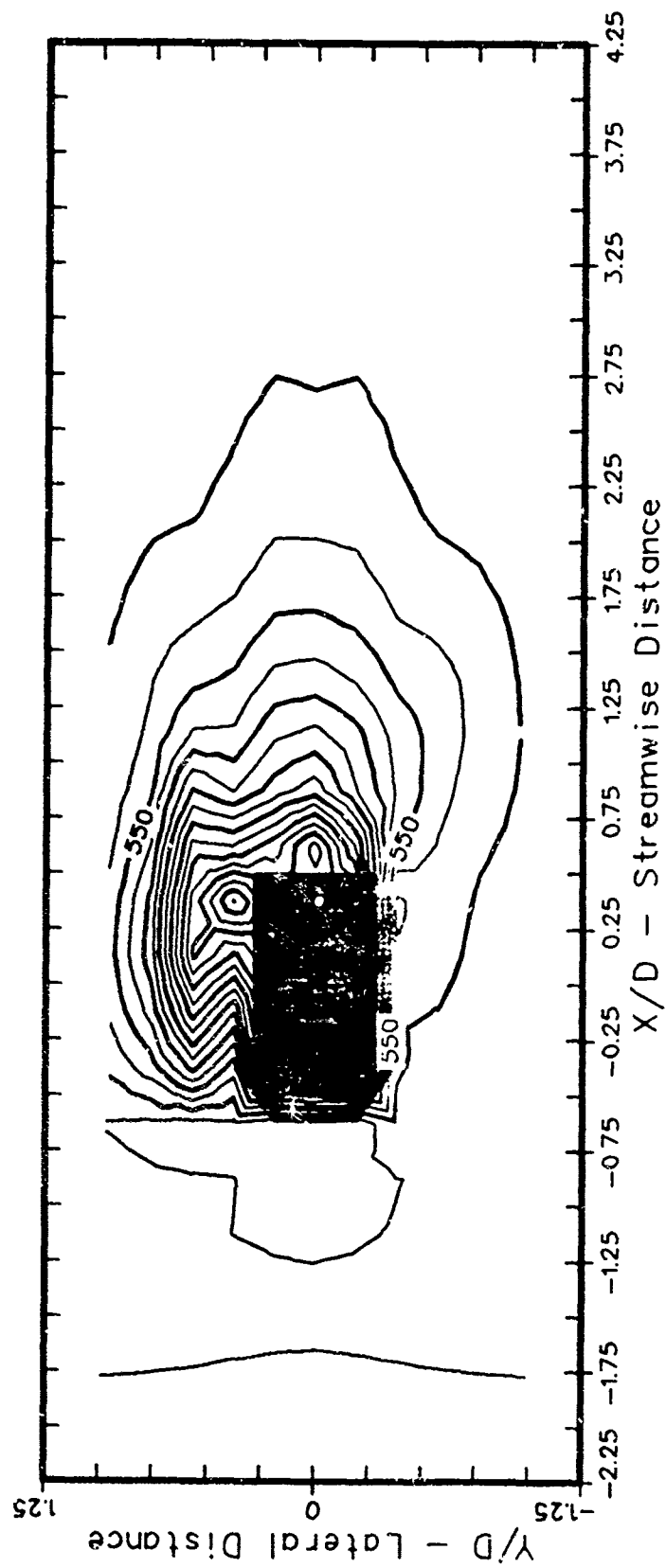


Figure 35. Adiabatic Wall Temperature: Helium, $K=1.20$, Coarse Mesh, Molecular

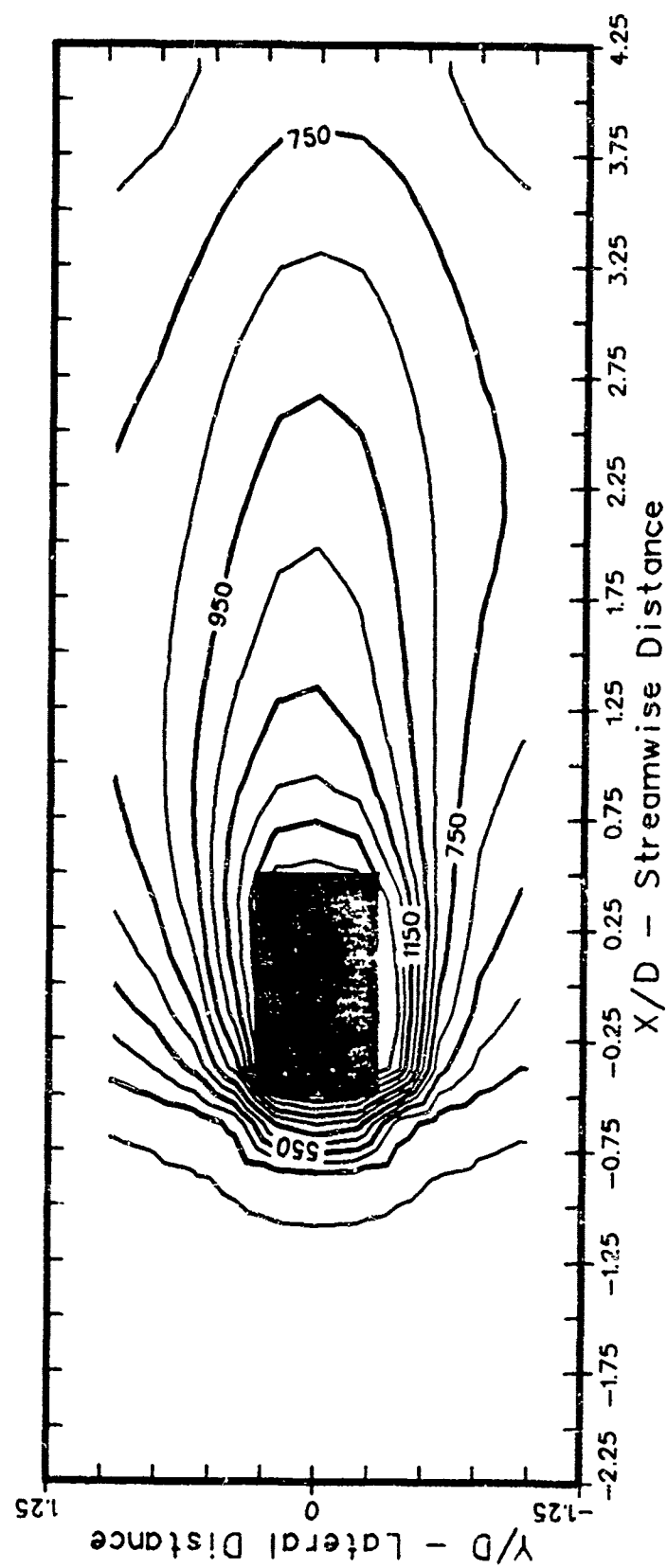


Figure 36. Adiabatic Wall Temperature: Helium, $K=1.20$, Coarse Mesh, Turbulent

Table I

AFWL Gas Mixture (CASE 2C)

Species _j	Mole Fraction [X _j]	Molecular Weight (M _j)
CF ₄	0.01281	160.39
He	0.86242	4.0026
D ₂	0.04140	4.028204
DF	0.03852	21.0125
HF	0.02562	20.006303
N ₂	0.01923	28.016

Average Gas Temperature: 1500 °K

Average Gas Molecular Weight: 6.60674

Specific Heat Ratio: 1.5484

Appendix A

1962 United States Standard Atmosphere

The computer simulation utilized a numerical description of the first two layers of the 1962 standard atmosphere. Figure A1 depicts the temperature variation with altitude as adopted by the 1962 standard atmosphere (Ref A.1).

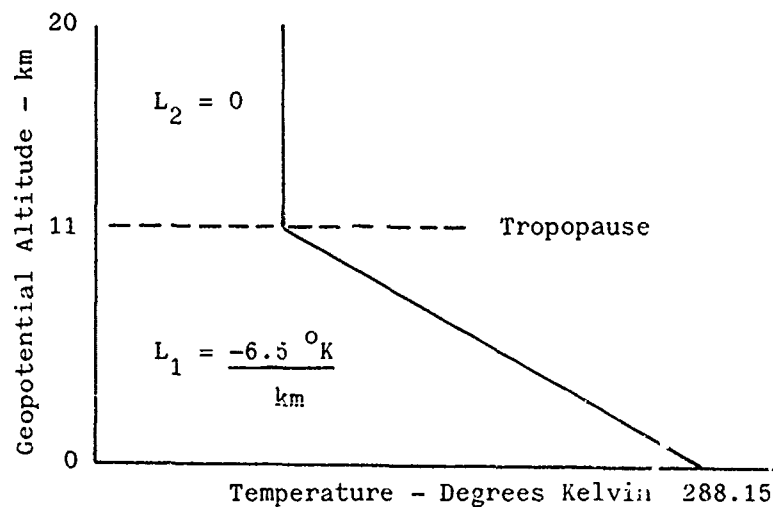


Figure A1. 1962 Standard Atmosphere

Associated with the temperature variation prescribed by Figure A1, there were values of basic constants utilized by mathematical model of the atmosphere which were also prescribed by the committee which derived the standard atmosphere. The following list of constants required by the atmospheric model are as follows:

Universal Gas Constant, R_{gas}	1545.31 ft-lb _f /(lb _m -mole-°R)
Sea Level Pressure, P_{SL}	2116.22 lb _f /ft ²
Sea Level Temperature, T_{SL}	288.15 °K

Acceleration of Gravity, g 32.174049 ft/sec²

Molecular Weight of Air, M 28.9644

To further reduce the complexity of the mathematical description of the atmosphere, non-dimensional quantities were defined to make the numerical model less dependent upon the myriad of units which could possibly be used to parameterize the atmosphere. These non-dimensional quantities are given by the following:

$$(1) \Theta = T_{\text{ambient}}/T_{\text{SL}} = T_{\text{ambient}}/288.15$$

$$(2) \delta = P_{\text{ambient}}/P_{\text{SL}} = P_{\text{ambient}}/2116.22$$

$$(3) \sigma = \rho_{\text{ambient}}/\rho_{\text{SL}} = \rho_{\text{ambient}}/0.00237691$$

A.1 Temperature Ratio

The first layer of the atmosphere is defined to exist between geopotential altitudes of 0 through 11 kilometers such that a uniform lapse rate, L_1 , of -6.5 °K/km is maintained. The temperature at any geopotential altitude between the endpoints of this layer is simply expressed by the following equation,

$$T_{\text{ambient}} = T_{\text{SL}} - L_1 \cdot h_p \quad (\text{A-1})$$

where h_p is any arbitrary layer-1 altitude.

Non-dimensionalization of the above expression is accomplished by dividing by the base temperature, T_{SL} , that is,

$$\Theta_1 = \frac{T_{\text{ambient}}}{T_{\text{SL}}} = 1 - \frac{L_1}{T_{\text{SL}}} h_p$$

$$= 1 - K_1 h_p \quad (\text{A-2})$$

where $K_1 = 6.8755856(10)^{-6}$ for h_p given in feet.

Noting that the second layer is isothermal, that is, the lapse rate L_2 is identically zero, the non-dimensional temperature ratio between geopotential altitudes of 11 and 20 kilometers is a constant given by,

$$\Theta_2 = 216.65/288.15 = 0.75186535 \quad (\text{A-3})$$

The temperature ratio specified by Eqs (A-2) and (A-3) completely define the temperature variation within the first two layers of the standard atmosphere.

A.2 Pressure and Density Ratios

The temperature variation for Layer-1 is prescribed precisely by Eq (A-1). However, the remaining state variables required to describe the atmosphere still must be determined. Assuming that the atmosphere remains in hydrostatic equilibrium, the associated equation which relates pressure changes to corresponding changes in altitude is given by,

$$dp = -\rho g dh_p \quad (\text{A-4})$$

Substituting Eqs (A-1), (A-2), and (A-4) into the equation of state results in the following ordinary first order differential equation

$$\frac{dp}{p} = - \frac{g}{1.8 R T_{SL}} \frac{dh_p}{1 - K_1 h_p} \quad (A-5)$$

$$\text{where } R = R_{\text{gas}}/M,$$

which is easily integrated between sea level and the tropopause (11 km) to yield the following non-dimensional expression for the pressure variation within the first atmospheric layer in terms of the non-dimensional temperature ratio,

$$\theta_1 = \theta_1^{5.2559121} \quad (A-6)$$

The non-dimensional pressure variation within the second layer of the standard atmosphere is obtained circuitously by substituting the value of the temperature of this isothermal layer into the equation of state, writing the resultant expression in differential form, and then finally equating that expression to the hydrostatic balance equation, Eq (A-4), to obtain the following ordinary differential equation for the density,

$$\frac{d\rho}{\rho} = \frac{-g dh_p}{C} \quad \text{where } C = R \theta_2 T_{SL} \quad (A-7)$$

This equation was integrated between $h_p = 11$ km and 20 km to determine the variation of Layer-2 density as a function of geopotential altitude which is given as follows in terms of the difference in altitude above the tropopause, $(h_p - h^*)$,

$$\rho = \rho^* \exp [-(g/C) (h_p - h^*)] \quad (A-8)$$

Non-dimensionalization of the above expression is accomplished by dividing through by the sea level density (ρ_{SL}),

$$\sigma_2 = \frac{\rho}{\rho_{SL}} = \frac{\rho^*}{\rho_{SL}} \exp [-(g/C) (h_p - h^*)] \quad (A-9)$$

However, a numerical value of ρ^* must still be obtained to define the density variation with geopotential altitude. Fortunately, at this point both the non-dimensional pressure and temperature variation with geopotential altitude are known in terms of basic parameters. Additionally, since the equation of state is expressible in terms of the non-dimensional quantities,

$$\delta = \sigma \cdot \Theta \quad (A-10)$$

the value of ρ^* can be explicitly obtained in the following manner:

$$\begin{aligned} \rho^* &= \rho_{SL} \cdot \sigma \Big|_{h_p = h^*} \\ &= \rho_{SL} \cdot \frac{\delta}{\Theta} \Big|_{h_p = h^*} \\ &= \rho_{SL} \cdot \Theta^{4.2559121} \end{aligned} \quad (A-11)$$

Consequently, Eq (A-9) now can be expressed in its final form as follows:

$$\sigma_2 = 0.29707289 \exp [-4.8063758(10)^{-5} (h_p - h^*)] \quad (A-12)$$

Since the non-dimensional temperature and density variation with geopotential altitude for the second layer are now known, the corresponding expression for the non-dimensional pressure variation with altitude can be determined from the non-dimensional equation of state, Eq (A-10), as indicated by,

$$\begin{aligned}\delta_2 &= \sigma_2 \Theta_2 \\ &= 0.22335881 \exp [-4.8063758(10)^{-5} (h_p - h^*)] \quad (A-13)\end{aligned}$$

Similarly, the non-dimensional density variation of the first layer is obtainable from the non-dimensional equation of state as follows:

$$\sigma_1 = \frac{\delta_1}{\Theta_1} = \Theta_1^{4.2559121} \quad (A-14)$$

A.3 Summary

The following expressions summarize the non-dimensional variation of temperature, pressure, and density within the first two layers of the 1962 United States standard atmosphere.

Layer-1 :

$$\Theta = 1 - 6.8755856(10)^{-6} h_p$$

$$\delta = 5.2559121$$

$$\sigma = 4.2559121$$

Layer-2

$$O = 0.75186535$$

$$S = 0.22335881 \exp [-4.8063758(10)^{-5} (h_p - h^*)]$$

$$\sigma = 0.29707289 \exp [-4.8063758(10)^{-5} (h_p - h^*)]$$

Appendix B

Gaussian Jet Velocity Profile

In addition to the uniform ("top-hat") velocity profile accommodated within the computer simulation, a truncated bivariate normal distribution was also included for possible use to approximate the exhaust gas velocity field as it was forcibly being ejected through a rectangular diffuser exit port into a high subsonic crossflow. The truncated bivariate density function was expressed in the following form (Ref B.1):

$$f(x,y) = \begin{cases} \frac{K}{2\pi\sigma_x\sigma_y} \exp\left\{ -\frac{1}{2}\left[\left(\frac{x-x_\mu}{\sigma_x}\right)^2 + \left(\frac{y-y_\mu}{\sigma_y}\right)^2\right] \right\}, \\ \text{for } |x| \leq a, |y| \leq b; \\ \\ 0, \text{ for } |x| > a, |y| > b. \end{cases} \quad (B-1)$$

where : x_μ , y_μ are the mean values of x and y respectively,

σ_x , σ_y are the standard deviations of x and y respectively, and,

$2a$, $2b$ are the dimensions of the rectangular jet orifice, $2a$ being aligned with the freestream direction.

The parameter K in Eq (B-1) accounts for the fact that the orifice is of finite dimension and that the approximation of the jet injection velocity by a Gaussian distribution over this finite region requires a truncation factor to compensate for the neglected part of the continuous Gaussian density function. The value of K is calculated from the following constraint equation,

$$\int_{-a}^a \int_{-b}^b f(x,y) dx dy = 1 \quad (B-2)$$

When the expression of the density function, Eq (B-1), is substituted into the above constraint equation, and, the indicated integrations are carried out, the following equation results:

$$\begin{aligned} \int_{-a}^a \int_{-b}^b f(x,y) dx dy = & \left(K \operatorname{erf} \left[\frac{\sqrt{2} \mu_x + \sqrt{2} a}{2 \sigma_x} \right] - K \operatorname{erf} \left[\frac{\sqrt{2} \mu_x - \sqrt{2} a}{2 \sigma_x} \right] \right) \operatorname{erf} \left[\frac{\sqrt{2} \mu_y + \sqrt{2} b}{2 \sigma_y} \right] + \\ & \left(K \operatorname{erf} \left[\frac{\sqrt{2} \mu_x - \sqrt{2} a}{2 \sigma_x} \right] - K \operatorname{erf} \left[\frac{\sqrt{2} \mu_x + \sqrt{2} a}{2 \sigma_x} \right] \right) \operatorname{erf} \left[\frac{\sqrt{2} \mu_y - \sqrt{2} b}{2 \sigma_y} \right] \quad (B-3) \end{aligned}$$

Given a rectangular jet of dimension $(2a) \times (2b)$, if the mean values, x_μ and y_μ , are assumed to be identically zero, then the following expression results from which the required value of K can be obtained directly, namely,

$$K \operatorname{erf}\left\{\frac{a}{\sqrt{2}\sigma_x}\right\} \operatorname{erf}\left\{\frac{b}{\sqrt{2}\sigma_y}\right\} = 1 \quad (\text{B-4})$$

It is easily verified that if the limits in Eq (B-3) are allowed to approach those associated with the true bivariate Gaussian distribution, that is, if both a and b were allowed to become infinitely large in the limit, and, if both standard deviations were constrained to remain positive, then the integral simplifies as required to the following identity, that is,

$$K = 1 \quad (\text{B-5})$$

If each half dimension of the rectangular orifice is assumed to represent the standard deviation in the respective coordinate direction, that is, if

$$a = \sigma_x \quad \text{and} \quad b = \sigma_y \quad (\text{B-6})$$

and furthermore, if the mean values of x and y are coincident with the values associated with the geometric center of the orifice, then the truncation correction factor for the truncated bivariate density function is expressible as

$$K = \frac{1}{\operatorname{erf}(\bar{a}) \operatorname{erf}(\bar{b})} \quad (\text{B-7})$$

where $\bar{a} = \sqrt{2}/2 = \bar{b}$, from which the value of K for this special case is immediately determined,

$$K = 2.1456238$$

(B-8)

The truncated bivariate Gaussian velocity distribution associated with the assumptions expressed in Eq (B-6) possesses a relatively flat profile which is characteristic of fully developed turbulent jets. Consequently, Eq (B-1) with the value of K expressed in Eq (B-8) was utilized to define the "normal" form of the velocity profile of the jet within the computer simulation.

Appendix C

Gas Transport Properties

Modeling real gases at elevated temperatures requires the additional complexity incurred by determining the gas mixture transport properties of viscosity (μ), thermal conductivity (λ), and molecular diffusion coefficient (\mathcal{D}). The corresponding properties of the pure component gases were approximated by using the well established Lennard-Jones 12-6 intermolecular potential function (Ref C.1) which is given by

$$\phi(r) = 4\epsilon \left\{ \left[\frac{\sigma}{r} \right]^{12} - \left[\frac{\sigma}{r} \right]^6 \right\} \quad (C-1)$$

which is clearly a function of only two parameters for any given gas; ϵ , the maximum energy of attraction (well depth of the potential function) expressed in ergs, and σ , the zero energy collision diameter expressed in angstroms. Svehla (Ref C.2) documented these force constants (ϵ/k and σ where k is the Boltzmann constant) for a large number of gaseous species. Additional values can be obtained from the Hirschfelder, Curtiss and Bird text (Ref C.1) for the more ordinary gases and from the report by Liley (Ref C.3) for the more exotic species more directly associated with the exhausts of chemical lasers. The Lennard-Jones force constants utilized within the computer simulation are tabulated in Table C.1. Tables of the required collision integrals, $\Omega^{(1,1)*}$ and $\Omega^{(2,2)*}$, used in the requisite expressions for gas transport properties were obtained from Ref (C.1) despite some errors allegedly inherent in them as reported by Liley (Ref C.3). Empirical expressions for these

integrals which are well suited to numerical programming are presented in Refs C.4 and C.5; however, these expressions neither are as accurate as the tabular values nor are they applicable over the entire range of values encountered during the numerical simulation. Consequently, the tabular values of Hirschfelder, Curtiss and Bird were retained.

C.1 Mixture Viscosity

The first approximation of the molecular viscosity for a pure gas may be written (Ref C.1, Eq 8.2-18) as,

$$\mu = 266.93 (10)^{-7} \frac{\sqrt{M T}}{\sigma^2 \Omega^{(2,2)*}}, \text{ poises} \quad (\text{C-2})$$

where M is the molecular weight of the gas species, and $\Omega^{(2,2)*}$ is a tabulated function of the reduced temperature, $T^* = T/(\epsilon/k)$, where T is absolute temperature expressed in degrees Kelvin.

Following the procedure outlined in Ref C.1, the updated value of the pure gas component viscosity was obtained by using Eq 8.2-19 of that reference which is given by,

$$[\mu]_k = \mu \cdot f_{\mu}^{(k)} \quad (\text{C-3})$$

where the function $f_{\mu}^{(k)}$ is the k^{th} -order correction factor whose value is approximately equal to one (1.). Values of this correction are tabulated (Table I-P) as functions of T^* in the text of Hirschfelder, Curtiss and Bird.

The rigorously derived expressions according to the Chapman-Enskog

theory for the viscosity of a multi-component gas mixture are presented in Ref C.1, Eqs 8.2-25 - 28; however, they involve the ratios of determinants whose elements are neither easily nor efficiently programmable for gas mixtures comprised of more than two distinct species. The rigorous expansion can be closely approximated for non-polar gases at low pressures by the following series (Ref C.5, Eq 9-5.1),

$$\mu_{\text{mix}} = \frac{\sum_{i=1}^N x_i \mu_i}{\sum_{j=1}^N x_j \phi_{ij}} \quad (\text{C-4})$$

where μ_i are the component pure gas viscosities, and, x_i are the mole fractions of each species.

Furthermore, utilization of Wilke's approximation for the parameter ϕ_{ij} (Ref C.5, Eq 9-35) as given by,

$$\phi_{ij} = \frac{\left[1 + \left\{ \frac{\mu_i}{\mu_j} \right\}^{0.5} \left\{ \frac{M_j}{M_i} \right\}^{0.25} \right]^2}{\left[8 \left(1 + \frac{M_i}{M_j} \right) \right]^{0.5}} \quad (\text{C-5})$$

where M_k are the component molecular weights, results in an easily programmable expression for the viscosity of the gaseous mixture. Brokaw (Ref C.6) developed alignment charts for both the component viscosities and the expression given by Eq (C-5). A method for calculating the viscosity of a gas mixture, some components of which are polar, was detailed by Brokaw in Ref C.7.

C.2 Mixture Thermal Conductivity

The first approximation for the thermal conductivity of a pure monatomic gas may be written in the following form (Ref C.1, Eq 8.2-31):

$$\lambda = 1989.1 (10)^{-7} \frac{\sqrt{M T}}{\sigma^2 \Omega^{(2,2)*}}, \text{ cal/(cm-sec-}^\circ\text{K)} \quad (\text{C-6})$$

again where M is the pure gas species molecular weight, $\Omega^{(2,2)*}$ is the collision integral tabulated as a function of the reduced temperature, T^* , and T is expressed in degrees Kelvin. Updating this first approximation to the pure gas thermal conductivity, the methodology of Hirschfelder, Curtiss, and Bird was utilized (Ref C.1, Eq 8.2-32) to obtain the k^{th} order approximation given by,

$$[\lambda]_k = \lambda \cdot f_{\lambda}^{(k)} \quad (\text{C-7})$$

where $f_{\lambda}^{(k)}$ is the k^{th} order correction factor tabulated in Ref C.1, Table I-P, as a function of T^* and it too is approximately equal to unity.

Analogously to the mixture viscosity calculations, the rigorous application of Chapman-Enskog theory for non-polar gases results in the mixture thermal conductivity being expressed again as a ratio of determinants (Ref C.1, Eq 8.2-43) whose elements are equally unwieldy for computational purposes. Instead, the Cheung, Bromley, and Wilke method (Ref C.5, Eq 10-6.1) utilizing the familiar Wassiljewa form of the approximation was employed to obtain the thermal conductivity for the gas mixture composed of non-polar gases, that is,

$$\lambda_{\text{mix}} = \frac{\sum_{i=1}^N x_i \lambda_i}{\sum_{j=1}^N x_j A_{ij}} \quad (\text{C-8})$$

where λ_i is the thermal conductivity of the i^{th} species given by Eq (C-6) , x_i and x_j are the mole fractions of species "i" and "j" respectively, and A_{ij} is a parameter which is temporarily unspecified.

The method proceeded by splitting the thermal conductivity of each species into two distinct parts,

$$\lambda_i = \lambda_i^* + \lambda_i^{**} \quad (\text{C-9})$$

where the first part, λ_i^* , accounts for the contribution of the monatomic, or translational, thermal conductivity of the species, and the second part, λ_i^{**} , accounts for the contribution of the polyatomic thermal conductivity by internal energy diffusional transport, or internal degrees of freedom (Ref C.2, Appendix B). After applying the Eucken corrections to λ_i^* to account for the presence of polyatomic gases, the following expressions for this quantity resulted (Ref C.4, Eq 10-40):

$$\lambda_i^* = \begin{cases} \lambda_i & , \text{ monatomic} \\ \lambda_i \left[1 / \left[1 + 0.35 \left(c_{p1} / R - 2 \right) \right] \right] & , \text{ linear} \\ \lambda_i \left[1 / \left[1 + 0.25 \left(c_{p1} / R - 2 \right) \right] \right] & , \text{ non-linear} \end{cases} \quad (\text{C-10})$$

After λ_i^{**} was obtained from Eq (C-9) and the unspecified parameter A_{ij}

was assumed to be well represented by ϕ_{ij} , Eq (C-5), the mixture thermal conductivity was expanded in the following manner:

$$\lambda_{\text{mix}} = \frac{\sum_{i=1}^N \lambda_i^* x_i}{\sum_{j=1}^N (M_{ij}/M_i)^{0.125} \phi_{ij} x_j} + \frac{\sum_{i=1}^N \lambda_i^{**} x_i}{\sum_{j=1}^N \phi_{ij} x_j} \quad (\text{C-11})$$

where

$$M_{ij} = (M_i + M_j) / 2 \quad (\text{C-12})$$

C.3 Mixture Molecular Diffusion Coefficient

The first approximation of the coefficient of diffusion for a binary gas mixture comprised of species "i" and "j" is given by the following expression (Ref C.1, Eq 8.2-44),

$$D_{ij} = 0.0026280 \frac{\sqrt{T^3 (M_i + M_j) / (2M_i M_j)}}{P \sigma_{ij} \Omega_{ij}^{(1,1)*}} \text{ , (cm}^2\text{/sec)} \quad (\text{C-13})$$

where P is the pressure in atmospheres, T is the temperature in degrees Kelvin, $\Omega_{ij}^{(1,1)*}$ is the collision integral evaluated at the temperature T_{ij}^* ,

$$T_{ij}^* = T / \sqrt{\left(\frac{\epsilon}{k}\right)_i \cdot \left(\frac{\epsilon}{k}\right)_j} \quad (\text{C-14})$$

where σ_{ij} is the pair molecular potential energy parameter given by,

$$\sigma_{ij} = (\sigma_i + \sigma_j) / 2, \text{ (angstroms)} \quad (C-15)$$

This approximation of D_{ij} was similarly updated by multiplication with the k^{th} order correction factor, $f_D^{(k)}$, given by (Ref C.1, Eq 8.2-45)

$$[D_{ij}]_k = D_{ij} \cdot f_D^{(k)} \quad (C-16)$$

where $f_D^{(k)}$ is also tabulated in Table I-P of Ref C.1 as a function of the reduced temperature, T^* . This correction factor also is approximatedly equal to unity.

Calculation of the diffusion coefficient for a mixture of gases is extremely difficult if not nearly impossible for gaseous mixtures representative of exhausts from chemical laser systems. However, if one starts with the Stefan-Maxwell equations given by (Ref C.8, Eq 18.4-19),

$$\nabla x_i = \sum_{j=1}^N \frac{x_i x_j}{D_{ij}} (v_j - v_i) \quad (C-17)$$

where x_i is the mole fraction of species "i", D_{ij} is the binary mixture diffusion coefficient for the i-j species gaseous pair, and v_j and v_i are the velocities of species "j" and "i" respectively, and if, it is further assumed that one homogeneous gas diffuses into another homogeneous gas (for example, air diffusing into the exhaust jet gases), then it becomes possible to derive the diffusion coefficient of the binary mixture comprised of both the homogeneous gases. The resulting expression of the molecular diffusion coefficient for this binary gaseous pair is then given by (Ref C.8, Eq 18.4-25),

$$D_{in} = \frac{1 - x_i}{\sum_{\substack{j=1 \\ j \neq i}}^N \frac{x_j}{D_{ij}}}, \text{ (cm}^2\text{/sec)} \quad (C-18)$$

where x_i and x_j are the mole fractions of the diffusing gas and the exhaust gases respectively, and D_{ij} is the binary mixture diffusivity of the diffusing gas with each of the exhaust species gases comprising the laser exhaust which is given for each of these pairs by Eq (C-13).

C.4 Unit Conversion

The units utilized within the computer simulation were predominantly English engineering units. The units associated with the transport properties of the gases were initially computed in various forms of the Metric system thereby necessitating numerical conversion. The conversion factor compendium of Mechtley (Ref C.9) was used to facilitate conversion of the derived properties to compatible English engineering units. The conversion tables in Ref C.9 are equally usable, however, the corresponding factors are not carried to the same precision as those provided by Mechtly.

Table C.1

Lennard Jones (12-6) Force Constants

Species	Molecular Weight	ϵ/k (°K)	σ (Å)
CF ₄	88.00475	134.0	4.662
He	4.00260	10.22	2.551
D ₂	4.0028204	35.20	2.952
HF	20.006303	330.0	3.418
DF	21.0125	199.1	2.826
N ₂	28.016	71.4	3.798
Air	28.9644	78.6	3.711

Appendix D

Thermodynamic Properties

Gas mixture thermodynamic properties were calculated from component species thermodynamic properties based upon the respective mass fractions of each species. Values of specific heat at constant pressure, c_p , and sensible enthalpy, $h-h_{298.15}$, were tabulated for each gas mixture component as functions of temperature from 200 - 2500°K. The values for the exhaust gas species were obtained from the JANAF Thermochemical Tables (Ref D.1). The corresponding values for air were obtained from two separate sources; sensible enthalpies were obtained from the tables of Keenan and Kaye (Ref D.2) while specific heats were obtained from the text by Eckert and Drake (Ref D.3, Table B-4). Tables D.1 and D.2 list the values of c_p and $h-h_{298.15}$ for every gas component required by the computer simulation. Required unit conversions were again accomplished using the compendium of conversion factors compiled by Mochly (Ref C.9).

Table D.1

Thermochemical Data - c_p - (Gibbs/mole)

Temperature (°K)	Gas Species						
	CF ₄	He	D ₂	HF	DF	N ₂	Air
200.	11.322	4.968	6.980	6.962	6.961	6.957	6.955
298.15	14.592	4.968	6.978	6.964	6.964	6.961	6.962
300.	14.648	4.968	6.978	6.964	6.964	6.961	6.962
400.	17.304	4.968	6.989	6.967	6.973	6.990	7.020
500.	19.290	4.968	7.019	6.972	7.002	7.069	7.127
600.	20.741	4.968	7.079	6.986	7.065	7.196	7.304
700.	21.799	4.968	7.172	7.015	7.161	7.350	7.443
800.	22.580	4.968	7.290	7.063	7.281	7.512	7.600
900.	23.166	4.968	7.423	7.129	7.413	7.670	7.762
1000.	23.613	4.968	7.561	7.211	7.549	7.815	7.904
1100.	23.960	4.968	7.698	7.303	7.681	7.945	8.030
1200.	24.234	4.968	7.830	7.402	7.806	8.061	8.162
1300.	24.453	4.968	7.954	7.504	7.923	8.162	8.286
1400.	24.631	4.968	8.070	7.606	8.029	8.252	8.404
1500.	24.777	4.968	8.177	7.705	8.126	8.330	8.515
1600.	24.899	4.968	8.275	7.800	8.215	8.398	8.639
1700.	25.001	4.968	8.366	7.891	8.295	8.458	8.771
1800.	25.087	4.968	8.450	7.977	8.367	8.512	8.909
1900.	25.161	4.968	8.527	8.058	8.433	8.559	9.062
2000.	25.224	4.968	8.598	8.133	8.493	8.601	9.263
2500.	25.439	4.968	8.891	8.442	8.724	8.756	11.685

Table D.2

Thermochemical Data - $h_{298.15} - (\text{kcal/mole})$

Temperature (°K)	Gas Species						
	CF ₄	He	D ₂	HF	DF	N ₂	Air
200.	-1.276	-0.488	-0.685	-0.683	-0.683	-0.683	-0.680
298.15	0.	0.	0.	0.	0.	0.	0.
300.	0.027	0.009	0.013	0.013	0.013	0.013	0.013
400.	1.631	0.506	0.711	0.709	0.710	0.710	0.711
500.	3.465	1.003	1.411	1.406	1.408	1.413	1.417
600.	5.471	1.500	2.116	2.104	2.111	2.125	2.136
700.	7.600	1.996	2.828	2.804	2.822	2.853	2.871
800.	9.821	2.493	3.551	3.508	3.544	3.596	3.623
900.	12.110	2.990	4.287	4.217	4.279	4.355	4.391
1000.	14.450	3.487	5.036	4.934	5.027	5.129	5.174
1100.	16.829	3.984	5.799	5.660	5.788	5.917	5.979
1200.	19.239	4.480	6.575	6.395	6.563	6.718	6.777
1300.	21.674	4.977	7.365	7.140	7.349	7.529	7.595
1400.	24.129	5.474	8.166	7.896	8.147	8.350	8.422
1500.	26.599	5.971	8.979	8.661	8.955	9.179	9.256
1600.	29.083	6.468	9.801	9.437	9.772	10.015	10.097
1700.	31.578	6.964	10.633	10.221	10.598	10.858	10.945
1800.	34.083	7.461	11.474	11.015	11.431	11.707	11.798
1900.	36.595	7.958	12.323	11.816	12.271	12.560	12.656
2000.	39.115	8.455	13.179	12.626	13.117	13.418	13.519
2500.	51.786	10.939	17.555	16.774	17.425	17.761	17.351
ΔH_f^0 298.15	-223.04	0.	0.	-65.14	-65.85	0.	0.

Vita

William Charles Golbitz was born 16 February 1943 in Williamsport, Pennsylvania, the son of Louis H. Golbitz and Sylvia Friedman Golbitz. He attended the Pennsylvania State University for one year after graduating from Williamsport Senior High School in 1961 prior to his accepting an appointment to the United States Air Force Academy. After graduation in June 1966 with a B. S. degree in Engineering Science and commissioning as a Second Lieutenant in the Regular Air Force, he entered active duty as a performance flight test engineer at the Air Force Flight Test Center, Edwards AFB, California. After this assignment, the requirements for a M. S. degree in Aerospace Engineering were completed in December 1970 at the University of Texas at Austin, Texas, from which he was assigned to the San Antonio Air Logistics Center, Kelly AFB, Texas, until May 1975 as Lead Aerodynamics Engineer for the C-5A aircraft. He was then reassigned to the Engineering Deputate of the Aeronautical Systems Division, Wright-Patterson AFB, Ohio, as an aeronautical engineer through June 1977 during which time he conducted analyses for V/STOL and reconnaissance air vehicles as well as for both jet and integral-rocket-ramjet powered missiles. From July to the present, he has been enrolled in the Doctoral Program in Aeronautical Engineering at the Air Force Institute of Technology, Wright-Patterson AFB, Ohio.

Forwarding Address: 145 Waltham Street, Apt 6,
Maynard, Massachusetts 01754

UNCLASSIFIED

SECURITY CLASSIFICATION OF THIS PAGE (When Data Entered)

REPORT DOCUMENTATION PAGE		READ INSTRUCTIONS BEFORE COMPLETING FORM
1. REPORT NUMBER AFIT/DS/AA/80-1	2. GOVT ACCESSION NO. AD-A0910 343	3. RECIPIENT'S CATALOG NUMBER
4. TITLE (and Subtitle) TIME DEPENDENT NAVIER-STOKES SOLUTION OF A TURBULENT GAS JET EJECTED FROM A RECTANGULAR ORIFICE INTO A HIGH-SUBSONIC FLOW		5. TYPE OF REPORT & PERIOD COVERED PhD Dissertation
7. AUTHOR(s) William C. Golbitz, Major USAF		6. PERFORMING ORG. REPORT NUMBER N/A
9. PERFORMING ORGANIZATION NAME AND ADDRESS Air Force Institute of Technology (AFIT-EN) Wright-Patterson AFB, Ohio 45433		8. CONTRACT OR GRANT NUMBER(s) N/A
11. CONTROLLING OFFICE NAME AND ADDRESS Air Force Flight Dynamics Laboratory Air Force Wright Aeronautical Laboratories Wright-Patterson AFB, Ohio 45433		10. PROGRAM ELEMENT, PROJECT, TASK AREA & WORK UNIT NUMBERS Project No. 317J Task No. 317J50 Work Unit No. 317J5007
14. MONITORING AGENCY NAME & ADDRESS (if different from Controlling Office) N/A		12. REPORT DATE June 1980
		13. NUMBER OF PAGES 186
		15. SECURITY CLASS (of this report) UNCLASSIFIED
		15a. DECLASSIFICATION/DOWNGRADING SCHEDULE
16. DISTRIBUTION STATEMENT (of this Report) Approved for public release; distribution unlimited.		
17. DISTRIBUTION STATEMENT (of the abstract entered in Block 20, if different from Report)		
18. SUPPLEMENTARY NOTES Approved for public release; IAW AFR 190-17. <i>Frederic C. Lynch</i> FREDERIC C. LYNCH, Major, USAF Director of Public Affairs		
19. KEY WORDS (Continue on reverse side if necessary and identify by block number) Numerical Methods; Navier-Stokes Solutions; Turbulent Mixing; Jet Mixing; Jet-Crossflow Interactions; Hot Gases; Jet Impingement; Jet Exhaust Flows; Compressible Flows		
20. ABSTRACT (Continue on reverse side if necessary and identify by block number) High temperature exhaust gases from an airborne chemical laser ejected at a jet to freestream dynamic pressure ratio (Q) of 0.15 from an aspect ratio 1.75 rec- tangular diffuser exit aligned parallel to the ambient crossflow was numerically simulated. The time dependent, three-dimensional Navier-Stokes equations and a species conservation equation were solved. Diffusive flux effects caused by concentration gradients as well as variable transport and thermodynamic proper- ties were incorporated into the numerical model. Turbulence closure was achieved by a locally varying velocity defect eddy viscosity model. Chemical		

DD FORM 1 JAN 73 1473

EDITION OF 1 NOV 63 IS OBSOLETE


UNCLASSIFIED

SECURITY CLASSIFICATION OF THIS PAGE (When Data Entered)

Unclassified

SECURITY CLASSIFICATION OF THIS PAGE(When Data Entered)

block 20 continued

reactions between the exhaust gases and the crossflow were proscribed. The trajectory of the jet plume, the extent of recirculation zones, and regions with high rates of heat transfer were defined. Simplified analyses demonstrated that essential flow phenomena were replicated. Convective processes dominated the low Q jet-crossflow interaction. Thermal diffusion had significantly greater effect than molecular diffusion for the jet-crossflow gases simulated. Jet penetration was dependent upon the molecular weight of the injectant for the constant Q constraint. A molecular weight correction factor was empirically used to synthesize the trajectory of one gas from that of another gas and to correct empirical trajectory formulae for molecular weight variances. Sensitivity analyses relating heat transfer to the injection surface from the jet plume with the magnitude of the turbulence diffusivities were conducted. 

UNCLASSIFIED

SECURITY CLASSIFICATION OF THIS PAGE(When Data Entered)